To the Graduate Council:

I am submitting herewith a thesis written by Chance Thomas Donahue entitled “Thermal, Magnetic, and Mechanical Stresses and Strains in Copper/Cyanate Ester Cylindrical Coils – Effects of Variations in Fiber Volume Fraction.” I have examined the final electronic copy of this thesis for form and content and recommend that it be accepted in partial fulfillment of the requirements for the degree of Master of Science, with a major in Mechanical Engineering.

Madhu S. Madhukar

Major Professor

We have read this thesis and

recommend its acceptance:

J.A.M. Boulet

John D. Landes

Accepted for the Council:

Carolyn R. Hodges

Vice Provost and Dean of the Graduate School

(Original signatures are on file with official student records.)

THERMAL, MAGNETIC, AND MECHANICAL STRESSES AND STRAINS IN COPPER/CYANATE ESTER CYLINDRICAL COILS – EFFECTS OF VARIATIONS IN FIBER VOLUME FRACTION

A Thesis

Presented for the

Master of Science Degree

The University of Tennessee, Knoxville

Chance Thomas Donahue

August 2010

Copyright © 2010 by Chance Thomas Donahue

All rights reserved.

ACKNOWLEDGEMENTS

I wish to thank all those who helped me complete my Master of Science Degree in Mechanical Engineering. I would like to thank Dr. Madhukar for his guidance and his effort to teach me about composite materials, continuum mechanics, mechanics of materials, and sustainable energy concepts. His many conversations with me have been very helpful to my continued learning. I appreciate his acceptance of me to the program and for his patient assistance through the whole process.

I also wish to thank Dr. Matthew Hooker of Composite Technologies Development, Inc. His ready assistance and guidance in the project and the useful data he sent me were invaluable to this research. The trips he made to the lab were much appreciated and all of his e-mail correspondences to any question I had were a great asset.

I would like to thank Kevin Freudenberg, Kirk Lowe, and Supratik Datta for their help on using the finite element analysis software COMSOL. They took time out of their busy schedules to guide me in the right direction and were patient with my numerous questions. Without them the FEA portion of the project would have been harder to complete.

The wonderful opportunity to work at the Magnet Development Laboratory was a great experience. All of the staff there were a huge asset and I learned so much just observing their work. The facilities at my disposal were phenomenal and the work ethic and eagerness to assist me were much appreciated. The opportunity to attend meetings and listen to all the knowledge passed on was truly an honor that I am very grateful for.

I would like to thank Dr. Landes for teaching me about solid mechanics and advanced mechanics of materials and for his guidance on classes. I would like to thank Dr. Boulet for his guidance on programs and coursework. I wish to thank all three professors for serving on my committee.

Lastly, I would like to thank my family and my friends, whose suggestions and encouragement made all of my hard work possible. It is impossible for me to quantify how much they have helped me in all of my accomplishments.

To every who has helped me along the way, thank you for your time and support.

ABSTRACT

Several problems must be solved in the construction, design, and operation of a nuclear fusion reactor. One of the chief problems in the manufacture of high-powered copper/polymer composite magnets is the difficulty to precisely control the fiber volume fraction. In this thesis, the effect of variations in fiber volume fraction on thermal stresses in copper/cyanate ester composite cylinders is investigated. The cylinder is a composite that uses copper wires that run longitudinally in a cyanate ester resin specifically developed by Composite Technology Development, Inc. This composite cylinder design is commonly used in magnets for nuclear fusion reactors. The application of this research is for magnets that use cylindrical coil geometry such as the Mega Amp Spherical Tokamak (MAST) in the UK. However, most stellarator magnet designs use complex geometries including the National Compact Stellarator Experiment (NCSX), and the Quasi-Poloidal Stellarator (QPS). Even though the actual stresses calculated for the cylindrical geometry may not be directly applicable to these projects, the relationship between fiber volume fraction and stresses will be useful for any geometry. The effect of fiber volume fraction on stresses produced by mechanical, thermal and magnetic loads on cylindrical magnet coils is studied using micromechanics with laminate plate theory (LPT) and finite element analysis (FEA).

Based on the findings of this research, variations in volume fraction do significantly affect the stress experienced by the composite cylinder. Over a range of volume fractions from 0.3 to 0.5, the LPT results demonstrate that thermally induced stresses vary approximately 30% while stresses due to pressure vary negligibly. The FEA shows that magnetic stresses vary much less at around only 5%. FEA results seem to confirm the LPT model. It was also concluded that the stress in the insulation layers due to all types of loadings is significant and must be considered when using this system in fusion applications.

TABLE OF CONTENTS

Chapter **Page**

I. INTRODUCTION 1

1.1 Energy 1

1.2 Nuclear Energy 2

1.2.1 MAST Tokamak 2

1.3 Use of Cyanate Ester Resin vs. Epoxy for Tokamak Insulation 3

1.4 Effects of Variation in Fiber Volume Fraction 6

II. REVIEW OF LITERATURE 9

2.1 Overview 9

2.2 Composite Materials 9

2.2.1 Copper Strand Based Composite Materials 10

2.2.2 Cyanate Ester Based Composite Materials 10

2.3 Fiber Volume Fraction Effect on Composite Materials 11

2.4 Shells of Revolution 12

2.5 Related Studies 12

III. MATHEMATICAL FORMULATION 15

3.1 Overview 15

3.2 Lamina Level Analysis 15

3.2.1 Micromechanics 15

3.2.2 Global Orthotropic Properties 20

3.2.3 Thermal Properties 22

Chapter **Page**

3.3 Laminate Level Analysis....24
3.3.1 Classical Laminate Plate Theory....24
3.3.2 Laminate Stiffness....26
3.3.3 Inclusion of Thermal Loading in Laminate Analysis....31
3.4 Magnetic Stress in a Cylinder....32

IV. METHODOLOGY....36
4.1 Overview....36
4.2 Modeling....36
4.2.1 Lamina Level Analysis....39
4.2.2 Laminate Level Analysis....39
4.3 MATLAB Programming Environment....40
4.3.1 Lamina Level Programming....40
4.3.2 Laminate Level Programming....41
4.4 Finite Element Analysis of Magnetic Loading....43
4.4.1 Multiphysics Application Modes....43
4.4.2 Subdomain and Boundary Settings....46
4.4.3 Meshing and Mesh Settings....46
4.5 Finite Element Analysis of Magnetic Loading with Rounded Conductor....48
4.6 Finite Element Analysis of Thermal and Mechanical Loading....51
4.6.1 Multiphysics Application Modes....52
4.6.2 Subdomain and Boundary Settings....52
4.6.3 Meshing and Mesh Settings....53

Chapter **Page**

V. RESULTS AND DISCUSSION 55

5.1 Mathematical Modeling 55

5.1.1 Lamina Level Analysis Effects.....55

5.1.2 Laminate Level Analysis Effects 65

5.2 Finite Element Analysis.....78

5.2.1 Magnetic Stress for Square Conductor 78

5.2.2. Magnetic Stress for Rounded Conductor.....91

5.2.3 Thermal Stress and Mechanical Stress 95

VI. CONCLUSIONS AND RECOMMENDATIONS.....98

6.1 Conclusions.....98

6.2 Recommendations.....100

REFERENCES.....102

APPENDIX.....106

LIST OF TABLES

Table **Page**

1.1 Comparison of Cyanate Ester and Epoxy Material Properties 5

4.1 Input Parameters for Laminate Analysis in MATLAB.....42

5.1 Material Properties for Lamina Level Analysis 56

5.2 Difference in Material Properties from 0.3 to 0.5 Volume Fractions 61

5.3 Material Properties for Laminate Level Analysis.....66

5.4 Composite Cylinder Specifications 67

5.5 Summary of Laminate Level Analysis Results for Composite Layers.....77

5.5 Summary of Laminate Level Analysis Results for Insulation Layer 77

5.7 Maximum Stresses and Displacement for Several Volume Fractions.....90

5.8 Summary of Thermal and Pressure Finite Element Analysis.....97

LIST OF FIGURES

Figure **Page**

1.1 Worldwide Energy Sources 1

1.2 Cutaway View of Conceptual Power Plant Design of MAST Tokamak 3

1.3 Cure Cycle for CTD-403....6

1.4 National Compact Stellarator Experiment, a Complex Geometry Coil 8

3.1 Proposed Methods of Finding Transverse Young's Modulus E_2....18

3.2 Proposed Methods of Finding Shear Modulus G_{12}....19

3.3 Schematic of Strain Magnification Due to a Transverse Load....19

3.4 Global Coordinate System (x,y,z) and Laminate Reference Directions (1,2,3)....20

3.5 Proposed Methods of Finding Transverse CTE α_2 24

3.6 Illustration of Kirchhoff's Hypothesis 26

3.7 Geometry of an N-Layered Laminate 27

3.8 Lamina Geometry 28

3.9 Laminate Orientation for 0° and 45° Samples....29

3.10 Earth's Magnetic Field....32

3.11 Geometry for Calculating Magnetic Field at *P* Due to Current *I* 33

3.12 Force Due to a Current Running Through Two Parallel Wires 34

3.13 Magnetic Field of a Current-Carrying Solenoid....35

4.1 Copper Conductor Wound in Cylindrical Form 37

4.2 Schematic Showing Fiber Orientation....38

4.3 Layout of Composite Wires 38

4.4 Autodesk Inventor Model of Coil 44

4.5 Drawing of COMSOL Magnetic Model....45

4.6 Close-up of the Coil 45

Figure **Page**

4.7 Editing Toolboxes Used in COMSOL 47

4.8 Mesh of Coil Geometry 47

4.9 Close-Up View of Coil Mesh 48

4.10 Photograph of a 2x2 Conductor Assembly 49

4.11 Magnetic Model with Rounded Edges 50

4.12 Close-Up of Rounded Edged Magnetic Model 50

4.13 Drawing of COMSOL Thermal and Mechanical Model 51

4.14 Subdomain Editing Toolbox for 3D Model 52

4.15 Initial Plane Sketch before Extrusion 53

4.16 Meshed 3D Coil Geometry 54

5.1 Young's Moduli E_1 and E_2 with Varying Fiber Volume Fraction 56

5.2 Poisson's Ratio v_{12} with Varying Fiber Volume Fraction 57

5.3 Shear Modulus G_{12} with Varying Fiber Volume Fraction 57

5.4 Variation of E_x as a Function of Orientation Angle ϑ 59

5.5 Variation of E_y as a Function of Orientation Angle ϑ 59

5.6 Variation of G_{xy} as a Function of Orientation Angle ϑ 60

5.7 Variation of v_{xy} as a Function of Orientation Angle ϑ 60

5.8 Variation of v_{yx} as a Function of Orientation Angle ϑ 61

5.9 Longitudinal and Transverse CTE's α_1 and α_2 with Varying Fiber Volume Fraction 63

5.10 Variation of α_x as a Function of Orientation Angle ϑ 64

5.11 Variation of α_y as a Function of Orientation Angle ϑ 64

5.12 Variation of α_{xy} as a Function of Orientation Angle ϑ 65

5.13 Stress in X Direction Due to Mechanical Loading 68

5.14 Stress in *Y* Direction Due to Mechanical Loading 69

5.15 Stress in *X*-*Y* Plane Due to Mechanical Loading 70

5.16 Stress in *X* Direction Due to Thermal Loading 71

Figure **Page**

5.17 Stress in *Y* Direction Due to Thermal Loading 72

5.18 Stress in *X*-*Y* Plane Due to Thermal Loading 73

5.19 Stress in X Direction Due to Combined Loading 74

5.20 Stress in *Y* Direction Due to Combined Loading 75

5.21 Stress in *X*-*Y* Plane Due to Combined Loading 76

5.22 Surface Magnetic Field 79

5.23 Surface Magnetic Flux Density 80

5.24 Magnetic Field Lines 80

5.25 Magnetic Field Lines, *r* Component 81

5.26 Magnetic Field Lines, *z* Component 81

5.27 Stress in the *r* direction σ_r 83

5.28 Close-up of the End of the Coil for Stress σ_r 84

5.29 Close-up of the Center of the Coil for Stress σ_r 84

5.30 Stress in the *z* direction σ_z 85

5.31 Close-up of the End of the Coil for Stress σ_z 85

5.32 Close-up of the Center of the Coil for Stress σ_z 86

5.33 Stress in the φ direction σ_φ 86

5.34 Close-up of the Coil for Stress σ_φ 87

5.35 Shear Stress τ_{rz} 87

5.36 Close-up of the End of the Coil for Stress τ_{rz} 88

5.37 Close-up of the Center of the Coil for Stress τ_{rz} 88

5.38 *r*-direction Displacement d_r 89

5.39 *z*-direction Displacement d_z 89

5.40 Total Displacement d_{tot} 90

5.41 Stress in the *r* direction σ_r for Rounded Edges 93

Figure **Page**

5.42 Stress in the *z* direction σ_z for Rounded Edges 93

5.43 Stress in the φ direction σ_φ for Rounded Edges 94

5.44 Shear Stress τ_{rz} for Rounded Edges 94

5.45 Stress with Insulation Boundary Removed 95

5.46 Thermal Stress in the *X* Direction 96

5.47 Thermal Stress in the *Y* Direction 96

LIST OF ABBREVIATIONS

NCSX	National Compact Stellarator Experiment
QPS	Quasi-Poloidal Stellarator
CTD	Composite Technology Development, Inc.
FEA	Finite Element Analysis
LPT	Laminate Plate Theory
CTE	Coefficient of Thermal Expansion
MAST	Mega Amp Spherical Tokamak
START	Small Tight Aspect Ratio Tokamak
ITER	International Thermonuclear Experimental Reactor
CE	Cyanate Ester
VPI	Vacuum Pressure Impregnation

LIST OF SYMBOLS

E_1	Elastic Modulus of Composite in Longitudinal Direction
E_2	Elastic Modulus of Composite in Transverse Direction
v_{12}	Poisson's Ratio of Composite
G_{12}	Shear Modulus of Composite
E_f	Elastic Modulus of Fiber Material
E_m	Elastic Modulus of Matrix Material
G_f	Shear Modulus of Fiber Material
G_m	Shear Modulus of Matrix Material
v_f	Poisson's Ratio of Fiber Material
v_m	Poisson's Ratio of Matrix Material
V_f	Fiber Volume Fraction of Composite
V_m	Matrix Volume Fraction of Composite
V_{voids}	Void Volume Fraction of Composite
E_x	Elastic Modulus of Composite in *X* Direction
E_y	Elastic Modulus of Composite in *Y* Direction
v_{xy}	Poisson's Ratio of Composite in *X*-*Y* Plane
G_{xy}	Shear Modulus of Composite in *X*-*Y* Plane
ϑ	Fiber Orientation Angle Relative to Reference *X* Axis
α_1	Coefficient of Thermal Expansion in Longitudinal Direction
α_2	Coefficient of Thermal Expansion in Transverse Direction
α_x	Off-Axis Coefficient of Thermal Deformation in *X* Direction
α_y	Off-Axis Coefficient of Thermal Deformation in *Y* Direction
α_{xy}	Off-Axis Coefficient of Thermal Deformation in *X*-*Y* Direction

Chapter I

INTRODUCTION

1.1 Energy

The current world economy is primarily based on energy, and as our need for energy increases with technology and population, we will need more and more clean, efficient sources of readily available energy. Energy currently comes from many sources, but the overwhelming majority of our energy needs are met using fossil fuels, with oil being the leading source of this energy. There is only a finite amount of these fossil fuels available for use, so research in the area of clean renewable energy is of the utmost importance. The current picture of our energy needs is quite bleak, since nearly 90% of our energy comes from nonrenewable fossil fuels, as shown in Figure 1.1.

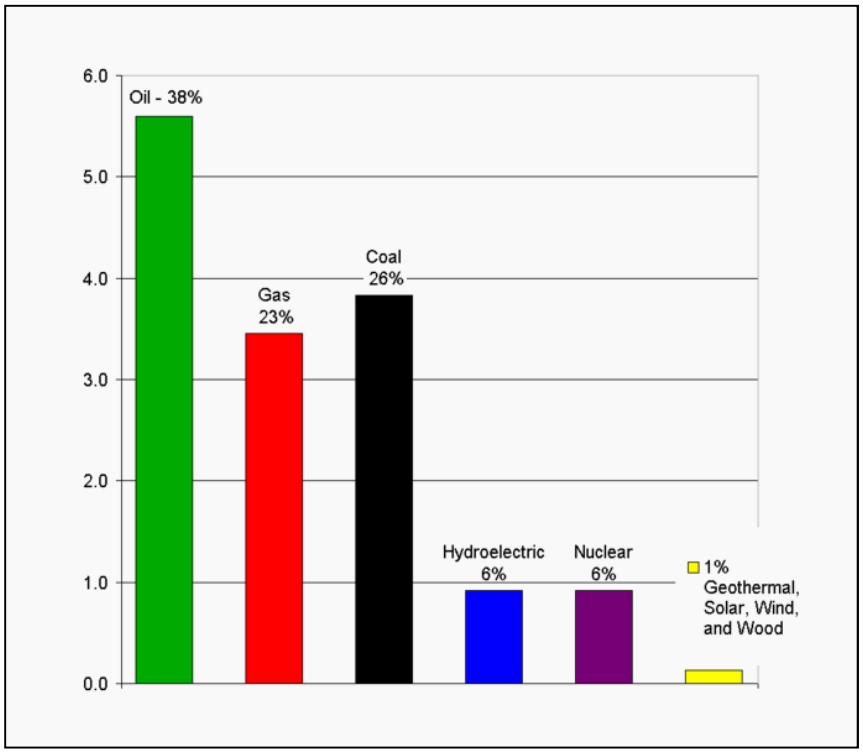


FIGURE 1.1 Worldwide Energy Sources [1].

1.2 Nuclear Energy

At present, the most viable source of clean, efficient, and abundant energy is in nuclear power. Nuclear energy sources have much less atmospheric pollution, while promising long-term energy production using less fuel due to the large energy density of nuclear fuels when compared to conventional fossil fuels. The current production of nuclear energy uses nuclear fission. Fission is the splitting of a large atom into several smaller, more stable atoms by striking it with a neutron. The resulting products have slightly less mass than the initial atom because the "missing" mass is converted directly into energy. The alternative to fission is nuclear fusion. Fusion is the combining of two small atoms (usually hydrogen isotopes) into a larger atom, with the conversion of some of the mass into energy. The advantage of fusion over fission is that it has the potential to have an even greater energy density than fissile fuels, would be completely self-sustaining once initiated, and produces less harmful wastes. However, fusion has many large obstacles that must be surmounted in order for it to become a viable energy source. Containment of the fusion reaction is the chief among these, as no current engineering material can withstand the extreme heat required in a fusion reaction. Naturally occurring fusion in the heart of stars is contained simply by the gravity of their enormous mass; synthetic reactions currently use high-powered magnetic fields for containment. The design, production, maintenance, and operation of these magnetic fields is the primary area of concern for future development of fusion sources of energy, as these magnetic fields confine and sustain the plasma required for fusion.

1.2.1 MAST Tokamak

The Mega Amp Spherical Tokamak (MAST), shown in Figure 1.2, is a program based in Culham, United Kingdom, to build a spherical cyanate ester based fusion tokamak as a proof-of-concept test of the spherical tokamak design [2]. MAST is the successor to the Small Tight Aspect Ratio Tokamak (START) program and a test model has been successfully built.

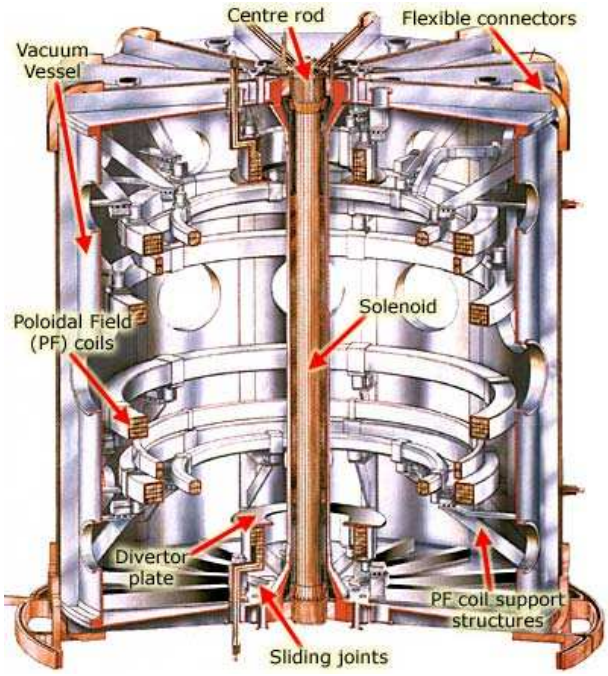


Figure 1.2 Cutaway View of Conceptual Power Plant Design of MAST Tokamak [2].

The tokamak is a magnetic confinement device that utilizes toroidal magnetic fields produced by an electric current to confine thermonuclear fusion plasma. It is distinct in its azimuthal symmetry and is one of the best developed fusion device classes known [3]. The principal objectives for developing the MAST device are to analyze and optimize key issues for the ITER (originally International Thermonuclear Experimental Reactor, now just ITER) project and to investigate the viability, longevity, and feasibility of a spherical design and of tokamaks in general.

1.3 Use of Cyanate Ester Resin vs. Epoxy for Tokamak Insulation

Conventionally, epoxy-based insulation systems have been used in tokamak production and testing. However, a cyanate ester resin would offer a number of advantages for insulation system application, including increased high temperature strength, greater radiation resistance, and drastically extended

pot life (the length of time that a catalyzed resin system retains a viscosity low enough to be used in processing) [4]. For these reasons Composite Technologies Development (CTD), Inc. has developed several cyanate ester based epoxy setups, most notably CTD-403. However, cyanate ester does have its drawbacks in that very little industrial research has been done, the gelling process is highly exothermic, the curing process requires that the resin must have no voids, and the resin is sensitive to moisture absorption and swelling. However, some thermo-mechanical testing and analysis has been performed by Voss, G. et al [5], and moisture degradation due to moisture effects has been explored in detail by Morgan, B. et al [6].

There are several key reasons that epoxy-based polymers are not as well suited to fusion insulation. Cyanate ester exhibits superior material properties to epoxy at critical temperatures necessary for fusion operation, and especially has much better elevated temperature properties, as is summarized in Table 1.1 below [5]. In addition to having very good mechanical properties, cyanate ester maintains its elevated temperature properties much better than epoxy and it demonstrates better resistance to damage from radiation that is characteristic of nuclear reactors [7]. Cyanate ester also exhibits improved toughness over epoxy. Significant work is being performed in testing and characterizing this new material to predict material performance under specific loading and to solidify the superiority of cyanate ester to epoxy polymers.

The typical cure cycle for CTD-403 cyanate ester is shown in Figure 1.3 below. As can be seen from this figure, the minimum time required to cure CTD-403 would be about 17 hours, and 22-40 hours is a typical cure time used in production with soakings at lower temperatures to avoid overheating the coil and to discourage a runaway exothermic reaction at voids and at rich resin areas [4]. CTD-403 has a very long pot life compared to other composites and the curing cycle is very straightforward and consistent.

Table 1.1 Comparison of Cyanate Ester and Epoxy Material Properties [4].

Property	Test Temp.	Unit	Cyanate Ester	Epoxy Resin
Tensile Strength	21 °C	Mpa	80.3	72.6
0.2% Proof Stress	21 °C	Mpa	66.7	58.1
Elongation at Failure	21 °C	%	2.64	2.9
Tensile Modulus	21 °C	GPa	3.49	3.2
Tensile Strength	70 °C	Mpa	64.4 (100 °C)	44.5
0.2% Proof Stress	70 °C	Mpa	49.0 (100 °C)	36.2
Elongation At Failure	70 °C	%	4.8 (100 °C)	3.7
Tensile Modulus	70 °C	GPa	2.36	2.16
Flexural Stress at Yield	21 °C	Mpa	163.0	120.2
Flexural Modulus	21 °C	GPa	3.95	3.39
Compression Modulus	21 °C	GPa	3.74	3.39
Max Compression Strength	21 °C	Mpa	158.2	118.5
Max Compression Strength	70 °C	Mpa	110.9	72.9
Max Compression Strength	100 °C	Mpa	87.7	13.0
Fracture Toughness K_{1c}	20 °C	$MNm^{-3/2}$	3.0	2.2
Glass Transition Temp. T_g	N/A	°C	158	121
Density	20 °C	Kg/m^3	1239	1207

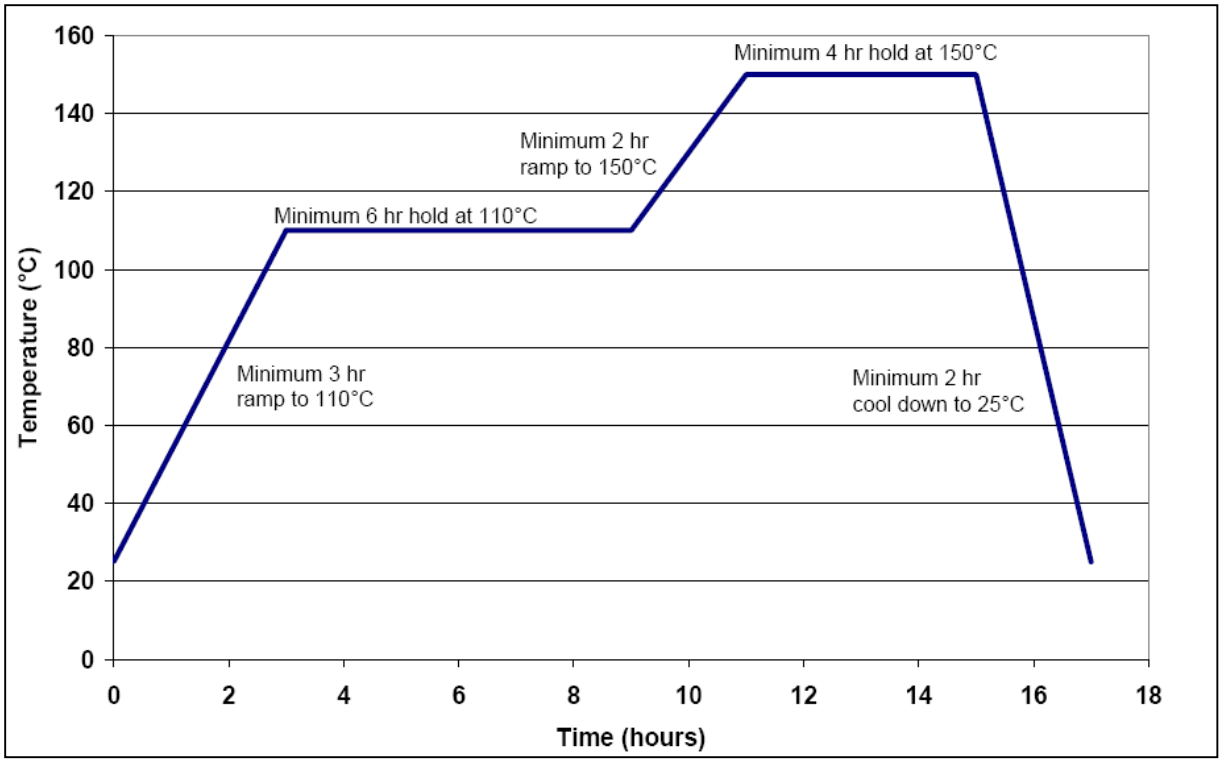


Figure 1.3 Cure Cycle for CTD-403 [6].

1.4 Effects of Variation in Fiber Volume Fraction

In a well-controlled VPI process, the fiber volume fraction will typically only vary by a few percent (±2% is probably a good estimate). In magnets the challenge is getting uniformly high fiber-volume contents. That often has more to do with the coil, resin flow path, and how well the coil is wound rather than problems with the resin processing. Thus you might get 40±2% fiber volume fraction in a coil rather than 50±2% [8]. The effects of variation in fiber volume fraction are important to characterize; although local variations are small, throughout the coil, fiber volume fraction can vary by 10% or more and it is difficult to produce a precise volume fraction throughout.

This research focuses on the effect of variation of fiber volume fraction in a copper/cyanate ester cylindrical coil on thermal, mechanical, and magnetic stresses and strains. The application of this research is for magnets that use cylindrical coil geometry such as the Mega Amp Spherical Tokamak

(MAST) in the UK. In some stellarator magnet designs, such as the National Compact Stellarator Experiment (NCSX) (seen in Figure 1.4) and the Quasi-Poloidal Stellarator (QPS), the coil geometries are complex. While the actual stress values calculated from a simple cylindrical geometry may not be directly applicable to these more complex shapes, the relationship between fiber volume fraction and thermal stresses will be useful for any geometry.

The analysis of the composite cylinder was principally achieved through two methods: laminate plate theory (LPT), and model verification using finite element analysis (FEA). Essentially, the LPT was broken further into two parts: lamina level analysis and laminate level analysis. The lamina level analysis is used to determine lamina stiffness as a whole using the properties of the copper strands and the cyanate ester matrix. Variations in fiber volume fraction were reflected in the stiffness moduli E_x, E_y, G_{xy}, and ν_{xy}. Also, thermal expansion coefficients of the lamina were calculated from the thermal expansion coefficients of the copper fiber and polymer matrix. The composite showed strong dependence on fiber volume fraction variation in that for E_x, E_y, and G_{xy} increase in volume fraction caused an increase in these properties; for ν_{xy} the opposite trend was found. For the laminate level analysis, the cylinder had mechanical and thermal loadings applied in order to calculate the stress in the cylinder.

The FEA was used primarily to calculate the stress and strain due to magnetic loading of the cylinder. This type of loading is complex and would be difficult to calculate with the LPT. However, finite element simulation took much of the difficulty out of modeling this type of loading. The finite element models developed are also used to verify the results of the LPT for mechanical and thermal loadings of the cylinder.

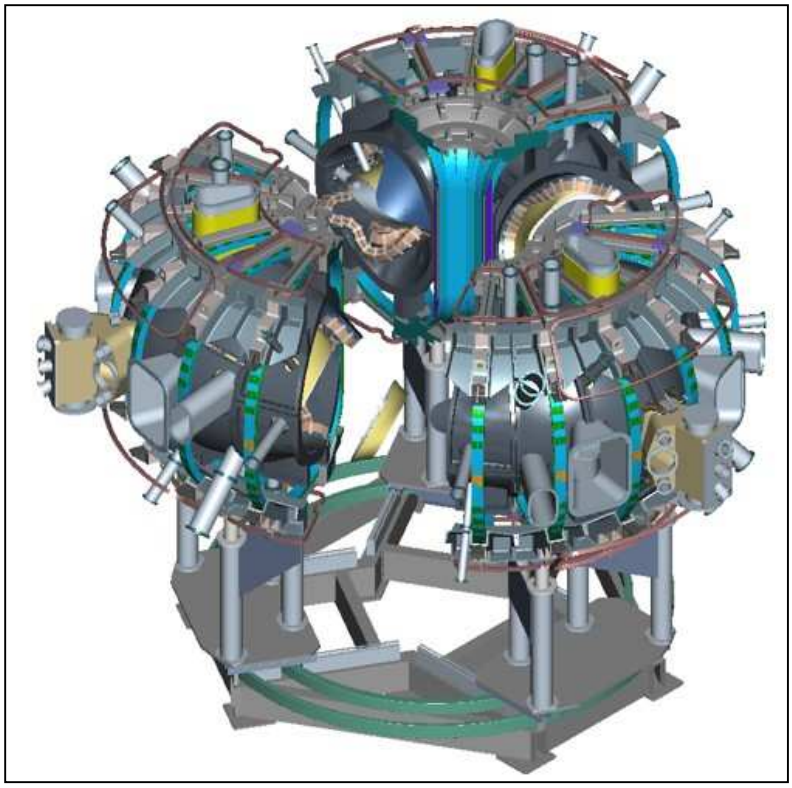


Figure 1.4 National Compact Stellarator Experiment, a Complex Geometry Coil [9].

Very little literature is available on the effects on a composite of varying the volume fraction of wires, and this is a very important parameter to monitor and predict when considering what material to use and how best to manufacture it. Several models have been developed to help predict exactly how a copper/cyanate ester composite will behave under varying loads and with varying fiber volume fraction. These loadings explored are intended to duplicate expected stresses experienced by the coil under a real duty cycle and should help predict material behavior in a nuclear fusion environment. Once the models are developed, then all that is needed is to input the specific material properties of the coil and its behavior can be characterized.

Chapter II

REVIEW OF LITERATURE

2.1 Overview

When attempting to describe the performance of a cyanate ester composite, one of the most important manufacturing variables is the fiber volume fraction [10]. Since the performance of a composite will depend on the properties of the constituents, namely the wires and the matrix, it is essential to characterize the effect of varying the mixture of both components in the composite. Once the effect of fiber volume fraction on stress in the material is understood, then models can be developed to accurately predict how varying the constituents' volume fraction will affect the load bearing capacity of the material. This research will provide an understanding of how the fiber volume fraction affects the load carrying capacity of a copper/polymer composite cylinder under thermal, mechanical and magnetic loads.

2.2 Composite Materials

In the broadest sense, the word "composite" denotes something that consists of two or more distinct, different parts that are combined together. In the context of its use in *composite materials* (usually just shortened to *composites*) a composite is an amalgamation of two (or rarely, more than two) materials with different properties and natures that allow the attainment of a material with a specific performance greater than that of the constituents taken separately [10]. The principle advantage of using a composite over a conventional engineering material is that composite materials usually exhibit the best qualities of their components and sometimes even possess some qualities neither constituent had [12]. There are three principle categories of composite materials: *fibrous composites, laminated composites, and particulate composites* [11]. Fibrous or fiber-reinforced composites are the most

common type and consist of long, continuous fibers imbedded in a polymer matrix. Laminated composites (not to be confused with laminae) are composed of layers of different materials adhered together. Particulate or particle-reinforced composites have a matrix like fibrous composites, but rather than fibers they have particles imbedded in the matrix.

2.2.1 Copper Strand Based Composite Materials

The cyanate ester/copper strand composite that is used in this research is most similar to a fiber-reinforced composite, but it is not really correct to classify it as such. The role of the copper wires in this composite is not to strengthen or stiffen the cylinder as is the case for fibrous composites. Copper wires are the current carriers and the role of the resin is to act as the insulation material and to provide support to the wires. An important property for the insulation material used in high voltage applications is the *dielectric strength*. The dielectric strength of a material is the voltage that will produce a rupture in the insulation divided by its thickness [6]. CTD-403 possesses a high dielectric strength of 105 kV/mm giving it superior electrical insulation properties and making it an attractive matrix material to be used in fusion applications. Furthermore, CE was found to maintain high dielectric strength even when exposed to high humidity and temperature for prolonged periods of time [6].

2.2.2 Cyanate Ester Based Composite Materials

Cyanate esters have recently emerged as a new class of thermosetting resin that has many applications to the aerospace and electronics industry [12]. The primary reason that these industries find cyanate ester to be very attractive is that CE possesses a good combination of high temperature stability and excellent mechanical properties. Additionally, cyanate esters possess excellent adhesive properties, are more resistant to the absorption of moisture than comparable thermosetting polymers, and have very low dielectric constants [13]. The adhesive properties make CE ideal as the matrix in a fiber reinforced

composite since the shearing and transverse strength of the material depends largely on the adhesive ability of the matrix to the wires; additionally, moisture absorption tends to cause materials to swell and experience a loss in mechanical properties as explored by Morgan, B.I. [6] so low moisture absorption properties of cyanate esters are very attractive. Cyanate ester possesses a uniquely low cross link density in its structural makeup making it naturally tougher than most other high-temperature thermosets [12, 13]. Since fusion composite applications also demand a material with these desirable qualities, one could add fusion research as an emerging industry that can find many applications for cyanate ester based composite materials. However, these advantages come at a very high monetary cost that may not be justified except in the aforementioned industries [13]. Also, the relatively long and high temperature treatment cycle shown in Figure 1.3 required to cure CE can be seen as a disadvantage when comparing with epoxy based matrix materials for a composite.

2.3 Fiber Volume Fraction Effect on Composite Materials

The fiber volume fraction, V_f, and is defined as

$$V_f = \frac{v_f}{v_c} \tag{2.1}$$

Where v_f is the volume of wires and v_c is the total composite volume. The total volume of the composite is composed of the volume of wires and matrix, and the volume of voids [14]. This equation therefore is

$$V_f + V_m + V_{voids} = 1 \tag{2.2}$$

In vacuum-pressure impregnated coils, the void content in the polymer is considered to be less than 1% (and is quite often less than 0.5%). Void volume is challenging to measure with absolute certainty because the void size can be quite small (less than a few microns). Because it is so small, the void content is generally considered to be zero [8]. It is also not unreasonable to assume that any test article would have the same void content as a coil, so test data probably is very representative of the values

input into a model. For this reason the void fraction in the models developed is set as zero, leading to the following equation

$$V_m = 1 - V_f \tag{2.3}$$

This assumption will be used in the analysis of cyanate ester/copper composite materials.

2.4 Shells of Revolution

When analyzing the composite cylinder, the pressure vessel may be considered a *shell of revolution* due to its curved nature. A shell has all the characteristics of plates, with one additional attribute: curvature. Shells offer a number of advantages in engineering structures and applications, including their efficiency of load-bearing behavior, high degree of reserved strength and structural integrity, high strength to weight ratio, very high stiffness, and effective containment and utilization of space [15]. Although shells do have these advantages, when considered as a three-dimensional body the calculations involved in their analysis are generally very difficult and complicated. However, Ventsel [15] has suggested that for sufficiently thin shells, the analysis can be restricted to the middle surface such that the shell problem can now be approximated as a two-dimensional thin plate, greatly simplifying the calculations. It is with this approximation in mind that the theories utilized in the mathematical formulation are developed and implemented.

2.5 Related Studies

As stated previously, there is not a lot of research available in the area of the performance of a composite material as fiber volume fraction is varied. Furthermore, there is little in the area of the use of copper or even metals in general as fiber reinforcement in composite materials, and to the author's knowledge no research exists on the effect of fiber volume fraction on cyanate ester composites as these are a relatively new material class. However, some research has been performed previously.

McMillan, J.P. [16] performed a study on the effects of fiber volume fraction on the elastic stability of specially orthotropic plates. In his findings, McMillan reports that from a micromechanics and structural analysis standpoint, increasing fiber volume fraction of a composite plate will dramatically increase its ability to withstand compressive loads. Since his results are for a boron-epoxy composite, and all composite materials behave differently, one cannot assume that these results are applicable to all fiber-reinforced composites. However, he does state that increasing the fiber content of a unidirectional, specially orthotropic and transversely isotropic composite material will increase its elastic stability. Therefore these trends can be applied to any continuous fiber embedded in an epoxy or epoxy-like matrix.

Sayre, J.R. [17] performed a study on the effects of fiber volume fraction on mechanical properties of filament-wound, polypropylene-glass tubes. Sayre performed a study on varying the fiber volume fraction using three V_f's: 0.34, 0.37, and 0.46. It was found that the strength and modulus didn't vary significantly form one sample to the other. It was also concluded that fiber volume fraction isn't a controlling factor in mechanical properties. However, the methods used in reference 17 for controlling V_f were crude and probably not uniform. Sayre states that the manner used to increase fiber volume fraction was to simply "squeeze out" polypropylene at the fiber exit. He also states that as he increased fiber volume fraction, that voids most likely increased in the composite, representing areas of stress concentration that could promote crack growth and/or reduce the adhesion of the fibers to the matrix. Upon inspection of Sayre's results, it was observed that both tensile and flexural properties increased as volume fraction was increased, but the difference between 0.34 and 0.37 was much more pronounced than that between 0.37 and 0.46. It can therefore be concluded from Sayre's results that at lower volume fractions, increasing the amount of wires has a large effect but as this fiber fraction increases, its effect on mechanical properties decreases somewhat.

Kavuri, H. [18] performed a study on cure behavior and elastic modulus characterization of a QPS coil. He found that both CTD-404 and CTD-101K resins had low cure stresses but high cool down stresses. Furthermore, he found that the Young's modulus for CTD-101K at liquid nitrogen temperatures did not differ significantly from the value at room temperature. Since CTD-404 is essentially the same as CTD-403, the results were directly applied to the research presented in this thesis. CTD-101K is an epoxy based resin so although the results for its analysis are not exactly applicable, they can be held to be generally true [8].

Chapter III

MATHEMATICAL FORMULATION

3.1 Overview

A large portion of the research undertaken involved the application of micromechanics and classical laminate plate theory to predict the behavior and performance of a cyanate ester/copper composite material subjected to thermal and mechanical loads. The methodology used is briefly developed in the preceding sections. Many leading texts in the area of composites, laminates, and plate and shell theory are used to formulate a process for finding stress and strain in the composite, and to see how varying fiber volume fraction affects these stresses.

3.2 Lamina Level Analysis

3.2.1 Micromechanics

Micromechanics is the study of a composite material as it pertains to the interaction of the constituents of the heterogeneous composite [11]. Therefore micromechanics deals with the individual components of the composite, namely the wires and the matrix, and how their properties can be used to find the orthotropic behavior of the composite as a whole. Before the overall properties can be found, the properties of the wires and matrix themselves must be found, namely E_f, E_m, G_f, G_m, ν_f, and ν_m. Both the copper wires and the cyanate ester isotropic bulk materials; the shear modulus G for both materials can be found using the elementary mechanics of materials relation.

$$G = \frac{E}{2(1+\nu)} \tag{3.1}$$

Additionally, the fiber volume fraction V_f and the matrix volume fraction V_m are found using equations (2.1) and (2.3) as discussed previously. Once the pertinent constituent properties are known and

characterized, then properties of the composite material as a whole can be found. Most texts on composite materials suggest using a mechanics of materials approach to finding these stiffness constants. Several texts suggest a *rule of mixtures* expression for the apparent Young's modulus E_1 and for the Poisson's ratio v_{12}, including Hyer [19], Jones [11], Berthelot [10], and Chawla [20]. These equations are shown below.

$$E_1 = E_L = \sum E_i V_i = E_f V_f + E_m V_m \tag{3.2}$$

$$\nu_{12} = V_f \nu_f + V_m \nu_m \tag{3.3}$$

These are called rules of mixtures because they are linear relations with respect to the fiber volume fraction and thus depend solely on the mixture of fibers and matrix. However, these sources suggest not using the rule of mixtures for the other constants, G_{12} and v_{12}. Hyer [19], Tsai [14] and Bertholet [10] suggest using the following equations.

$$E_2 = \left(\frac{V_f}{E_f} + \frac{V_m}{E_m}\right)^{-1} \tag{3.4}$$

$$G_{12} = \left(\frac{V_f}{G_f} + \frac{V_m}{G_m}\right)^{-1} \tag{3.5}$$

Gibson [21] proposes that the above standard equations do not correspond well with experimental data so the equations must be modified. His derivation suggests that transverse and shear moduli are more accurately functions of the root of fiber volume fraction and advocates the following equations be used.

$$E_2 = E_m\left[\left(1 - \sqrt{V_f}\right) + \frac{\sqrt{V_f}}{1 - \sqrt{V_f}\left(1 - \frac{E_m}{E_f}\right)}\right] \tag{3.6}$$

$$G_{12} = G_m\left[\left(1 - \sqrt{V_f}\right) + \frac{\sqrt{V_f}}{1 - \sqrt{V_f}\left(1 - \frac{G_m}{G_f}\right)}\right] \tag{3.7}$$

Jones [11] derives the transverse and shear moduli by assuming the same transverse and shear stresses are experienced by the fibers and matrix, and finds the strain by finding the average stress over the corresponding volume of material. Since stress and strain are related through the moduli, these moduli can be solved for in the equations. Therefore Jones has put forward the following nondimensionalized equations.

$$E_2 = \frac{E_m}{V_m + V_f(\frac{E_m}{E_f})} \tag{3.8}$$

$$G_{12} = \frac{G_m}{V_m + V_f(\frac{G_m}{G_f})} \tag{3.9}$$

Chawla [20] derives the transverse and shear moduli slightly differently. He starts with the same general assumptions as Jones, but using the knowledge that experimental results do not follow Jones' results exactly, Chawla has provided modified equations describing these constants. Much like Gibson's results, Chawla's models for E_2 and G_{12} depend on the root of V_f rather than volume fraction directly, and he believes this modification results in better agreement between experimental results and predicted trends. Therefore Chawla recommends using

$$E_2 = \frac{E_m}{1 - \sqrt{V_f}\left(1 - \frac{E_m}{E_f}\right)} \tag{3.10}$$

$$G_{12} = \frac{G_m}{1 - \sqrt{V_f}\left(1 - \frac{G_m}{G_f}\right)} \tag{3.11}$$

A plot of these various sources' normalized curves is shown in Figures 3.1 and 3.2. These have both been normalized in order to make a better comparison. As can be seen, the curves all follow similar trends except for Gibson and Chawla; however, Hyer and Tsai suggest that their formulas are consistently lower than experimental data and recommend using partitioning factor to adjust the curves up. In addition, Gibson justifies his variation because of the over-simplification involved in the rule of mixtures

approach. This is because strain in the transverse direction is heterogeneous as is illustrated in Figure 3.3. In slice a-a, the strain will be placed mostly on the matrix since the matrix modulus is less in magnitude than the fiber modulus. However, slice b-b has no wires in it so the entire load is born by the resin. This discrepancy in loading because of inherent irregular fiber distribution results in the average matrix strain in slice b-b being smaller than that of slice a-a. This effect is known as *strain magnification* in the matrix. Chawla does not address the issue, and it is observed that he did attempt to rectify the error in the rule of mixtures model. However, his equations do not follow the other trends, so his equations are disregarded. Because of this shortcoming in rule of mixtures, and the fact that Hyer and Tsai also address this issue in a similar manner, Gibson's equations for E_2 and G_{12} (3.6 and 3.7) are preferred.

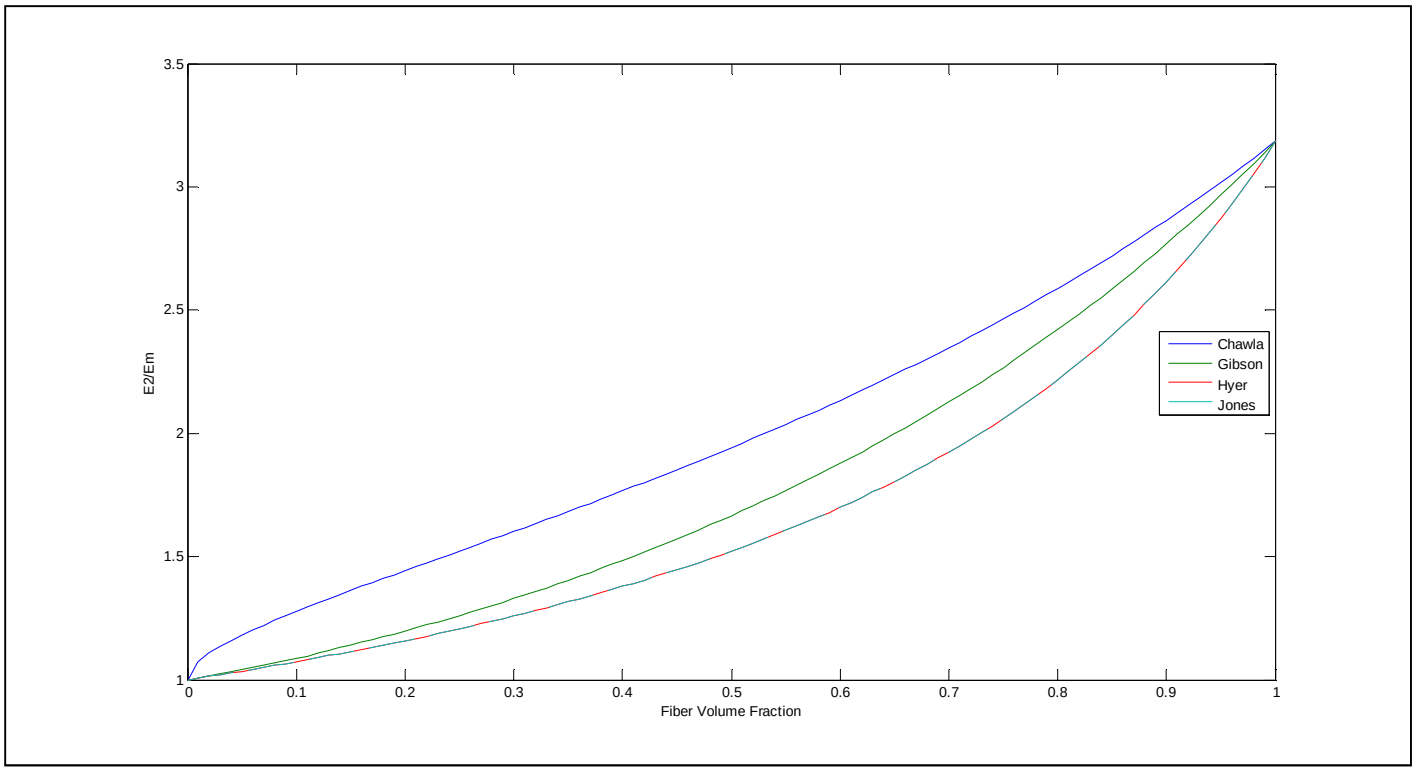


Figure 3.1 Proposed Methods of Finding Transverse Young's Modulus E_2. Gibson's equation is used in the analysis instead of those presented by Chawla, Hyer, and Jones.

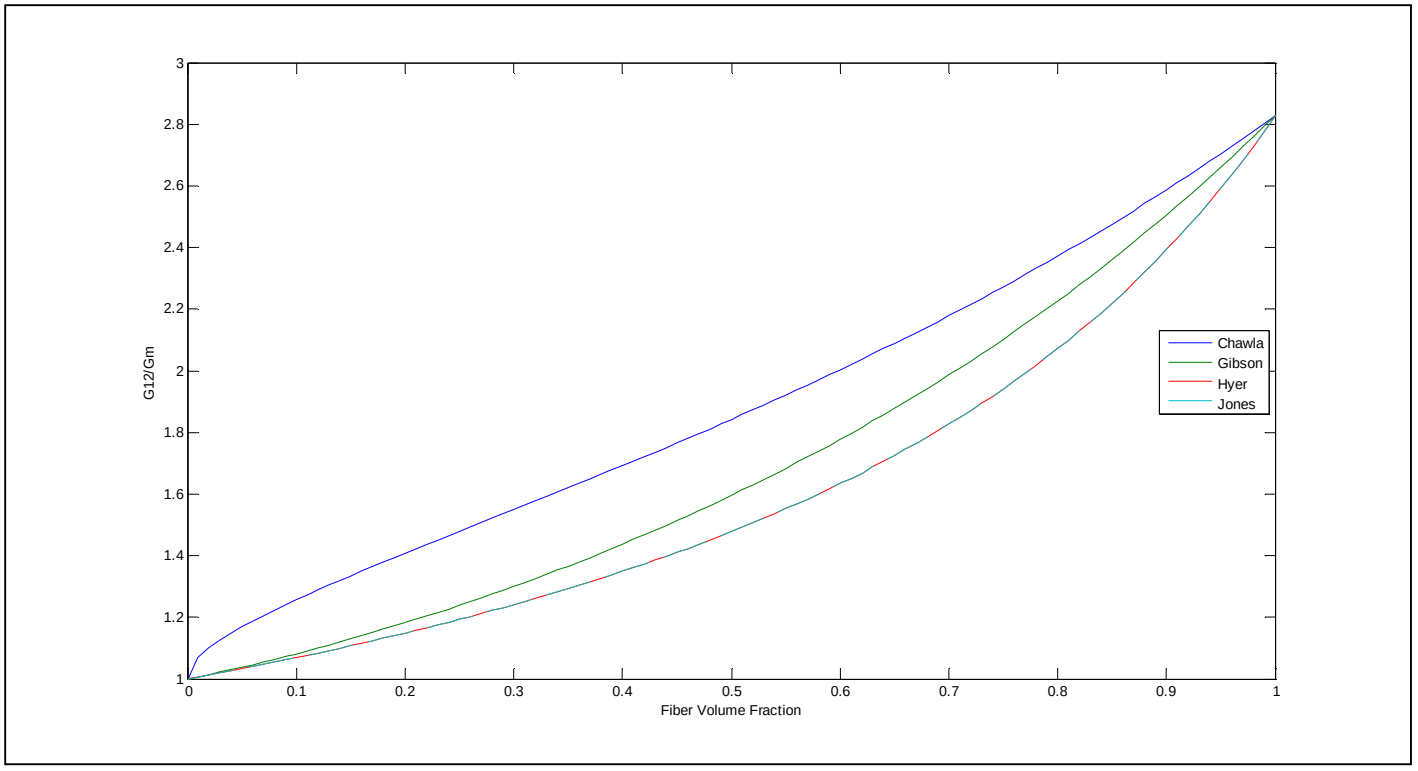


Figure 3.2 Proposed Methods of Finding Shear Modulus G_{12}. Gibson's equation is used in the analysis instead of those presented by Chawla, Hyer, and Jones.

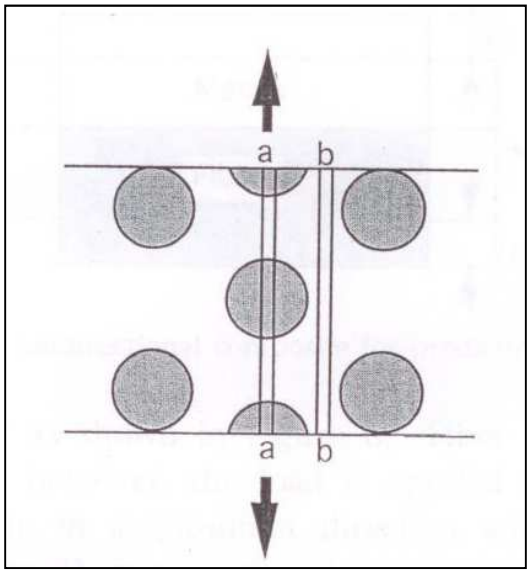


Figure 3.3 Schematic of Strain Magnification Due to a Transverse Load [21].

3.2.2 Global Orthotropic Properties

When using fiber reinforced composite laminae, one important aspect of their application is in the use of multiple fiber orientations. Most structural laminates are composed of multiple laminae, and usually each lamina is oriented in a specific fiber direction that is different from adjacent layers [19]. This is known as off-axis condition, where the wires are not aligned with the *X* axis. Off-axis condition frequently occurs in a structure that consists of a laminate of multiple fiber orientations. Since the overall behavior of the laminate is important, we must be able to account for this off-axis behavior. A schematic illustrating this off-axis orientation is shown in Figure 3.4.

In order to account for fiber direction offset ϑ in the material property equations, *transformation relations* must be used. These transformation relations are used with the offset angle to find how stiffness parameters vary when the lamina is oriented off-axis.

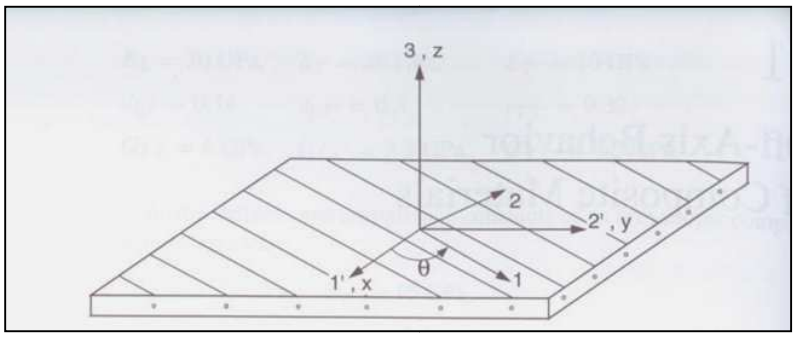


Figure 3.4 Global Coordinate System (x,y,z) and Laminate Reference Directions (1,2,3) [10].

Hyer [19] suggests the following standard properties for off-axis orientations.

$$E_x = \frac{E_1}{cos^4\theta+\left(\frac{E_1}{G_{12}}-2\nu_{12}\right)cos^2\theta sin^2\theta+\frac{E_1}{E_2}sin^4\theta} \tag{3.12}$$

$$E_y = \frac{E_2}{cos^4\theta+\left(\frac{E_2}{G_{12}}-2\nu_{21}\right)cos^2\theta sin^2\theta+\frac{E_2}{E_1}sin^4\theta} \tag{3.13}$$

$$G_{xy} = \frac{G_{12}}{cos^4\theta+sin^4\theta+2[2\frac{G_{12}}{E_1}(1+2\nu_{12})+2\frac{G_{12}}{E_2}-1]cos^2\theta sin^2\theta} \tag{3.14}$$

$$\nu_{xy} = \frac{\nu_{12}\left(cos^4\theta+sin^4\theta\right)-\left(1+\frac{E_1}{E_2}-\frac{E_1}{G_{12}}\right)cos^2\theta sin^2\theta}{cos^4\theta+\left(\frac{E_1}{G_{12}}-2\nu_{12}\right)cos^2\theta sin^2\theta+\frac{E_1}{E_2}sin^4\theta} \tag{3.15}$$

$$\nu_{yx} = \frac{\nu_{21}(cos^4\theta+sin^4\theta)-\left(1+\frac{E_2}{E_1}-\frac{E_2}{G_{12}}\right)cos^2\theta sin^2\theta}{cos^4\theta+\left(\frac{E_2}{G_{12}}-2\nu_{21}\right)cos^2\theta sin^2\theta+\frac{E_2}{E_1}sin^4\theta} \tag{3.16}$$

However, Bertholet [10] and Jones [11] propose

$$E_x = [\frac{1}{E_1}cos^4\theta + \frac{1}{E_2}sin^4\theta + \left(\frac{1}{G_{12}} - 2\frac{\nu_{12}}{E_1}\right)cos^2\theta sin^2\theta]^{-1} \tag{3.17}$$

$$E_y = [\frac{1}{E_1}sin^4\theta + \frac{1}{E_2}cos^4\theta + \left(\frac{1}{G_{12}} - 2\frac{\nu_{12}}{E_2}\right)cos^2\theta sin^2\theta]^{-1} \tag{3.18}$$

$$G_{xy} = [2\left(\frac{2}{E_1} + \frac{2}{E_2} + 4\frac{\nu_{12}}{E_1} - \frac{1}{G_{12}}\right)cos^2\theta sin^2\theta + \frac{1}{G_{12}}(sin^4\theta+cos^4\theta)]^{-1} \tag{3.19}$$

$$\nu_{xy} = E_x[\frac{\nu_{12}}{E_1}(cos^4\theta + sin^4\theta) - \left(\frac{1}{E_1} + \frac{1}{E_2} - \frac{1}{G_{12}}\right)sin^2\theta cos^2\theta] \tag{3.20}$$

These two methods were compared and gave identical curves for all of the properties shown, except for the Poisson's ratio due to stress in the *y* direction ν_{yx} since the other authors do not account for it. In fact, the corresponding equations in (3.12) through (3.16) and (3.17) through (3.20) not only give

identical results, but are the same equations written differently, so they must give the same results. It is also of note that although Hyer, Berthelot, and Jones derived them, the above equations did not originate with these authors but are commonly used in micromechanical analysis. Equations (3.12) through (3.16) are used for the analysis simply due to equation layout preference, but either set of equations would give the same results and could have been used.

3.2.3 Thermal Properties

In addition to the mechanical properties that relate mechanical strains to stresses, thermal properties of the composite were also analyzed. The thermal analysis of the laminate was based on finding the coefficient of thermal expansion (CTE) of the lamina. Similarly to the previous review, thermal properties were first found for the composite from the properties of the wires and matrix, and then global laminate properties were developed from these. In Hyer's [19] model, the composite coefficients of thermal expansion in the fiber and transverse directions α_1 and α_2 are found using an alternative rule of mixtures model similar to that of the transverse modulus. This modified method is used for the same reason that it is implemented in E_2: to account for the interaction between the wires and matrix elements. Unique strains due to an interaction between the different expansion properties of the wires and matrix must be built into the model. Because of this, the models are

$$\alpha_1 = \frac{(\alpha_f E_f - \alpha_m E_m)V_f + \alpha_m E_m}{(E_f - E_m)V_f + E_m} \tag{3.21}$$

$$\alpha_2 = \alpha_m + (\alpha_f - \alpha_m)V_f + \left(\frac{E_f \nu_m - E_m \nu_f}{E_1}\right)(\alpha_m - \alpha_f)(1 - V_f)V_f \tag{3.22}$$

For the transverse thermal expansion constant, the final term is an adjustment from the rule of mixtures equation which is

$$\alpha_2 = \alpha_m + (\alpha_f - \alpha_m)V_f \tag{3.23}$$

Chawla [20] recommends the following formulas for finding the thermal expansion constants

$$\alpha_1 = \frac{V_f E_f \alpha_f + (1-V_f) E_m \alpha_m}{E_f V_f + E_m (1-V_f)} \tag{3.24}$$

$$\alpha_2 = \alpha_f \sqrt{V_f} + \alpha_m \left(1 - \sqrt{V_f}\right)\left(1 + \frac{V_f \nu_m E_f}{E_f V_f + E_m V_m}\right) \tag{3.25}$$

Both authors' models give the exact same trend for α_1; however, they do differ some for transverse thermal expansion coefficient. Because of this, the trends were compared and are shown in Figure 3.5.

As can be seen in this figure, the adjustments suggested by Hyer are small while those put forward by Chawla differ greatly from the rule of mixtures plot. Given that Hyer's equations are linear as is expected for transverse CTE behavior, and that Chawla's results previously were disregarded, equations (3.21) and (3.23) are used for the thermal analysis.

Just as the mechanical properties of a fiber reinforced orthotropic laminate vary with fiber orientation, the thermal properties as well will change with the fiber direction. Hyer [19] suggests that the coefficients of thermal deformation in the off-axis system can readily be found by using

$$\alpha_x = \alpha_1 cos^2\theta + \alpha_2 sin^2\theta \tag{3.26}$$

$$\alpha_y = \alpha_1 sin^2\theta + \alpha_2 cos^2\theta \tag{3.27}$$

$$\alpha_{xy} = 2(\alpha_1 - \alpha_2) cos\theta sin\theta \tag{3.28}$$

As with the mechanical properties, these off-axis thermal properties can be used now to characterize the behavior of a laminate with multiple fiber orientations.

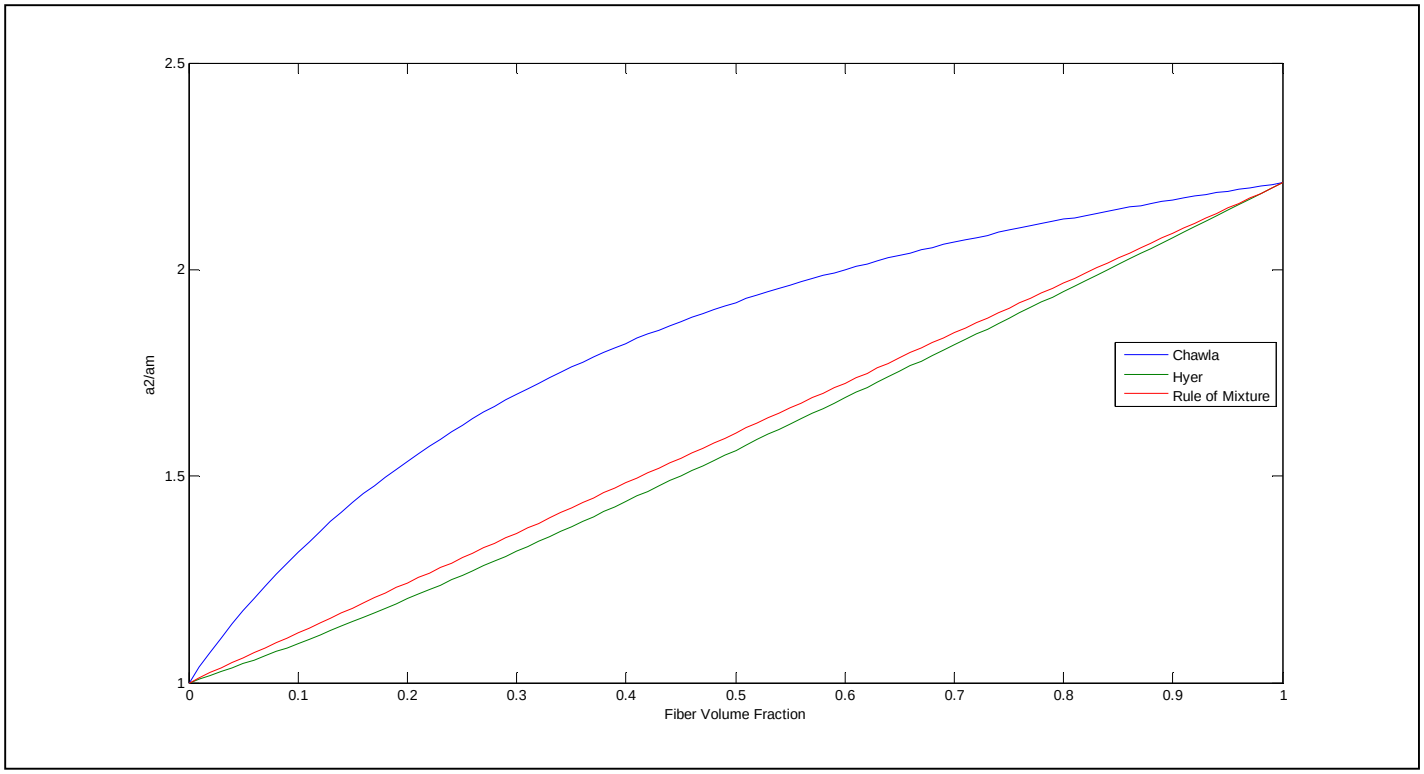


Figure 3.5 Proposed Methods of Finding Transverse CTE α_2. Rule of mixture equation is used instead of Chawla and Hyer.

3.3 Laminate Level Analysis

3.3.1 Classical Laminate Plate Theory

Classical laminate plate theory is the development of governing equations to use when dealing with composite plates. A *plate* is a structural element with planform dimensions that are large compared to its thickness and is subjected to loads that cause bending deformation in addition to stretching [22]. Euler-Bernoulli beam theory is based on the hypothesis that a straight line normal to the beam axis before bending remains (1) straight, (2) inextensible, and (3) normal to the beam after deformation. An extension of Euler-Bernoulli beam theory is Kirchhoff plate theory or *classical plate theory* [10, 22]. The displacement field is found based on the *Kirchhoff hypothesis* of three parts:

(1) Straight lines perpendicular to the mid-surface (i.e., transverse normals) before deformation remain straight after deformation.
(2) The transverse normals do not experience elongation (i.e., they are inextensible).
(3) The transverse normals rotate such that they remain perpendicular to the middle surface after deformation.

The chief implication of Kirchhoff's hypothesis is that it vastly simplifies the analysis of plates and thus plate bending. Since there is no mention of plate material properties, the subject of lines remaining straight is strictly a kinematic and geometric issue. This is important because it means that if we accept the validity of the hypothesis, then we assume it is valid for the wide range of complicated material properties inherent in fiber-reinforced composite materials [19]. A geometric example of the Kirchhoff hypothesis is shown in Figure 3.6. The plate in part (c) has allowed the lines to distort such that they are no longer perpendicular to the middle surface, whereas in part (b) the lines are still perpendicular to the middle surface and thus adhere to Kirchoff's hypothesis.

Laminate stiffness can be found using Kirchhoff's hypothesis and another concept that stems from classical plate theory: classical lamination theory. The key to classical lamination theory is that if the strains and curvatures of the middle surface - $\varepsilon_x^o, \varepsilon_y^o, \gamma_{xy}^o, \kappa_x^o, \kappa_y^o, \kappa_{xy}^o$- are found, then the strain distribution through the thickness of the laminate can be computed [19]. As stated before, this drastically simplifies the analysis, especially for complicated multi-layered laminates.

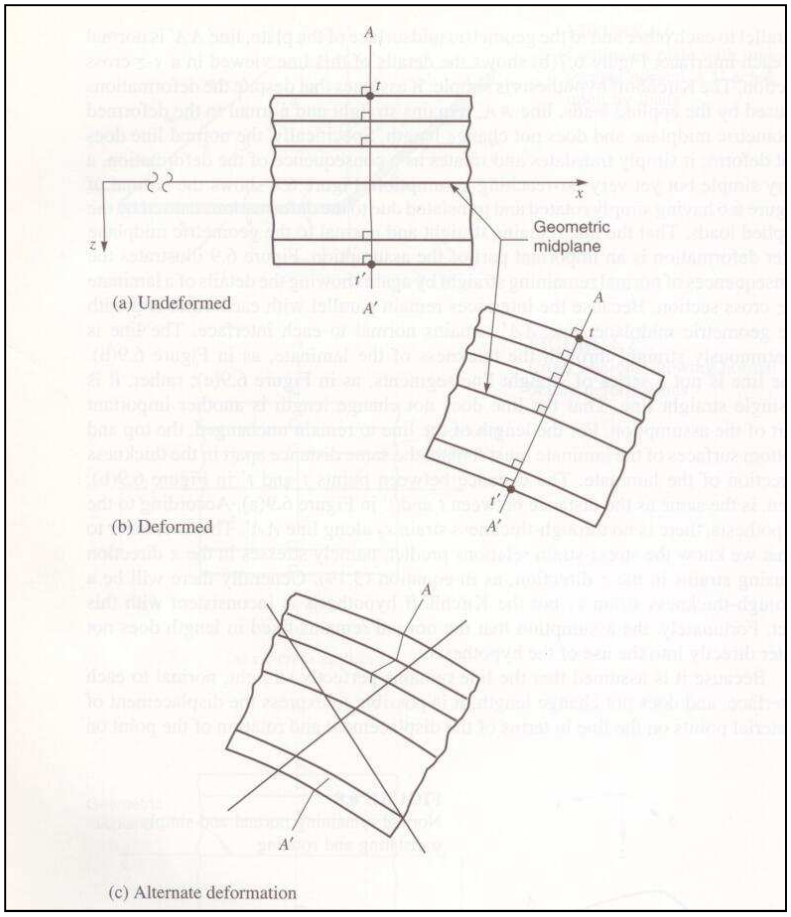


Figure 3.6 Illustration of Kirchhoff's Hypothesis [19].

3.3.2 Laminate Stiffness

The starting point for this analysis is to find the laminate stiffness matrix. For the models being developed, this includes a matrix for both the composite and for the insulation wrap. The compliance matrix (also known as the reduced stiffness matrix) is representative of the material properties calculated in the lamina analysis. For an orthotropic material like copper/cyanate ester composite, the compliance matrix is defined as [19]

$$\begin{Bmatrix} \sigma_1 \\ \sigma_2 \\ \tau_{12} \end{Bmatrix} = \begin{bmatrix} Q_{11} & Q_{12} & 0 \\ Q_{21} & Q_{22} & 0 \\ 0 & 0 & Q_{66} \end{bmatrix} \begin{Bmatrix} \varepsilon_1 \\ \varepsilon_2 \\ \gamma_{12} \end{Bmatrix} \tag{3.29}$$

The reduced stiffness matrix is the 3x3 *Q* matrix and is used to translate stress from strain. The components of the reduced stiffness matrix are defined as

$$Q_{11} = \frac{E_1}{1-\nu_{12}\nu_{21}}; \quad Q_{22} = \frac{E_2}{1-\nu_{12}\nu_{21}}; \quad Q_{12} = Q_{21} = \frac{\nu_{12}E_2}{1-\nu_{12}\nu_{21}} = \frac{\nu_{21}E_1}{1-\nu_{12}\nu_{21}}; \quad Q_{66} = G_{12} \tag{3.30}$$

These material properties are of course those of the composite or the insulation, depending on which layer is being analyzed. In these equations, the material properties are defined above except for v_{21} which is given by

$$\nu_{21} = \frac{\nu_{12}E_2}{E_1} \tag{3.31}$$

For this analysis, the stress and strain in the layers of the laminate are individually calculated. However, in order to proceed, the laminate has to be defined as shown in Figure 3.7.

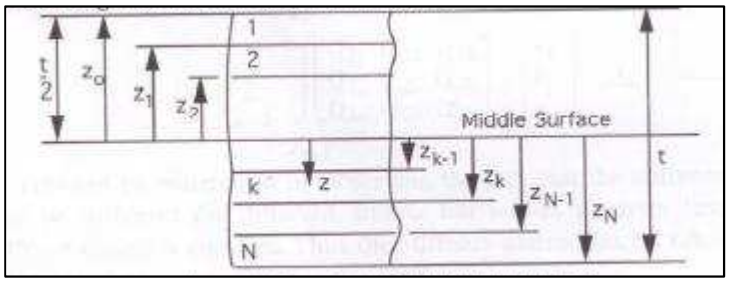


Figure 3.7 Geometry of an N-Layered Laminate [19].

As can be seen in this figure, the midline of the laminate is set as the *Z*-coordinate and the k^{th} lamina layer(s) extends from the middle surface. In addition to the coordinate system defined in Figure 3.7, the orientation of the individual lamina in the laminate must be accounted for in the stiffness matrix. This angle offset from the principal directions is shown in Figure 3.8. An example of a laminate with several lamina of different angle orientations is shown in Figure 3.9 below. This illustrates how a laminate can be arranged using the notation in Figure 3.7. The laminate on the left has what is known as $[\pm 45/0]_S$ orientation where it is arranged symmetrically about the midline, while the right laminate orientation is written as $[\pm 45/0]_T$. The response of the laminate under a load depends on how it is oriented, and it can be reasonably shown that the response of these two arrangements will differ even though both are composed of the same layers.

If the lamina is oriented such that the angle is 0° relative to the coordinate system, then the reduced stiffness matrix shown above may be used. However, when there is an angle offset a modified matrix, known as the Q' matrix, must be used in the equations.

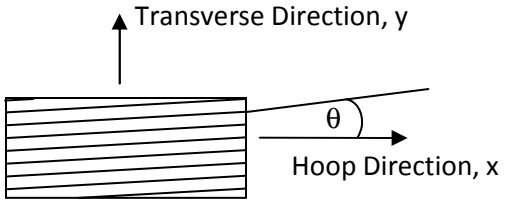


Figure 3.8 Lamina Geometry.

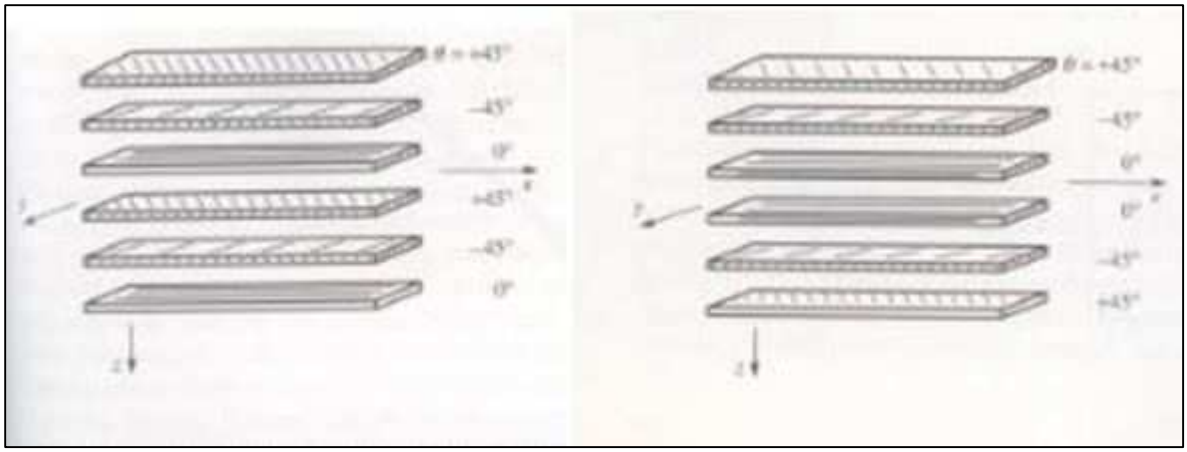


Figure 3.9 Laminate Orientation for 0° and 45° Samples [19].

This matrix is represented as

$$\begin{Bmatrix}\sigma_x\\ \sigma_y\\ \tau_{xy}\end{Bmatrix}=\begin{bmatrix}Q'_{11} & Q'_{12} & Q'_{16}\\ Q'_{12} & Q'_{22} & Q'_{26}\\ Q'_{16} & Q'_{26} & Q'_{66}\end{bmatrix}\begin{Bmatrix}\varepsilon_x\\ \varepsilon_y\\ \gamma_{xy}\end{Bmatrix} \tag{3.32}$$

In this equation the Q'_{xx}'s are found using the equations below, where as before θ is the angle offset [3]

$$\begin{aligned}
Q'_{11} &= Q_{11}\cos^4\vartheta+Q_{22}\sin^4\vartheta+2(Q_{12}+2Q_{66})\sin^2\vartheta\cos^2\vartheta\\
Q'_{22} &= Q_{11}\sin^4\vartheta+Q_{22}\cos^4\vartheta+2(Q_{12}+2Q_{66})\sin^2\vartheta\cos^2\vartheta\\
Q'_{66} &= (Q_{11}+Q_{22}-2Q_{12}-2Q_{66})\sin^2\vartheta\cos^2\vartheta+Q_{66}(\sin^4\vartheta+\cos^4\vartheta)\\
Q'_{12} &= (Q_{11}+Q_{22}-4Q_{66})\sin^2\vartheta\cos^2\vartheta+Q_{12}(\sin^4\vartheta+\cos^4\vartheta)\\
Q'_{16} &= (Q_{11}-Q_{12}-2Q_{66})\sin\vartheta\cos^3\vartheta-(Q_{22}-Q_{12}-2Q_{66})(\sin^3\vartheta+\cos\vartheta)\\
Q'_{26} &= (Q_{11}-Q_{12}-2Q_{66})\sin^3\vartheta\cos\vartheta-(Q_{22}-Q_{12}-2Q_{66})(\sin\vartheta+\cos^3\vartheta)
\end{aligned} \tag{3.33}$$

Once the Q' matrix was found for each layer, it was used in conjunction with the thickness from the midpoint of the laminate z_k to find some important properties of the material. The *extensional stiffness matrix* [A] relates the resultant forces to midplane strains, the *bending stiffness matrix* [D] relates the resultant moments to plate curvature, and the *coupling matrix* [B] implies coupling between bending and extension of a laminate plate. These are shown below.

$$[A] = A_{ij} = \sum_{k=1}^{N} (Q'_{ij})_k (z_k - z_{k-1}) \tag{3.34}$$

$$[B] = B_{ij} = \frac{1}{2}\sum_{k=1}^{N} (Q'_{ij})_k (z_k^2 - z_{k-1}^2) \tag{3.35}$$

$$[D] = D_{ij} = \frac{1}{3}\sum_{k=1}^{N} (Q'_{ij})_k (z_k^3 - z_{k-1}^3) \tag{3.36}$$

The loading on the laminate can be broken into two types: forces and moments. For this particular analysis, the loadings only consist of forces (a pressure loading); therefore, thin-walled pressure vessel theory is applied to find the force matrix and moment matrix

$$[N] = \begin{Bmatrix} N_x \\ N_y \\ N_{xy} \end{Bmatrix} = \begin{Bmatrix} pr \\ \frac{pr}{2} \\ 0 \end{Bmatrix}; \qquad [M] = \begin{Bmatrix} M_x \\ M_y \\ M_{xy} \end{Bmatrix} = \begin{Bmatrix} 0 \\ 0 \\ 0 \end{Bmatrix} \tag{3.37}$$

where *p* is the internal pressure and *r* is the radius of the middle surface of the laminate. These quantities can be inserted into the total laminate constitutive equation [19] as

$$\begin{Bmatrix} [N] \\ [M] \end{Bmatrix} = \begin{bmatrix} [A] & [B] \\ [B] & [D] \end{bmatrix} \begin{Bmatrix} [\varepsilon^o] \\ [\kappa] \end{Bmatrix} \quad \text{or} \quad \begin{Bmatrix} [\varepsilon^o] \\ [\kappa^o] \end{Bmatrix} = \begin{bmatrix} [A] & [B] \\ [B] & [D] \end{bmatrix}^{-1} \begin{Bmatrix} [N] \\ [M] \end{Bmatrix} \tag{3.38}$$

where $[\varepsilon^o]$ are the middle surface strains and $[\kappa^o]$ are the middle surface curvatures defined as

$$\begin{Bmatrix} \varepsilon_x^o \\ \varepsilon_y^o \\ \gamma_{xy}^o \end{Bmatrix} = \begin{Bmatrix} \frac{\partial u^o}{\partial x} \\ \frac{\partial v^o}{\partial y} \\ \frac{\partial u^o}{\partial y} + \frac{\partial v^o}{\partial x} \end{Bmatrix} \quad \text{and} \quad \begin{Bmatrix} \kappa_x^o \\ \kappa_y^o \\ \kappa_{xy}^o \end{Bmatrix} = -\begin{Bmatrix} \frac{\partial^2 w^o}{\partial x^2} \\ \frac{\partial^2 w^o}{\partial y^2} \\ 2\frac{\partial^2 w^o}{\partial x \partial y} \end{Bmatrix} \tag{3.39}$$

Now the Kirchhoff's hypothesis is utilized along with these middle surface strains and curvatures.

Kirchhoff hypothesis equations are [19]

$$\varepsilon_x(x, y, z) = \varepsilon_x^o(x, y) + z\kappa_x^o(x, y) \tag{3.40}$$

$$\varepsilon_y(x,y,z) = \varepsilon_y^o(x,y) + z\kappa_y^o(x,y) \tag{3.41}$$

$$\gamma_{xy}(x,y,z) = \gamma_{xy}^o(x,y) + z\kappa_{xy}^o(x,y) \tag{3.42}$$

Knowing these midplane strains and curvatures, the stress in the k^{th} lamina of the laminate can be obtained by substituting into the Kirchhoff hypothesis equation [19]

$$\begin{Bmatrix}\sigma_x\\ \sigma_y\\ \tau_{xy}\end{Bmatrix}_k = \begin{bmatrix}Q'_{11} & Q'_{12} & Q'_{16}\\ Q'_{12} & Q'_{22} & Q'_{26}\\ Q'_{16} & Q'_{26} & Q'_{66}\end{bmatrix}_k \begin{Bmatrix}\varepsilon_x^o\\ \varepsilon_y^o\\ \gamma_{xy}^o\end{Bmatrix} + z\begin{bmatrix}Q'_{11} & Q'_{12} & Q'_{16}\\ Q'_{12} & Q'_{22} & Q'_{26}\\ Q'_{16} & Q'_{26} & Q'_{66}\end{bmatrix}_k \begin{Bmatrix}\kappa_x^o\\ \kappa_y^o\\ \kappa_{xy}^o\end{Bmatrix} \tag{3.43}$$

The stress in each layer is linear with *z;* since each layer may have a different stiffness matrix, stresses will be discontinuous at the boundary between laminae.

3.3.3 Inclusion of Thermal Loading in Laminate Analysis

The principle of superposition can be used to include thermal loading in the stress analysis of the laminated coil. Equations for the off-axis thermal behavior were developed earlier and are represented in equations (3.26) through (3.28). Utilizing these expressions for α_x, α_y, and α_{xy}, one can find the laminate behavior at any offset angle ϑ.

Once the directional thermal expansion coefficients are found, then they can be superimposed directly into the strain matrix such that final stress-strain relation for mechanical and thermal loadings on the coil can be represented as [19]

$$\begin{Bmatrix}\sigma_x\\ \sigma_y\\ \tau_{xy}\end{Bmatrix}_k = \begin{bmatrix}Q'_{11} & Q'_{12} & Q'_{16}\\ Q'_{12} & Q'_{22} & Q'_{26}\\ Q'_{16} & Q'_{26} & Q'_{66}\end{bmatrix}_k \begin{Bmatrix}\varepsilon_x^o\\ \varepsilon_y^o\\ \gamma_{xy}^o\end{Bmatrix} + z\begin{bmatrix}Q'_{11} & Q'_{12} & Q'_{16}\\ Q'_{12} & Q'_{22} & Q'_{26}\\ Q'_{16} & Q'_{26} & Q'_{66}\end{bmatrix}_k \begin{Bmatrix}\kappa_x^o\\ \kappa_y^o\\ \kappa_{xy}^o\end{Bmatrix} - \Delta T\begin{bmatrix}Q'_{11} & Q'_{12} & Q'_{16}\\ Q'_{12} & Q'_{22} & Q'_{26}\\ Q'_{16} & Q'_{26} & Q'_{66}\end{bmatrix}_k \begin{Bmatrix}\alpha_x\\ \alpha_y\\ \alpha_{xy}\end{Bmatrix} \tag{3.44}$$

Or, more concisely

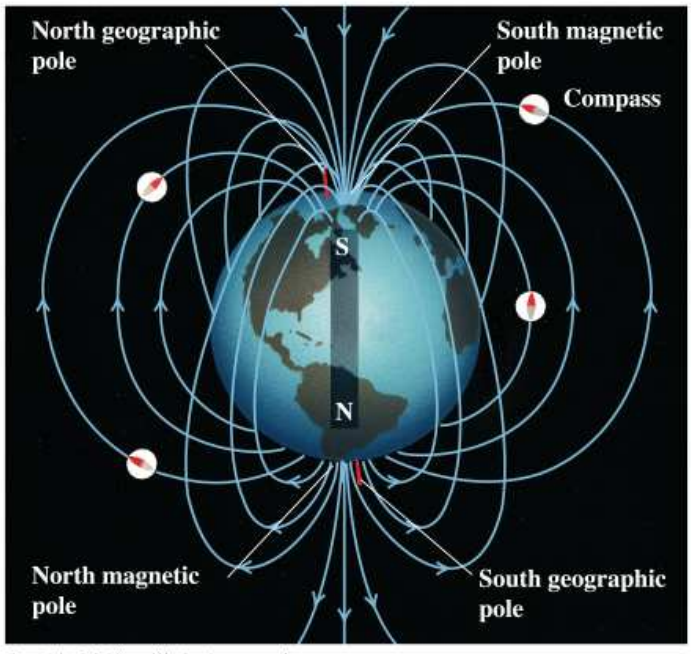
$$\begin{Bmatrix} \sigma_x \\ \sigma_y \\ \tau_{xy} \end{Bmatrix}_k = \begin{bmatrix} Q'_{11} & Q'_{12} & Q'_{16} \\ Q'_{12} & Q'_{22} & Q'_{26} \\ Q'_{16} & Q'_{26} & Q'_{66} \end{bmatrix}_k \begin{Bmatrix} \varepsilon_x^o + z\kappa_x^o - \Delta T\alpha_x \\ \varepsilon_y^o + z\kappa_y^o - \Delta T\alpha_y \\ \gamma_{xy}^o + z\kappa_{xy}^o - \Delta T\alpha_{xy} \end{Bmatrix} \quad (3.45)$$

3.4 Magnetic Stress in a Cylinder

A *magnetic field* is produced when a charged particle is moving causing *current* to flow; this field occupies the surrounding space and is a separate entity from the *electric field*. If any other charge or current is present within this magnetic field, a force is exerted on this charge or current by the field [23]. Magnetism is present in many applications, including the earth's magnetic field, as shown in Figure 3.10.

When current runs through a straight wire, it will create a magnetic field that can interact with any charged particle within this field. For a finite length segment of wire, Tipler [25] suggests that the magnetic field B can be found using the following equation

$$B = \frac{\mu_0 I}{4\pi R}(sin\varphi_1 + sin\varphi_2) \quad (3.46)$$



Copyright © Addison Wesley Longman, Inc.

Figure 3.10 Earth's Magnetic Field [24].

In this equation, μ_0 is the *permeability of free space*, with the value $\mu_0 = 4\pi \times 10^{-7} T \cdot m/A = 4\pi \times 10^{-7} N/A^2$, *I* is the current in the wire, *R* is the perpendicular distance to the particle, and φ_1 and φ_2 are angles between the line perpendicular to the wire and the line from the point P to either end of the wire. This is illustrated in Figure 3.11 below.

If the wire is very long, then the angles become very nearly 90° so the equation becomes

$$B = \frac{\mu_0 I}{2\pi r} \tag{3.47}$$

Force due to a magnetic field created by current running in a wire is found using the basic force equation [25]

$$\vec{F} = I\vec{l} \times \vec{B} \tag{3.48}$$

For two parallel conductors carrying currents *I* and *I'*, this becomes [23]

$$F = I'LB = \frac{\mu_0 I I' L}{2\pi r} \tag{3.49}$$

This is shown in Figure 3.12 below.

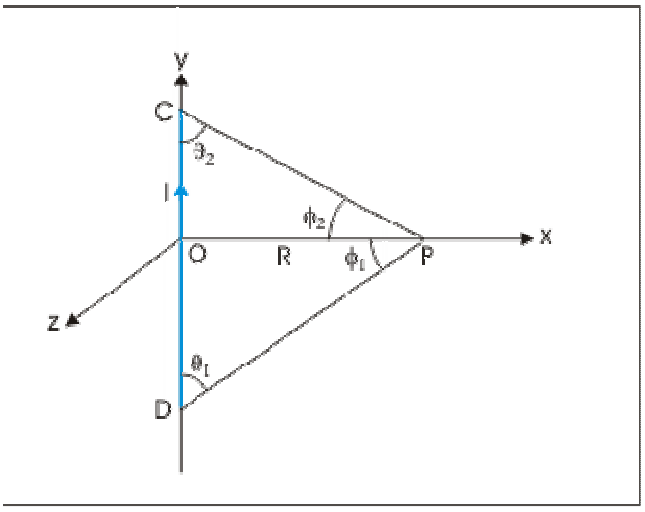


Figure 3.11 Geometry for Calculating Magnetic Field at *P* Due to Current *I* [26].

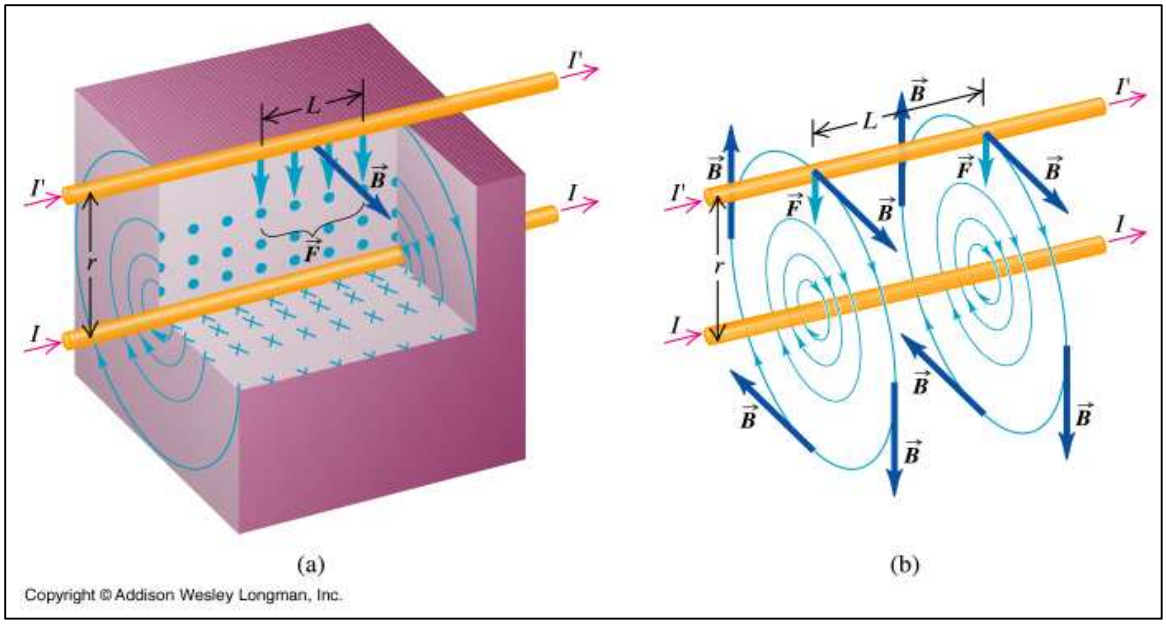


Figure 3.12 Force Due to a Current Running Through Two Parallel Wires [24].

A current-carrying wound helical coil falls into a special type of conductor called a *solenoid*. In the case of this project, the composite cylinder would be considered a solenoid. Due to the axisymmetric, wound shape of a solenoid, it has an interesting magnetic field. Figure 3.13 shows a current-carrying solenoid and a typical resulting magnetic field. The magnetic field produced by a solenoid is uniform except at the ends where it tapers off and loops back inside the coil [27]. However, the forces and by extension the mechanical stresses in a solenoid are not nearly as uniform.

The mechanical stress in a solenoid occurs because of two opposite effects: interaction between adjacent turns, and interaction of turns opposite each other. Adjacent turns in a solenoid carry parallel current traveling in the same direction; therefore they have a force of attraction between them that causes a compressive stress along the axis of the coil. Conversely, opposite sides of the coil have current traveling in opposite directions and as such they have a repulsive force that creates tensile stress in the conductors [23].

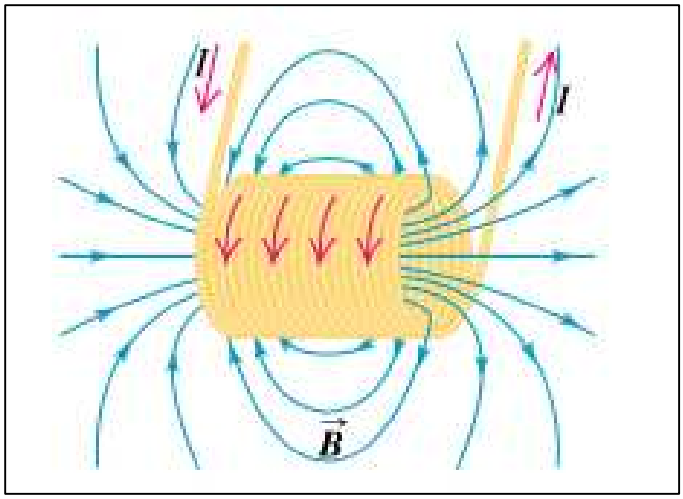


Figure 3.13 Magnetic Field of a Current-Carrying Solenoid [24].

The force in the solenoid is proportional to the magnetic field and is given by an equation known as the *Lorentz force equation*. The Lorentz force equation is [28]

$$\frac{F}{q} = E + v \times B \tag{3.50}$$

Where *F* is the force, *q* is the charge, *E* is electric field intensity, *v* is the velocity of the geometry, and *B* is the magnetic flux density. The stress experienced in a solenoid due to these forces can be found using *Maxwell's stress tensor*. Maxwell's stress tensor is complicated for geometries like that of a current-carrying wound coil, hence finite element methods are popularly employed for such problems. Maxwell's stress tensor is given by the following equation [29]

$$\sigma_{ij} = \varepsilon_0 E_i E_j + \frac{1}{\mu_0} B_i B_j - \frac{1}{2}(\varepsilon_0 E^2 + \frac{1}{\mu_0} B^2)\delta_{ij} \tag{3.51}$$

In this equation ε_0 is the *permittivity of vacuum* given as $4\pi \times 10^{-7}$ *H/m* and δ_{ij} is *Kronecker's delta*. As stated before, it is a daunting task to find this stress for geometry such as a multi-layer conducting solenoid coil but this difficulty can be overcome by employing the powerful FEA software.

Chapter IV

METHODOLOGY

4.1 Overview

This phase of the research focuses on the effect of variation in fiber volume fraction on stresses and strains in a copper/cyanate ester cylindrical coil used for nuclear plasma containment. The first step was to develop mathematical models to try to accurately predict the effect of varying the fiber volume fraction of the composite used in the coil. This portion of the research was further broken down into the lamina level analysis and the laminate level analysis. The mathematical models developed were then compared to experimental results found from actual samples tested by Composite Technology Development, Inc. Additionally, finite element models were created to perform magnetic load analysis and to further verify the results of the mathematical model.

4.2 Modeling

The coil is modeled as a compacted conductor composed of unidirectional copper/cyanate ester composite. Figure 4.1 shows a graphic of the coil. When wound in a coil like that in Figure 4.1, the wires will not be parallel to the hoop direction but rather will be oriented at an angle ϑ from it. This is shown in Figure 4.2 below. This compacted composite conductor is called the orthotropic lamina at the lamina level. The composite conductor will be composed of copper wires with cyanate ester matrix filling the voids in the material, and lapped S2 glass insulation on the outside of the copper sleeve, as shown in Figure 4.3. When several of these laminas are stacked together with an insulation layer separating them, this creates what is known as the laminate. This is the terminology used below to distinguish between these levels of analysis.

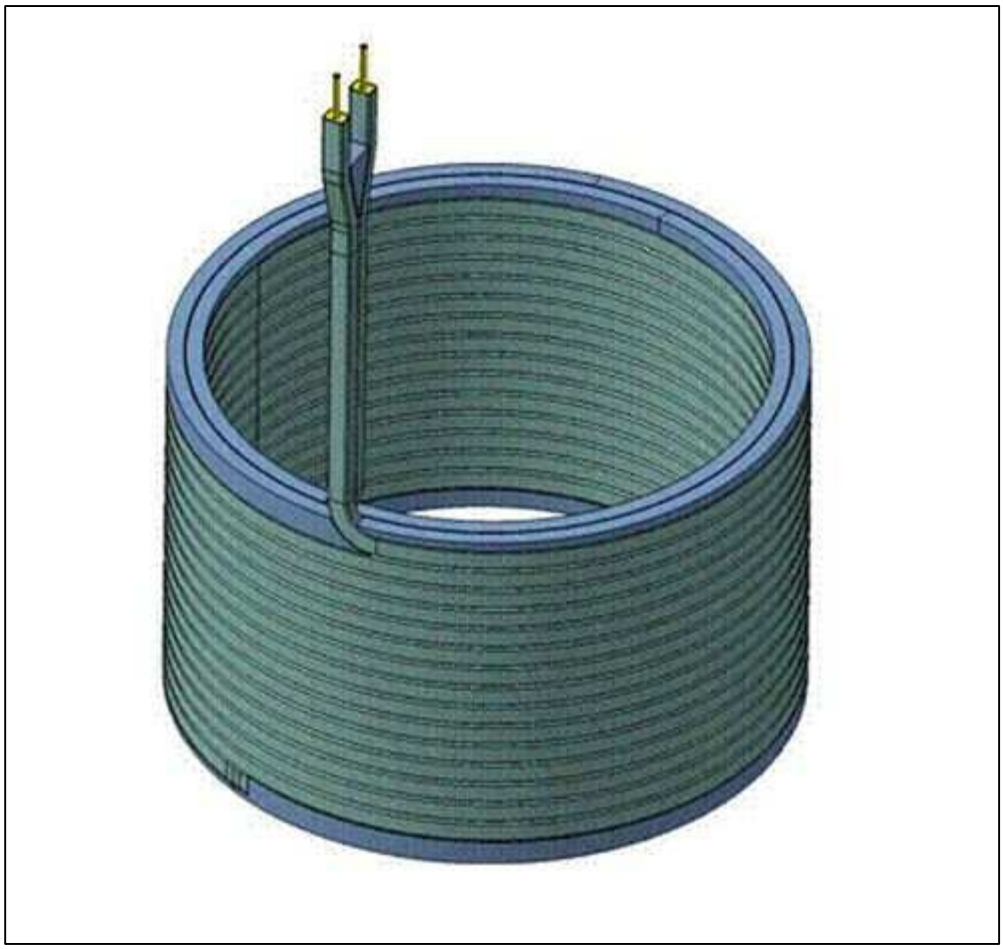


Figure 4.1 Copper Conductor Wound in Cylindrical Form.

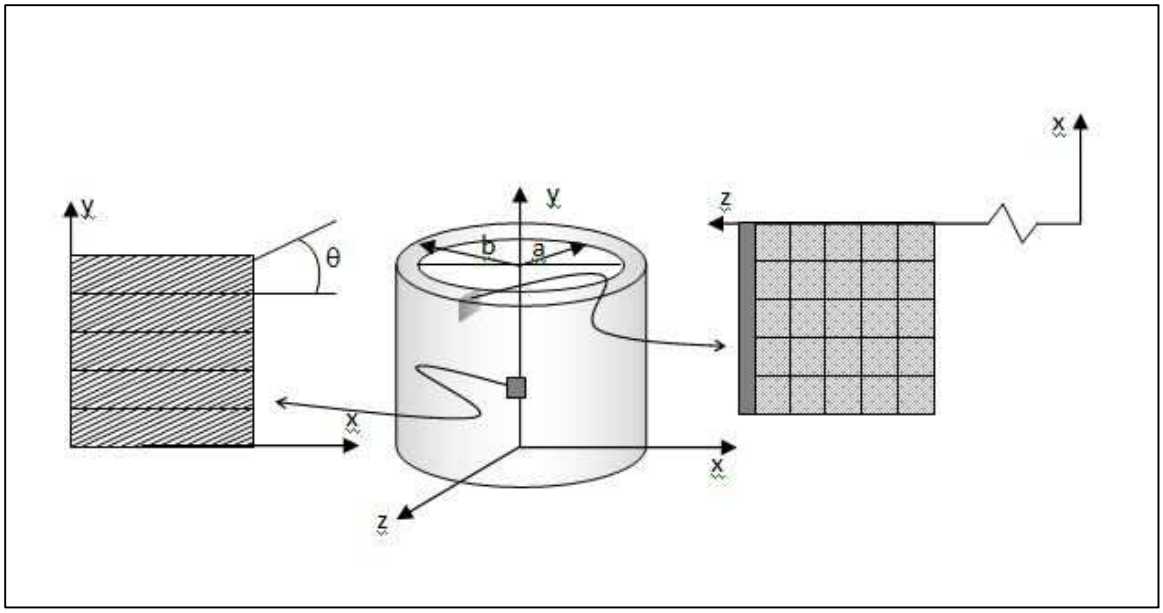
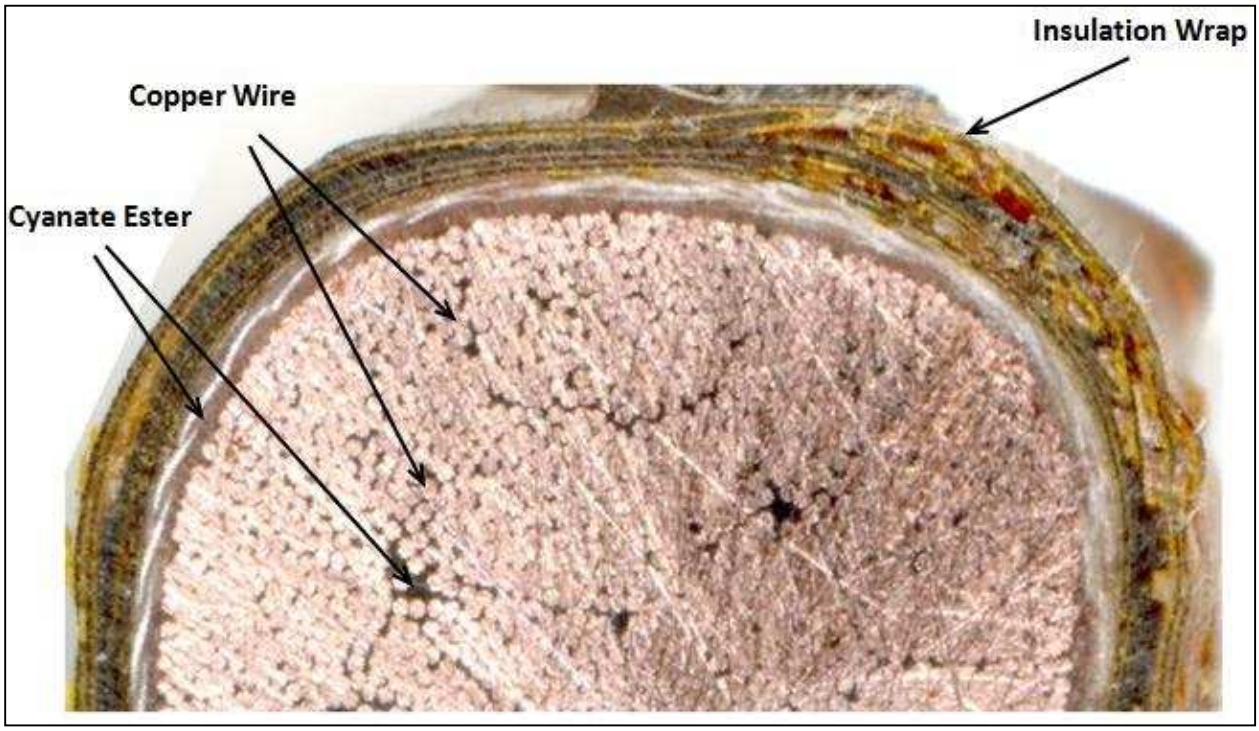


Figure 4.2 Schematic Showing Fiber Orientation.



4.3 Layout of Composite Wires. Cyanate ester is used to insulate and support the copper wires as well as fill voids between these wires.

4.2.1 Lamina Level Analysis

Lamina level analysis and laminate level analysis were based on laminate plate theory. In both the lamina and laminate level analysis, several symbols were used to abbreviate the material properties of interest, a comprehensive list of which is shown in the List of Symbols on page xv. In the lamina level portion, the composite was considered to consist of two portions, the cyanate ester polymer matrix, and the copper wires embedded in this. Each composite lamina was considered to be orthotropic. The material properties of the wires and the matrix were considerably different. The stiffness values E_1, E_2, v_{12}, and G_{12} were found from micromechanics using the material properties E_f, E_m, v_f, v_m, G_f, and G_m. All of these equations are a function of the fiber volume fraction of the material, V_f, and the matrix volume fraction V_m, assumed for this composite to be $V_m = 1\text{-}V_f$ since the composite has very few voids as discussed previously. Then the overall material constants E_x, E_y, G_{xy}, and v_{xy} were found based on E_1, E_2, v_{12}, and G_{12} and as a function of the fiber orientation angle ϑ from the reference X-axis. In order to perform the laminate level analysis, thermal expansion coefficients of the lamina were needed, and these were included in the lamina level analysis. These were calculated based on the thermal expansion coefficients of the constituents, copper fiber and polymer matrix.

4.2.2 Laminate Level Analysis

The laminate level analysis was then applied to calculate stress distribution across the thickness of various laminae. For this we considered the geometry of a composite cylinder with multiple layers of composite material, insulated from each other with a thin layer of glass cloth/cyanate ester orthotropic composite. A MATLAB code was developed to predict the stress distribution across the laminate thickness under various loading conditions. Both mechanical and thermal loadings were considered for the composite cylinder at the laminate level. The mechanical loading consisted of an internal pressure applied uniformly to the inside surface of the composite. Although an internal pressure loading inside

the composite cylinder is not of interest for the magnet applications, the MATLAB code included internal pressure primarily for code verification against known results. The thermal loading consisted of a uniform temperature through the material. The normal and shear stresses and strains in each composite layer and in the insulation layers were determined.

4.3 MATLAB Programming Environment

The code for the model was developed using the MATLAB programming environment. The code consisted of two distinct analysis types: the lamina analysis and the laminate analysis. The lamina level analysis of a copper/cyanate ester composite studied how varying the fiber volume fraction affected the material properties of the composite, namely the elastic moduli, the shear modulus, and Poisson's ratio. For this portion of the research, laminate plate theory (LPT) was utilized in conjunction with micromechanics of the lamina [22]. The equations developed and presented in Section 3 are utilized here. The code developed is included in the Appendix.

4.3.1 Lamina Level Programming

Initially, the fiber volume fractions desired, as well as the properties of the matrix and wires in the composite, are input into the MATLAB code. The necessary quantities are the V_f's, E_f, E_m, G_f, G_m, v_f, and v_m. From these inputs the stiffness coefficients E_1, E_2, G_{12}, and v_{12} can be found using the strength-of-materials approach [19]. The equations used are Equations (3.2), (3.3), (3.6), and (3.7). Once the micromechanics is used and these values are found, their off-axis behavior is characterized by finding E_x, E_y, G_{xy}, v_{xy}, and v_{xy} in equations (3.12) through (3.16). Next the thermal analysis was performed, using the coefficient of thermal expansions equations developed in (3.21), (3.23), and (3.26) through (3.28). These values are represented as α_1, α_2, α_x, α_y, and α_{xy}. This was the order in which the equations were used, and as mentioned previously the MATLAB code developed is shown in the Appendix.

4.3.2 Laminate Level Programming

The laminate level model uses the results from the lamina level analysis to predict how a laminate composed of multiple laminae will perform under a load. Additionally, these laminae will be oriented at different angles relative to a reference axis. The purpose of the MATLAB programming is to construct the code to see how a particular laminate will perform using known input parameters, and then it can be varied to account for virtually any laminate configuration. Since there were many different inputs required, it was easier to input all of the data as a table in Microsoft Excel and have MATLAB read it. Therefore, a particular configuration could be set up and then the code would be executed, and the initial parameters would already be updated. Table 4.1 shows an example configuration.

These inputs are self-explanatory. The number of layers includes the insulation layers, which in the above example are assumed to be glass cloth. The theory used in the code to develop the laminate level results is shown in equations (3.29) through (3.45). As can be inferred from the above table, the code was written to include a high level of flexibility, so that loading, number of layers, layer thicknesses, angular offsets, and coil dimensions can be varied. This allowed for great control over the input parameters and ultimately made it easier to explore how varying fiber volume fraction affected the output stresses.

Table 4.1 Input Parameters for Laminate Analysis in MATLAB.

Number of Layers	5		
Internal Pressure (kPa)	20		
Radius of Pressure Vessel (mm)	450		
Temperature Differential ΔT (^{o}C)	20		
Coefficient of Thermal Expansion α_1 (x10^{-6} K^{-1})	85		
Coefficient of Thermal Expansion α_2 (x10^{-6} K^{-1})	73		
CTE of Glass Cloth α_g (x10-6 K-1)	3		
Composite Compliance Matrix Q_c (GPa)	83.0425	14.4851	0
	14.4851	62.9786	0
	0	0	1.0624
Glass Cloth Compliance Matrix Q_g (GPa)	10	0.2	0
	0.2	10	0
	0	0	0.5

Thickness of Layers (mm)	**Angular offset of each layer (Degrees)**
3	0
0.5	0
4	10
0.5	0
3	20

4.4 Finite Element Analysis of Magnetic Loading

Finite element analysis was performed using the COMSOL commercially available software. Initially, the coil was modeled in three dimensions using the Autodesk Inventor Professional software and imported by COMSOL. The Inventor model of the coil is shown in Figure 4.4. However, it was found that when creating a model of magnetic loading and the resulting stresses, using the simplest geometry that still contains all the features necessary was the best approach since magnetic loading is more complicated than most other types of loads [28]. Since the coil was symmetric about the central axis, or the theta direction shown in Figure 3.4, it was easiest to create the preliminary model as a two-dimensional model utilizing axisymmetry about the midline of the coil. For the model itself, it was decided to use a coil consisting of two layers, with sixteen turns per layer. The drawing of the coil is shown in Figure 4.5. In this one can see that it consists of a coil in the center of the graphic, with two air layers around it. The inner layer is simply air, with the outer layer consisting of a region of "infinite" elements (an approximating feature used by COMSOL for modeling accuracy) so that the magnetic field isn't distorted by the boundary. In this and subsequent FEA figures, the inner red line is the axis of symmetry, so the drawing and the boundaries are rotated around it. Figure 4.6 shows the coil in detail. The turns consist of individual squares using the properties found in the mathematical model with a current run through it. As can be seen in the figure, the turns do not actually contact each other but rather have insulation layers of glass cloth between them.

4.4.1 Multiphysics Application Modes

COMSOL offers several Multiphysics Application Modes that are used to introduce the specific type of physical conditions and loadings on the model. For this simulation, the base multiphysics consists of a Structural Mechanics Module utilizing Stress-Strain relations and Axial Symmetry. This is coupled with the AC/DC Module of Azimuthal Induction Currents, Vector Potential for the magnetic loading, and a Heat Transfer Module of Resistive Heating for the thermal loading.

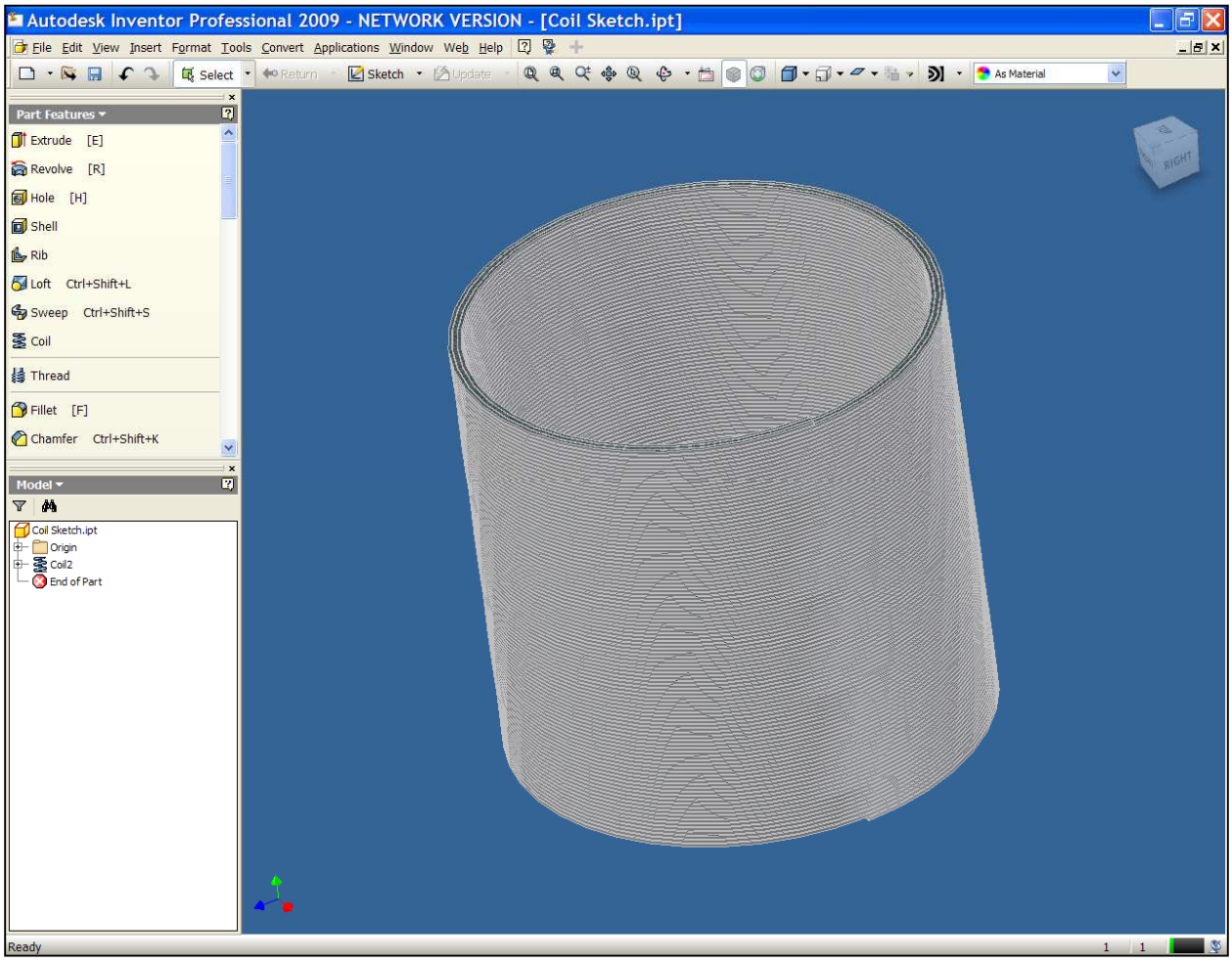


Figure 4.4 Autodesk Inventor Model of Coil. The coil consists of two composite layers with thin insulation layers on the outside and between the composite layers.

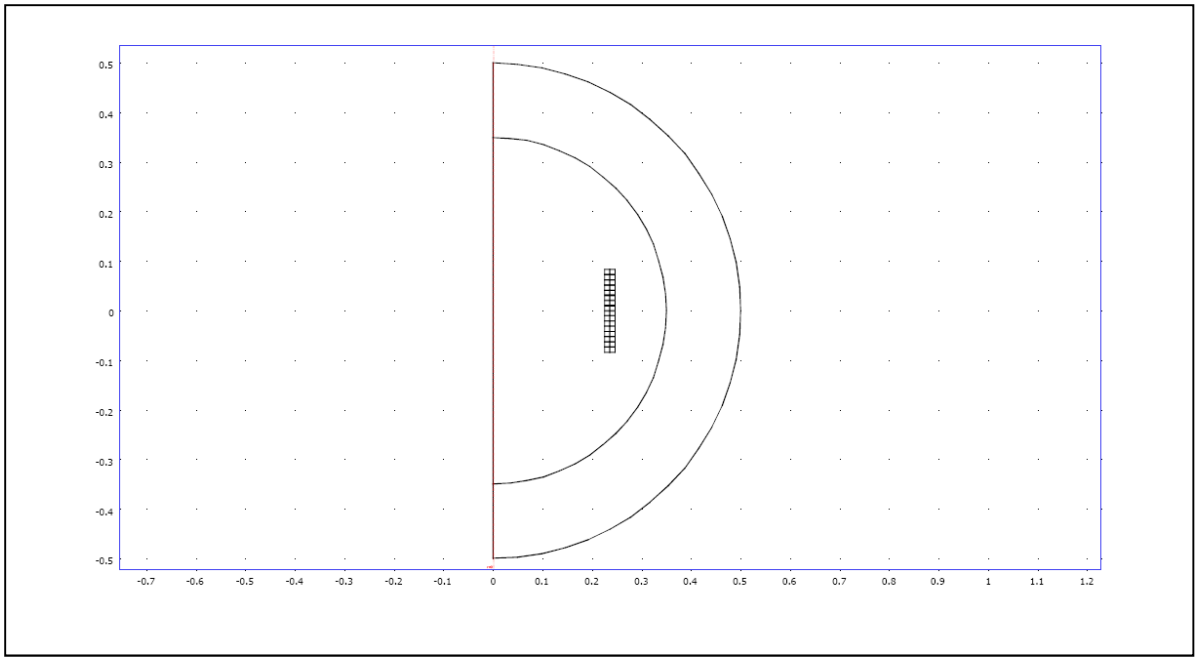


Figure 4.5 Drawing of COMSOL Magnetic Model.

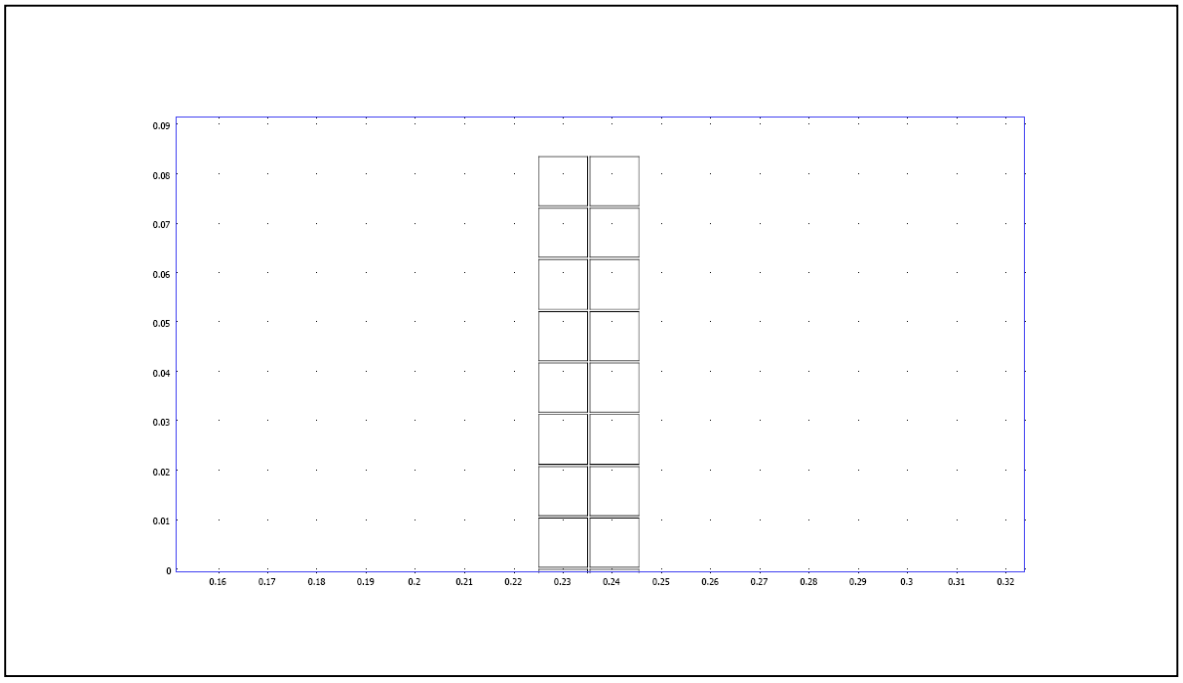


Figure 4.6 Close-up of the Coil.

4.4.2 Subdomain and Boundary Settings

Once the correct application modes are selected and inserted into the model, then the subdomain and boundary settings are required in order to couple the models together. This means that the magnetic loading and the thermal loading must be somehow related to the structural model so that stress and strain due to these loadings can be found. Figure 4.7 illustrates an example of how dialog boxes are used for subdomain and boundary editing.

4.4.3 Meshing and Mesh Settings

Once the correct operations, such as coupling loadings, inserting material properties, and grounding the structural model, were performed, the model could be meshed. Meshing is the term for breaking the model into discrete elements where the FEA calculations can be performed. The mesh of the model is shown in Figure 4.8 below. The mesh is automatically generated by the software once it is initialized, but can be refined and modified by the user for specific purposes. As can be seen below, the mesh is very fine within and near the coil conductor turns but is much courser farther away from the coil. This is a memory-saving feature of the software so that areas with a large gradient can be more precisely modeled while areas with less variation have broader mesh elements, thus preventing unnecessary calculations from being performed. A close-up view of the coil mesh is shown in Figure 4.9. This illustrates how corners and other typically higher-stress regions are finely meshed and how the other areas are not meshed nearly as finely. Once meshing is complete, the model is ready to be solved and the results analyzed.

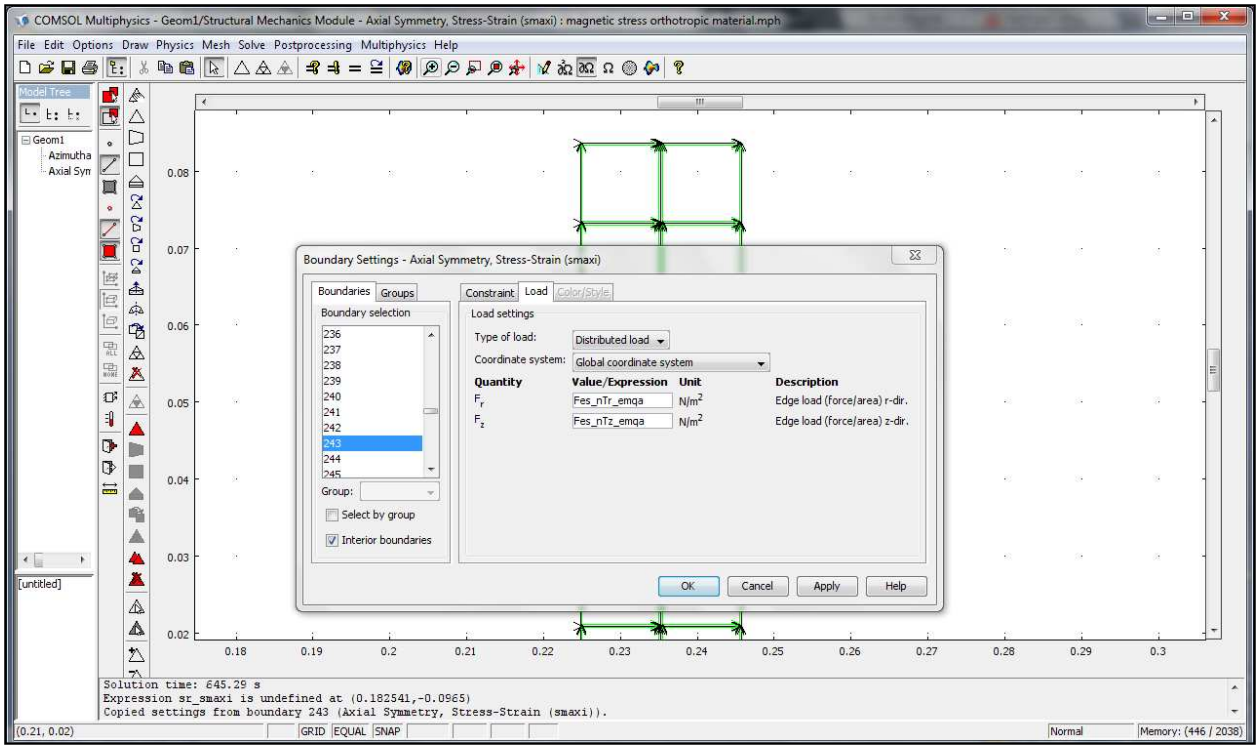


Figure 4.7 Editing Toolboxes Used in COMSOL. Domains, boundaries, and points can be individually selected and modified for different loads, constraints, material properties, etc.

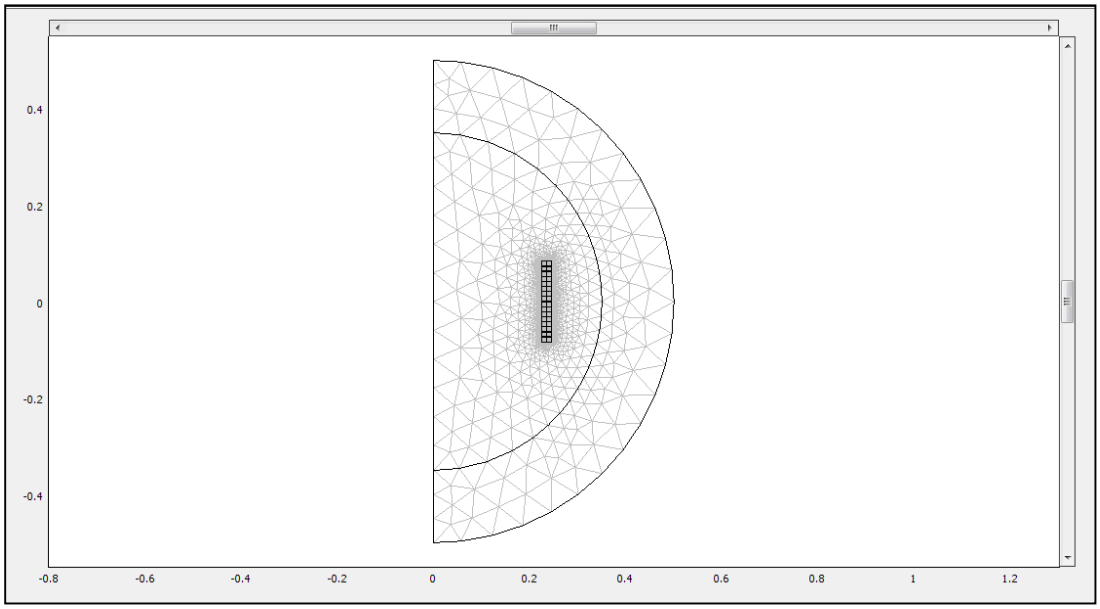


Figure 4.8 Mesh of Coil Geometry.

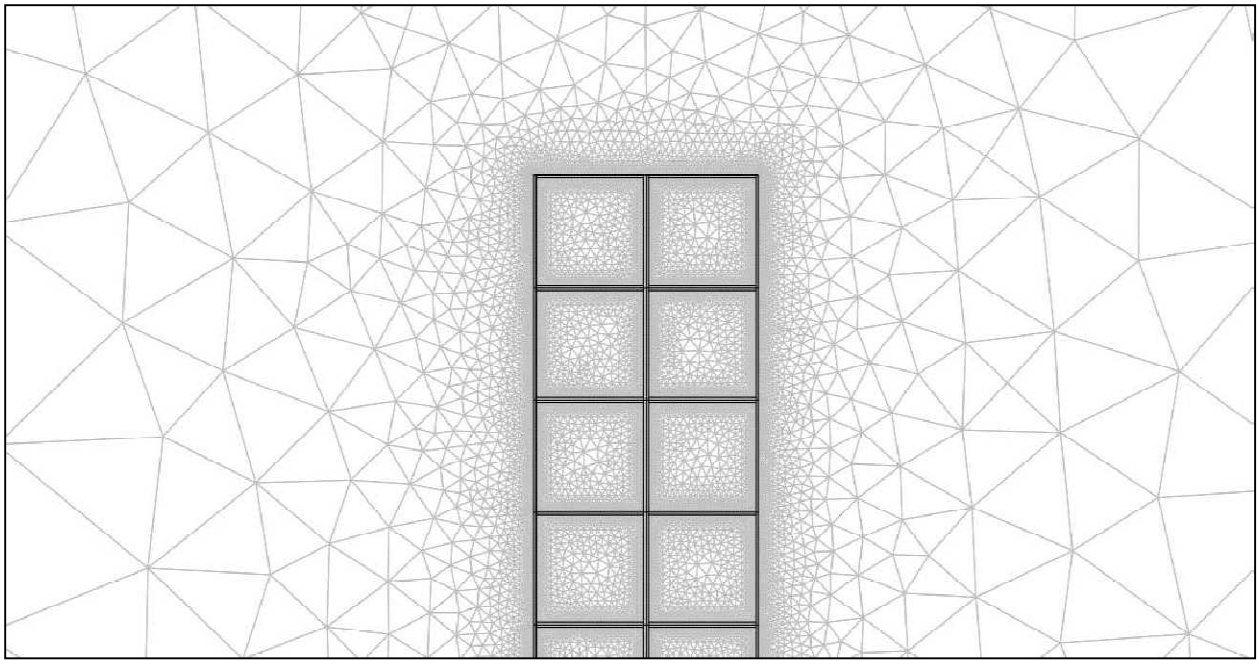


Figure 4.9 Close-Up View of Coil Mesh. The mesh is finest at critical points such as corners, different material contact surfaces, and in very thin insulation layers.

4.5 Finite Element Analysis of Magnetic Loading with Rounded Conductor

When analyzing the results of the magnetic loading analysis using square conductors, two issues were addressed:

1) Using square conductors that have corresponding sharp edges appear to have a stress concentration effect in that these edges magnify local stresses.
2) The actual conductors used, though they will ideally be square, in practice will have more rounded edges.

Figure 4.10 below shows a 2x2 conductor assembly that is used in practice. As can be seen in the image, the conductors have rounded edges.

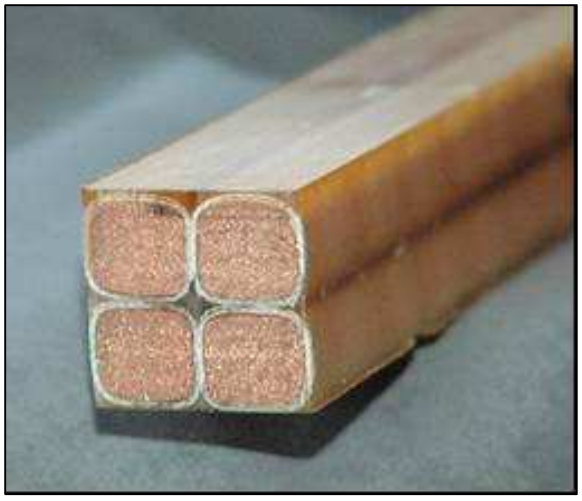


Figure 4.10 Photograph of a 2x2 Conductor Assembly [8]. Conductors are impregnated with and held together by CTD-403 resin.

For these reasons, it was decided to make a duplicate FEA model that is identical to the one developed previously except that the conductors and thus the corresponding insulation wrap layers are more rounded instead of square. The following is a brief development of the model. An exhaustive study as was performed on the model in Section 4.4 was not performed on this model; rather it was used to compare with the former model to see how rounding the edges affected stress and to try to determine whether eliminating the corners would reduce the stress concentration effect in the model.

The multiphysics for this model are exactly the same as those developed in the previous section. In order to test whether or not rounding the edges changed the stress, all other factors were held constant in the new model. Figure 4.11 shows the new FEA model developed, and Figure 4.12 is a close-up of this model.

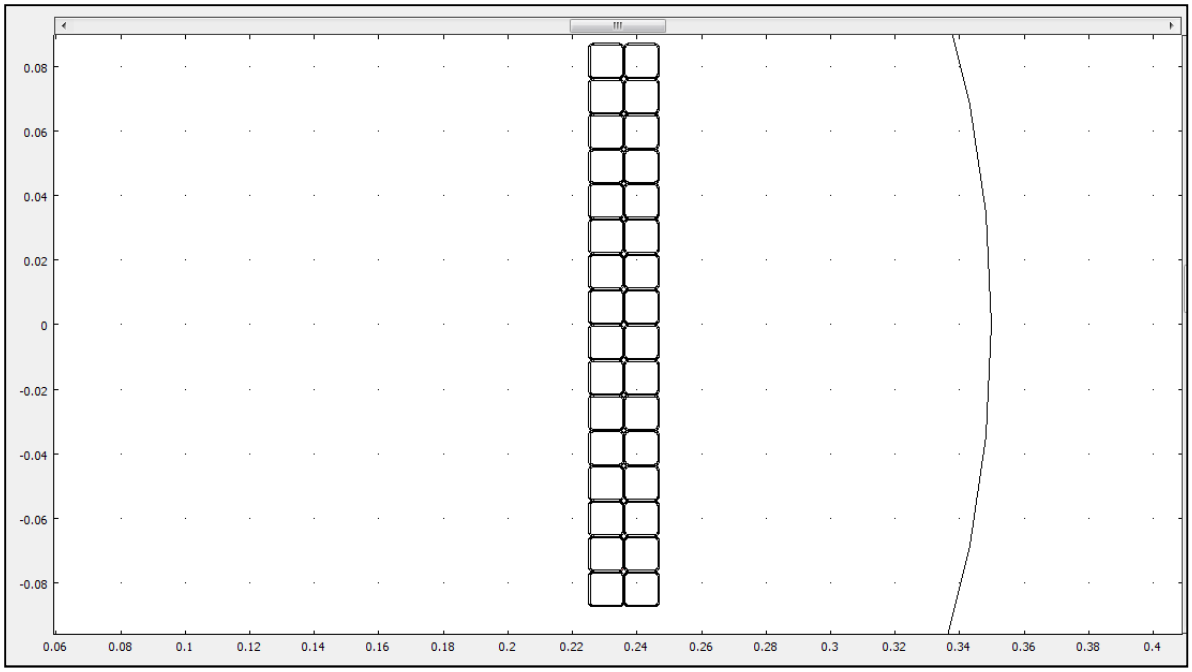


Figure 4.11 Magnetic Model with Rounded Edges.

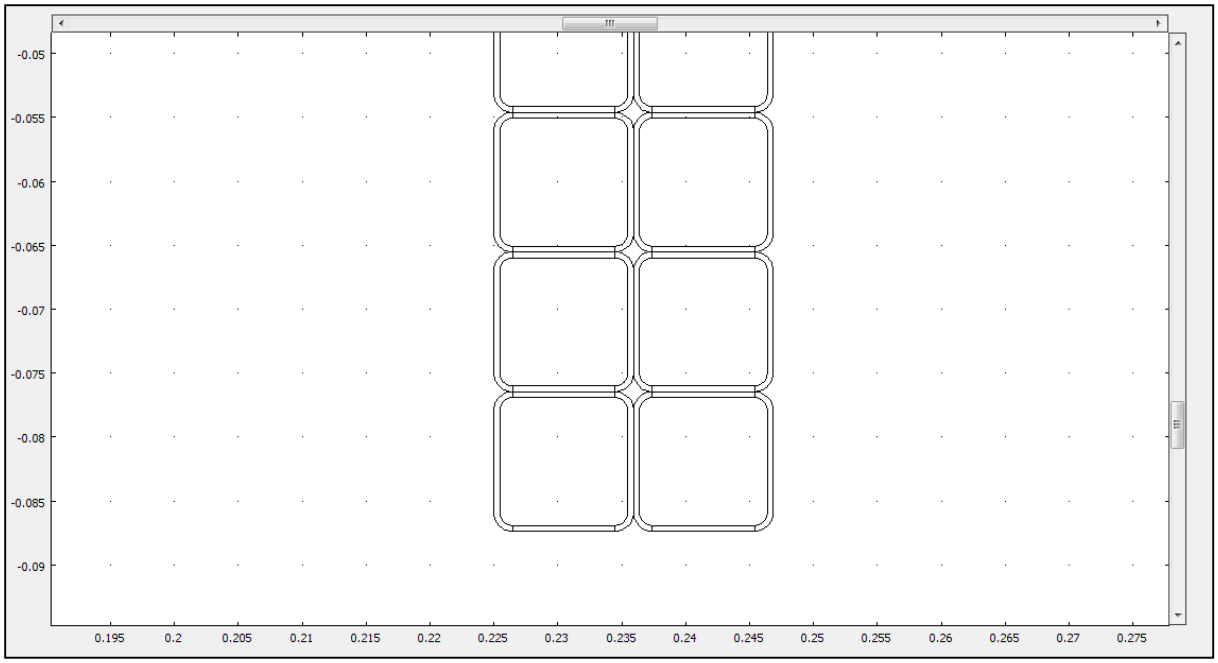


Figure 4.12 Close-Up of Rounded Edged Magnetic Model.

4.6 Finite Element Analysis of Thermal and Mechanical Loading

In order to verify the laminate level analysis of Section 4.2, a different FEA model was developed to predict stress from mechanical and thermal loading on the coil. This is a three-dimensional model and would more accurately portray the loads. This model looks very similar to the Inventor model shown in Figure 3.7, but for simplicity the layers are modeled as solid rather than with individual turns. The 3D model of the coil is shown in Figure 4.13. It is not obvious because of their small size, but the coil consists of two composite layers with insulation between these layers and on the outside of each layer. The coil is composed of one eighth of a completed coil and is sufficient to approximate the stresses experienced.

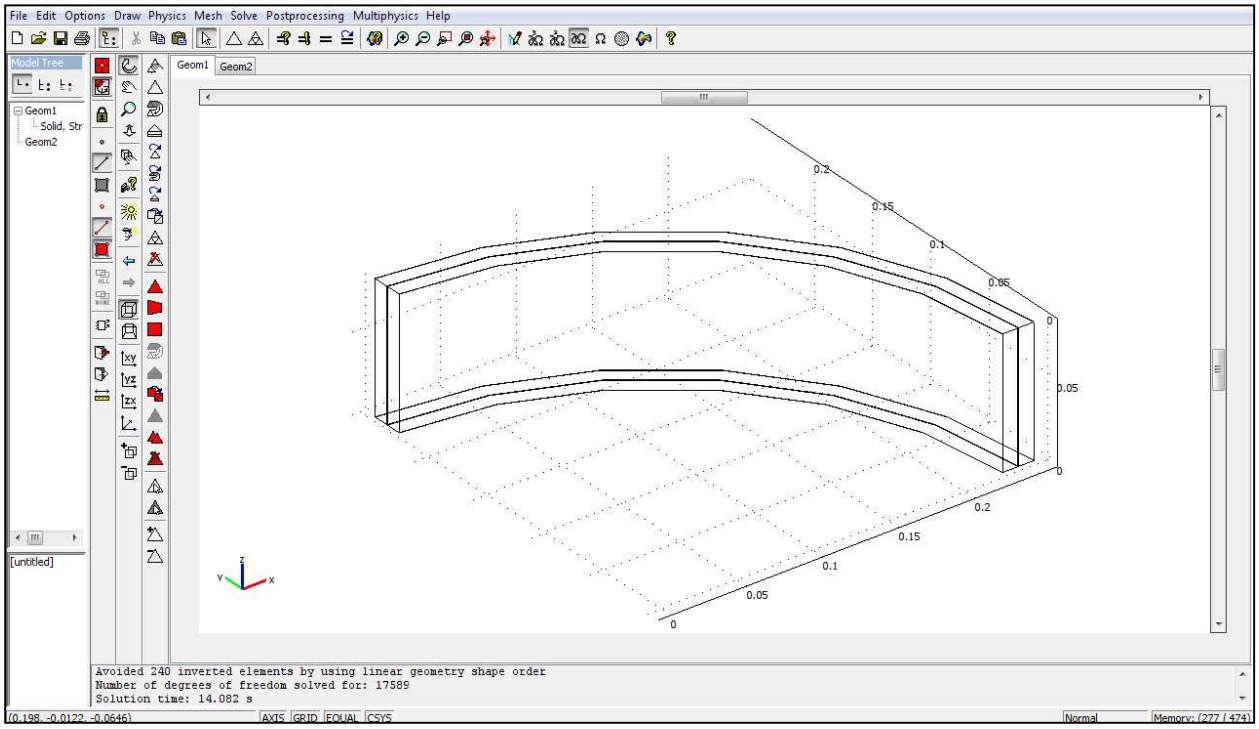


Figure 4.13 Drawing of COMSOL Thermal and Mechanical Model.

4.6.1 Multiphysics Application Modes

Unlike the magnetic model, this one was much simpler in that it did not involve coupling multiple multiphysics application modes together. The only application mode used was Solid, Stress-Strain from the structural mechanics module. This was used since the applied loads that are analyzed are mechanical and simply thermal. Since the thermal load is a simple uniform temperature difference, it can be inserted in the subdomain as a thermal expansion strain.

4.6.2 Subdomain and Boundary Settings

The subdomain settings tool box is used to input the material properties for both the composite and the insulation. It is also used to apply the thermal load to the model. The boundary settings tool box is used to identify the planes of symmetry (where the model should extend to complete the cylinder) and to apply the pressure load. Figure 4.14 shows the subdomain tool box.

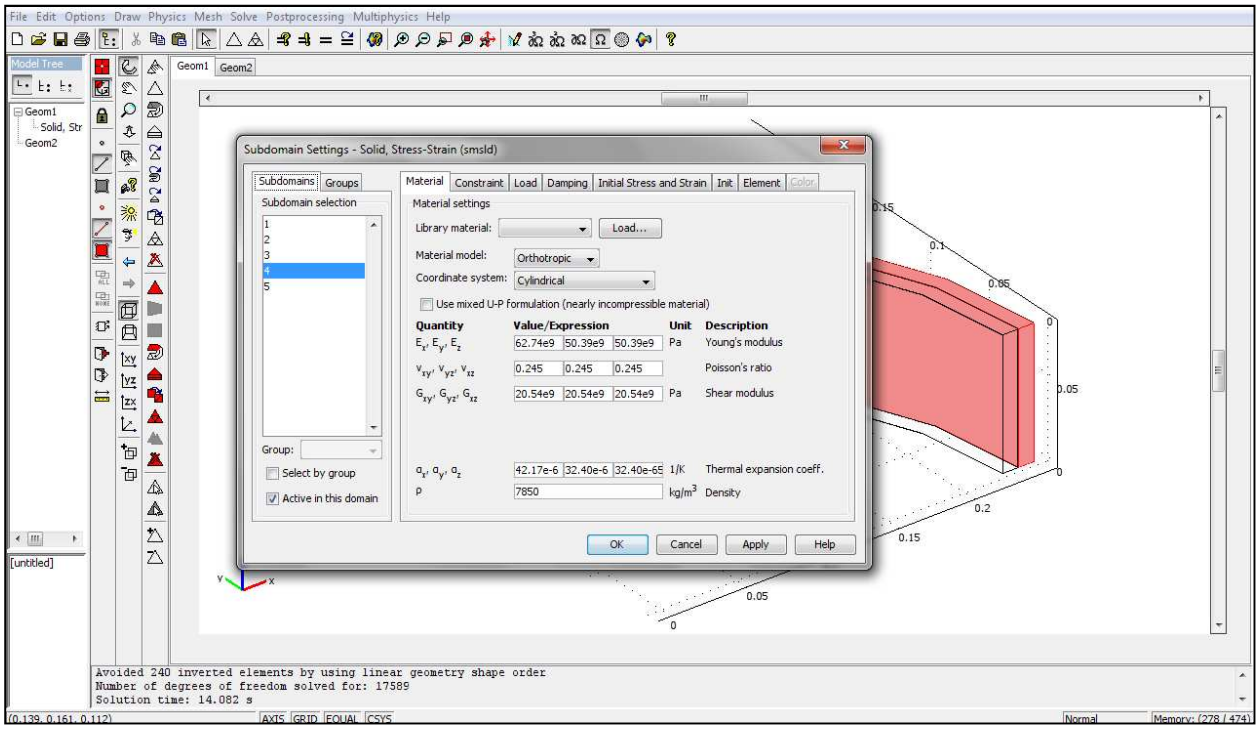


Figure 4.14 Subdomain Editing Toolbox for 3D Model. The toolboxes for 3D models are very similar to those used in 2D models previously.

4.6.3 Meshing and Mesh Settings

The mesh for a 3D model is created in a different way than it was for the 2D magnetic model. The vessel was drawn on a 2D plane, edge-on as shown in Figure 4.15. The curved sections were approximated by using the 2nd Degree Bézier Curve function built into COMSOL. Once this was drawn, the model was meshed using Mapped Mesh Parameters to create a structured 2D mesh. Then this was extruded into a 3D mesh with a set number of elements. Therefore the meshing of the model occurs before the subdomain and boundary settings are used, which is the reverse of the procedure for the 2D model. The completed meshed geometry is shown in Figure 4.16.

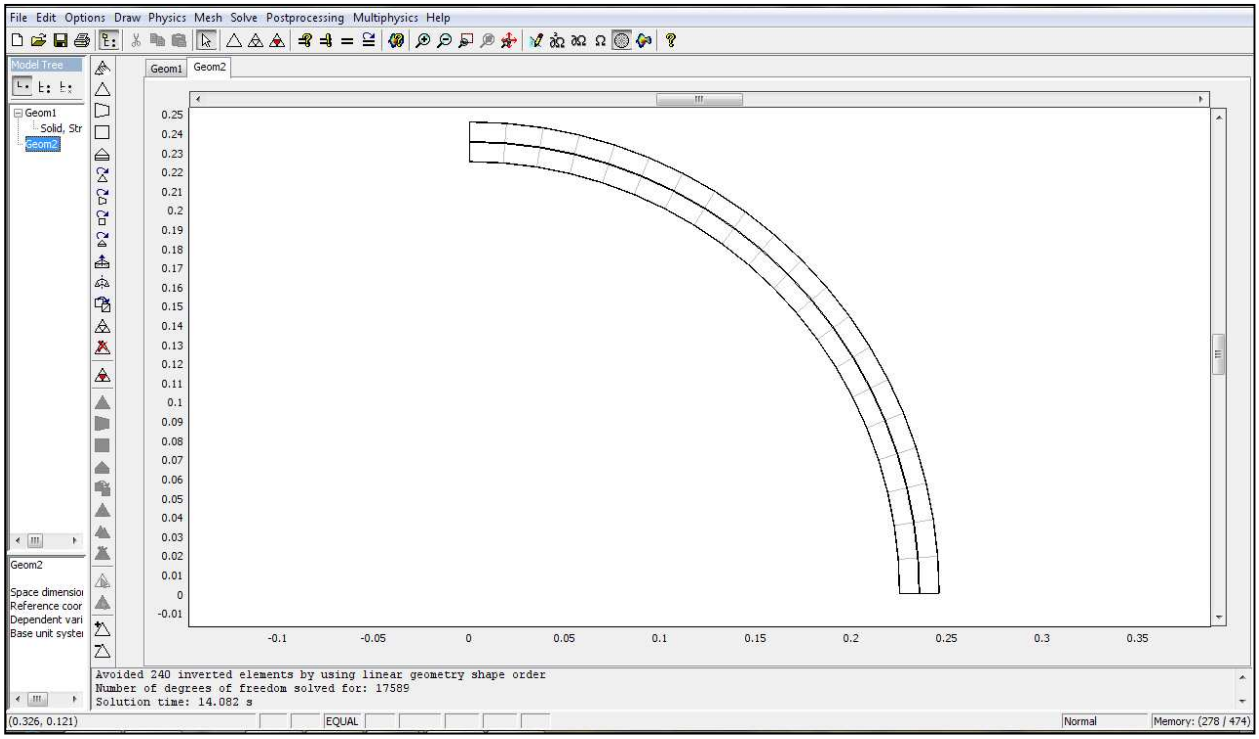


Figure 4.15 Initial Plane Sketch before Extrusion. The light gray squares represent the mesh elements to be extruded.

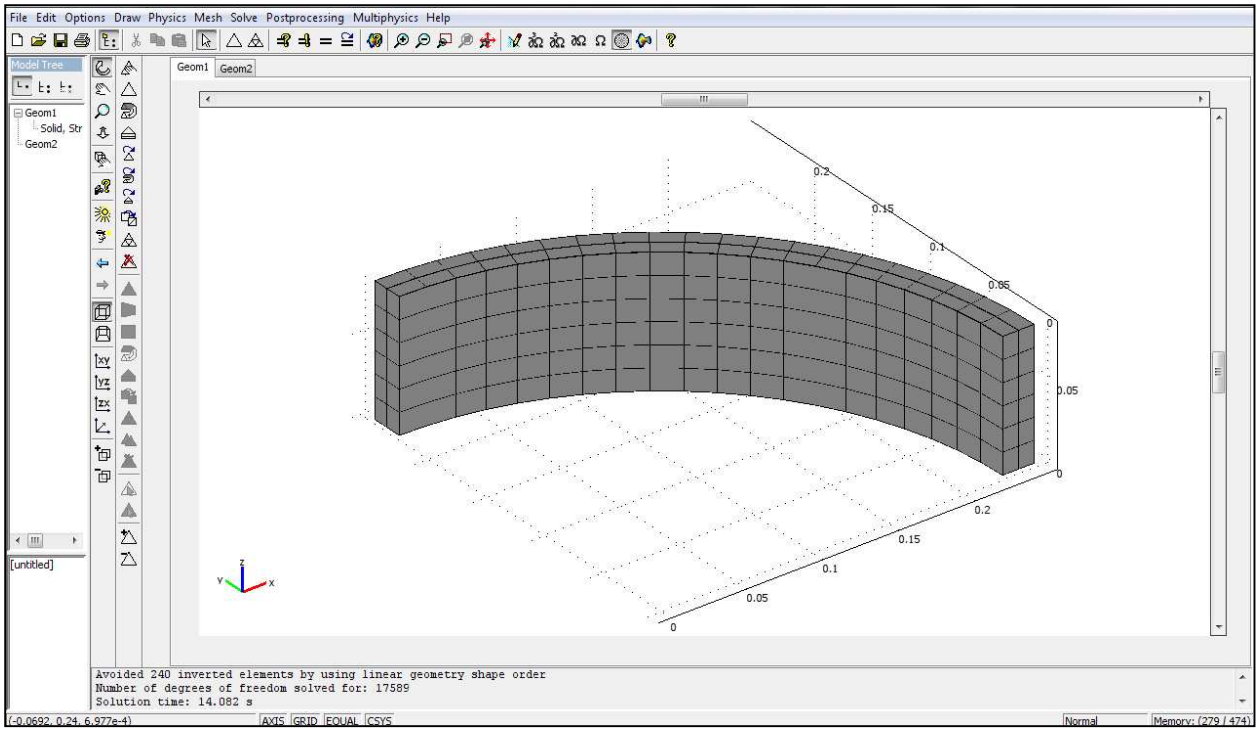


Figure 4.16 Meshed 3D Coil Geometry.

Chapter V

RESULTS AND DISCUSSION

5.1 Mathematical Modeling

5.1.1 Lamina Level Analysis Effects

The lamina level analysis results characterize the engineering constants *E, v, G*, and α for a lamina composed of copper wires imbedded in a cyanate ester resin. As stated earlier, the resin used was CTD-403. These mechanical constants were found with varying fiber volume fraction, and then they were described for off-axis behavior at three fiber volume fractions, namely 0.3, 0.4, and 0.5. A summary of the material properties used is provided below in Table 5.1. These values were input to the MATLAB code using the formulas described in the Methodology.

Figure 5.1 shows the Young's Moduli E_1 and E_2 with varying volume fraction. Figure 5.2 shows the Poisson's ratio v_{12} while Figure 5.3 shows shear modulus G_{12}, both with varying volume fraction. The results are as expected, with E_1 and v_{12} exhibiting linear rule of mixtures results. Also, E_2 and G_{12} exhibited modified rule of mixtures results because of off-axis effects discussed previously. E_1 and v_{12} vary linearly so increasing the fiber volume fraction will uniformly improve properties. However, both E_2 and G_{12} favor the matrix properties, especially at low fiber volume fractions meaning that transverse properties depend more on the matrix rigidity than the strength of the wires. One can conclude that at lower V_f the composite tends to favor matrix properties; therefore, increasing this fraction as much as possible will give better mechanical performance. The results of this section closely followed expected trends, and all values converged on pure matrix constants with a volume fraction of 0, and pure fiber constants with a volume fraction of 1.

Table 5.1 Material Properties for Lamina Level Analysis.

Copper (Wires) [30, 31]	CTD-403 (Matrix) [8]	Fiber Volume Fractions
E = 120.7 GPa	E = 37.9 GPa	V_{f1} = 0.3
G = 44.7 GPa	G = 15.8 GPa	V_{f2}= 0.4
v = 0.35	v = 0.20	V_{f3}= 0.5
α = 17 x10^{-6} K^{-1}	α = 52.96 x10^{-6} K^{-1}	

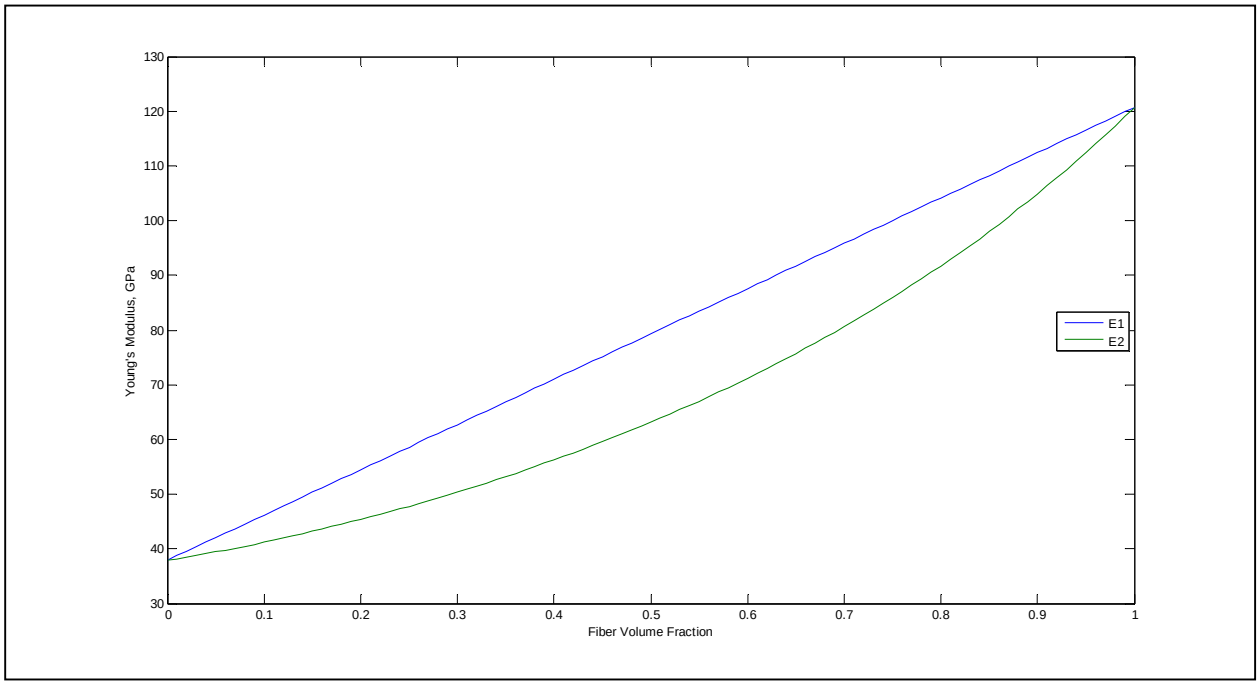


Figure 5.1 Young's Moduli E_1 and E_2 with Varying Fiber Volume Fraction. The rule of mixture based modulus in the longitudinal direction is linear, while the modified equation for transverse modulus has a parabolic shape.

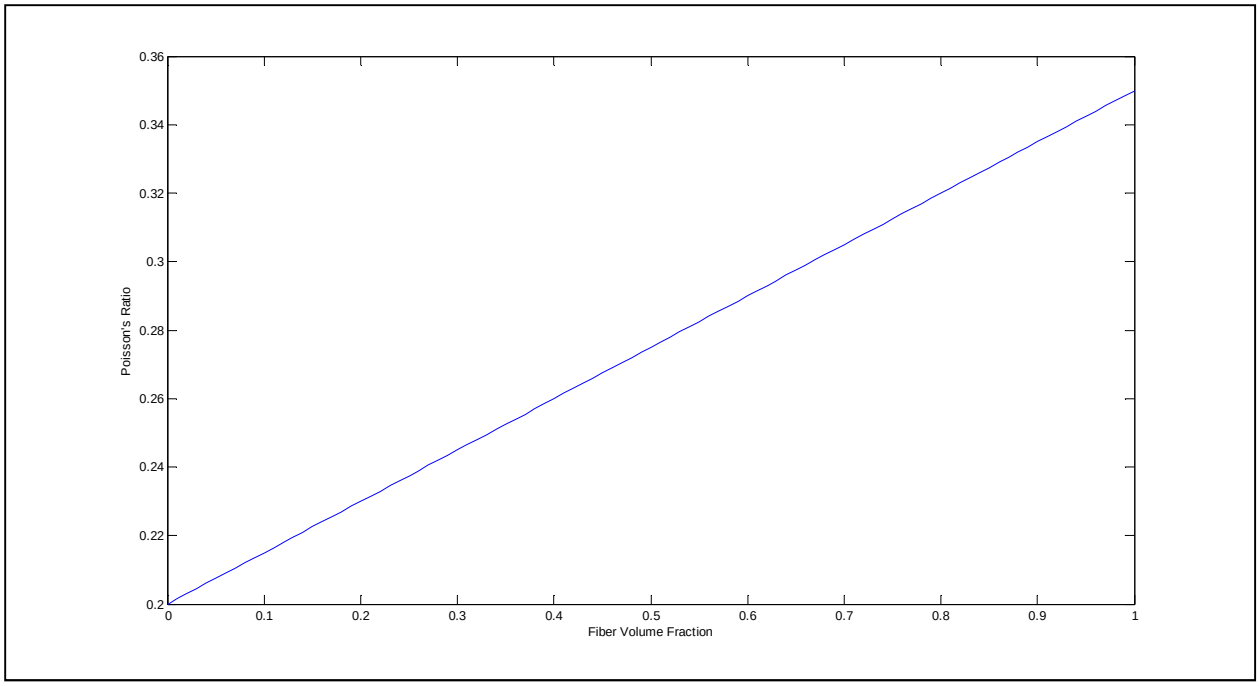


Figure 5.2 Poisson's Ratio v_{12} with Varying Fiber Volume Fraction. Poisson's ratio is linear based on the rule of mixture equation.

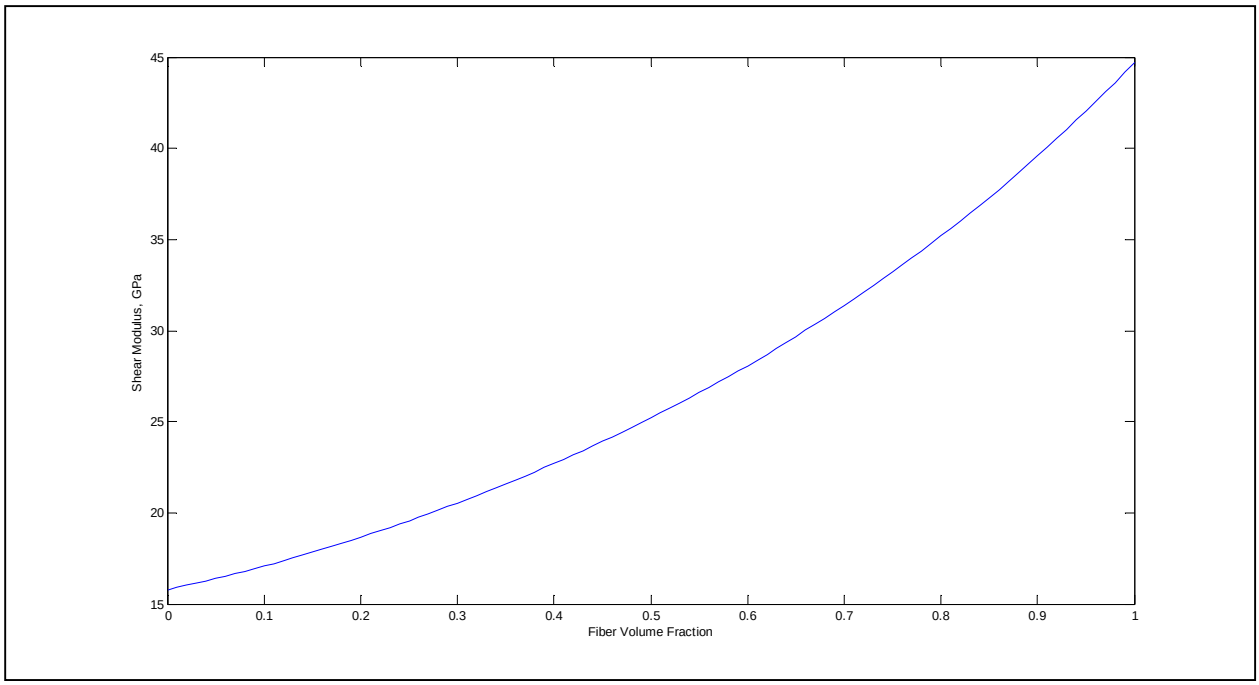


Figure 5.3 Shear Modulus G_{12} with Varying Fiber Volume Fraction. Modified shear equation makes this trend parabolic.

One important property to consider when studying a composite consisting of multiple laminae stacked to form a laminate is the off-axis behavior of the material. Therefore, the material properties as the orientation angle ϑ is varied from 0° (longitudinal fiber orientation) to 90° (transverse orientation) are provided below in Figures 5.4 – 5.8. Figure 5.4 is of the global elastic modulus E_x, Figures 5.5 and 5.6 show global transverse modulus E_y and global shear modulus G_{xy}, respectively, while Figures 5.7 and 5.8 show the Poisson's ratios v_{xy} and v_{yx}, respectively. Longitudinal and transverse Young's moduli have opposite trends; this is as expected since when the lamina is rotated 90° they will have effectively exchanged directions so that E_x becomes E_y and vice versa. For Young's modulus E_x, strength almost immediately drops off but becomes largely linear from 60° on up to 90° and the opposite for E_y. Shear modulus starts lower at 0°, peaks at 45°, and then returns to its original value again at 90°. This makes sense since shear effects will be maximum at a 45° offset angle and thus G_{xy} would become a larger factor in mechanical performance. Poisson's ratio v_{xy} has the most interesting curve, almost immediately increasing in value to peak at approximately 35°, then decreasing to below its starting value at 90°. Similarly to E_x and E_y, v_{yx} experiences the opposite trend of v_{xy}. In all of these mechanical properties, the largest fiber volume fraction (0.5) experienced the largest values of the properties, while 0.4 and 0.3 volume fractions had uniformly lower values. Therefore, as with the local material constants, the global off-axis mechanical properties of the composite increase in value as the fiber volume fraction was increased. The difference in the properties caused by the variation in fiber volume fraction, however, is not uniform for the properties; this is summarized by Table 5.2. As seen in the table, both elastic moduli and the shear modulus have very similar effects from altering the fiber volume fraction of around a 25% increase in properties from 0.3 to 0.5 V_f, but both the Poisson's ratios are affected by only about half as much at around 12%. Therefore one can conclude that the moduli are much more susceptible to variation in the volume fractions of wires whereas the Poisson's ratios are varied only half as much over the same fiber volume fraction range.

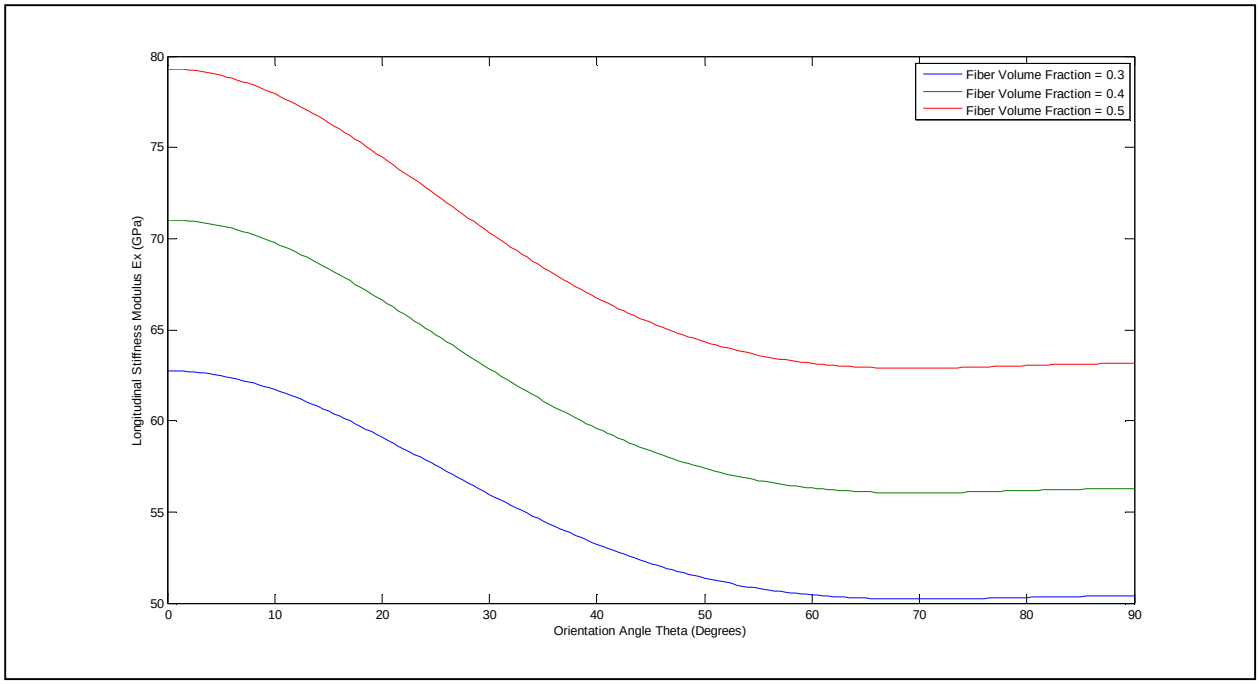


Figure 5.4 Variation of E_x as a Function of Orientation Angle ϑ. Modulus increases uniformly with volume fraction for all offset angles.

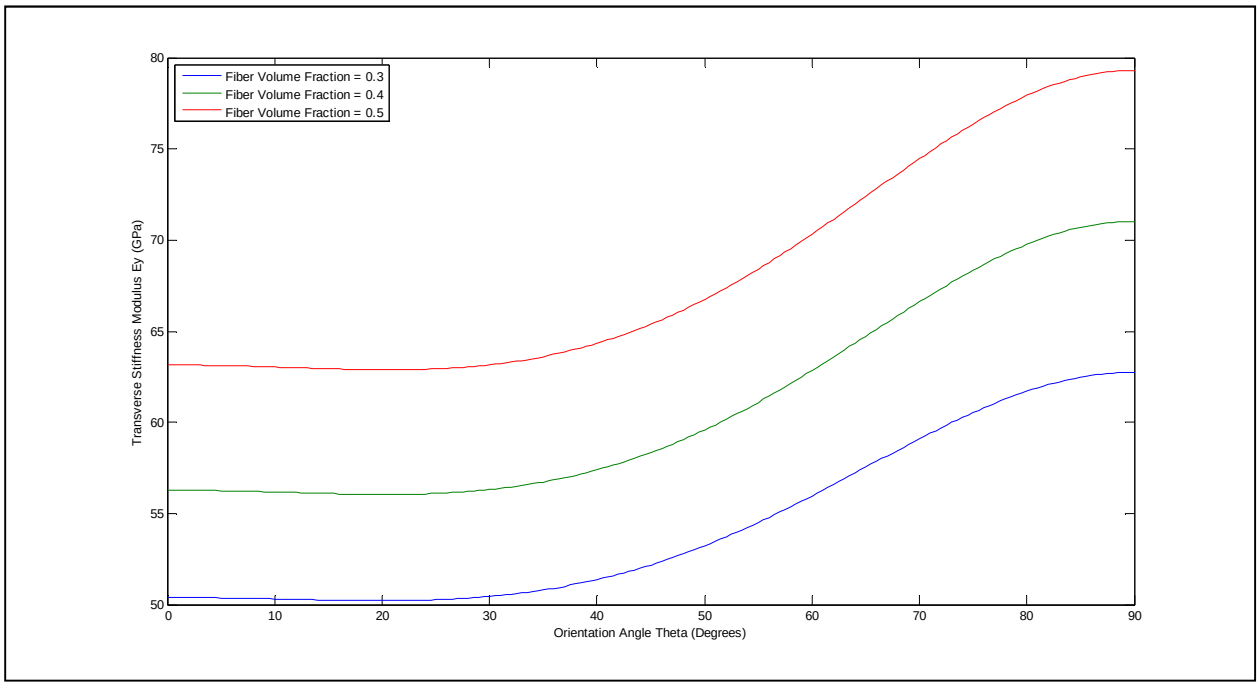


Figure 5.5 Variation of E_y as a Function of Orientation Angle ϑ. Modulus increases uniformly with volume fraction for all offset angles.

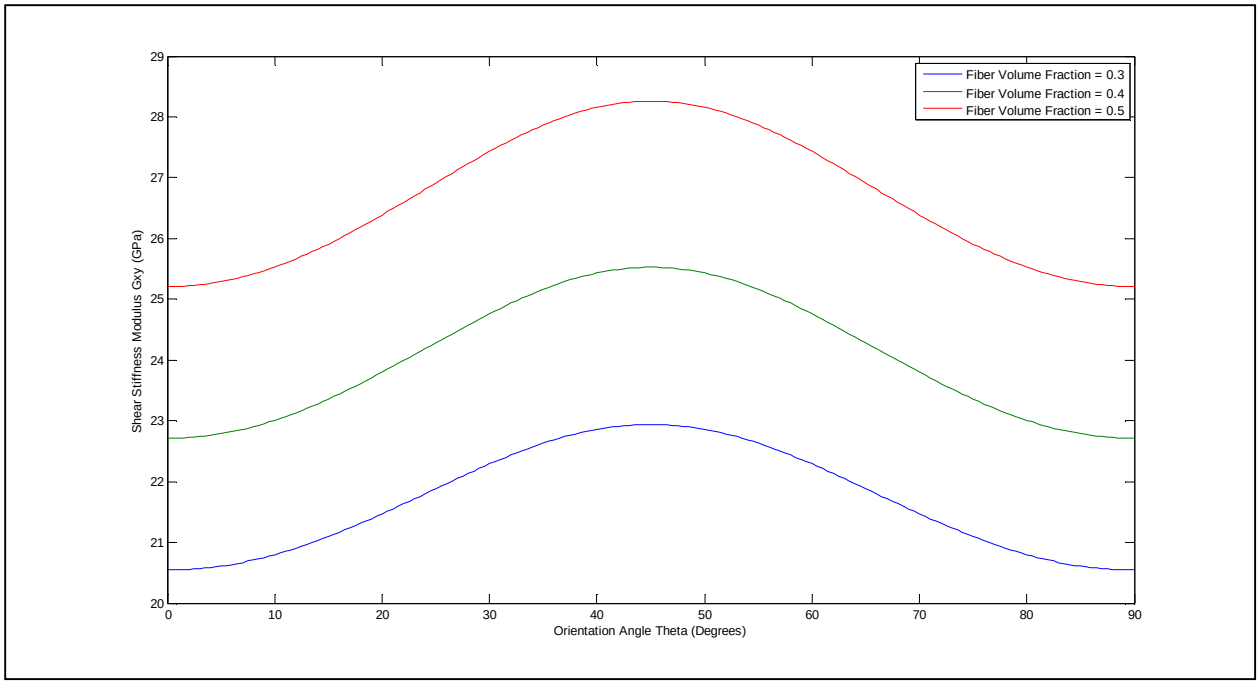


Figure 5.6 Variation of G_{xy} as a Function of Orientation Angle ϑ. Modulus increases uniformly with volume fraction for all offset angles.

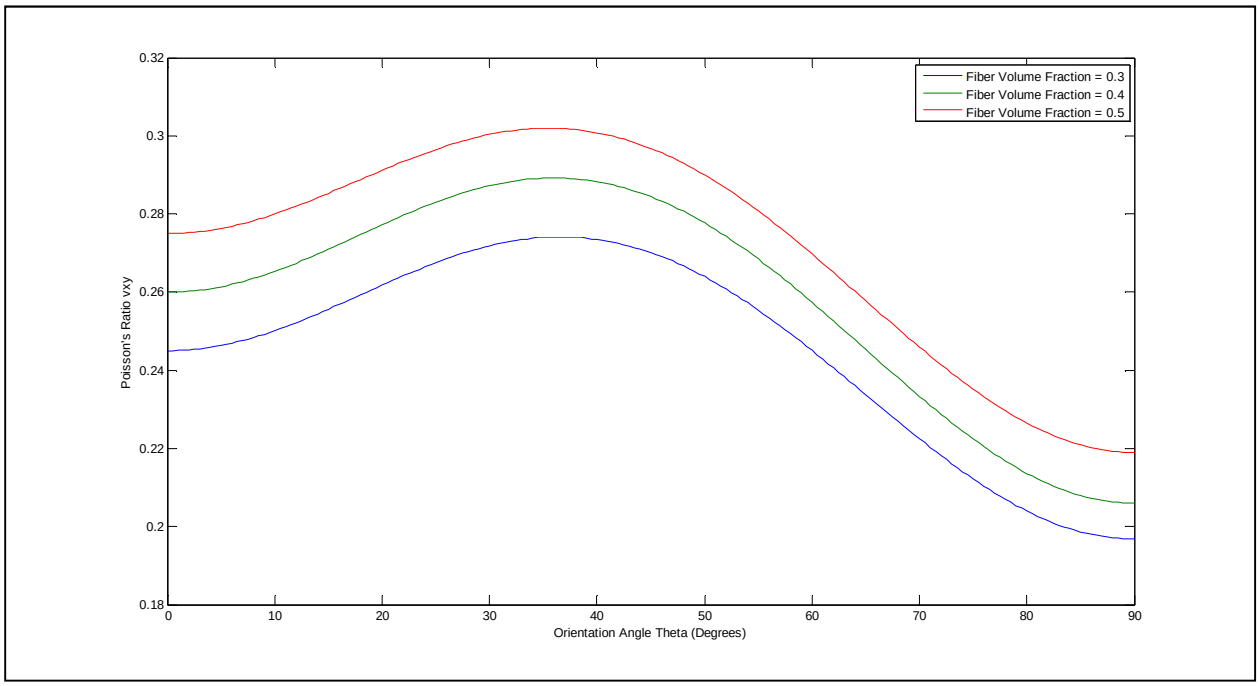


Figure 5.7 Variation of v_{xy} as a Function of Orientation Angle ϑ. Poisson's ratio increases uniformly with volume fraction for all offset angles.

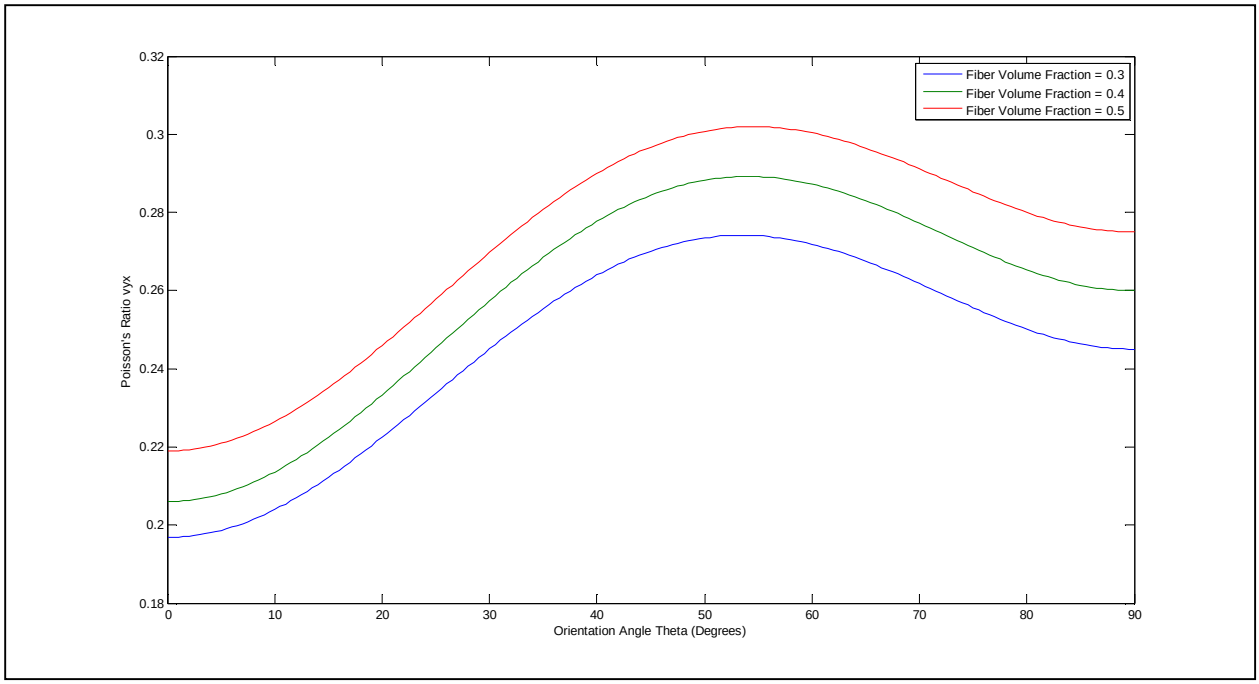


Figure 5.8 Variation of v_{yx} as a Function of Orientation Angle ϑ. Poisson's ratio increases uniformly with volume fraction for all offset angles.

Table 5.2 Difference in Material Properties from 0.3 to 0.5 Volume Fractions.

V_f	E_x	E_y	G_{xy}	ν_{xy}	ν_{yx}
0.3	62.74	50.39	20.54	0.245	0.197
0.4	71.02	56.27	22.71	0.260	0.208
0.5	79.30	63.15	25.21	0.275	0.219
Difference	**26.39%**	**25.32%**	**22.74%**	**12.24%**	**11.17%**

[1]Units of GPa.

The thermal property analysis follows a similar pattern to that of the mechanical properties; there is a local lamina analysis that looks at longitudinal and transverse thermal expansion coefficients α_1 and α_2, respectively, and then a global off-axis analysis to determine coefficients of thermal deformation α_x, α_y, and α_{xy}. The longitudinal coefficient of thermal expansion α_1 and the transverse CTE α_2 results are shown below in Figure 5.9. As with the mechanical properties, the thermal values exhibit full matrix values at 0 volume fraction, and full fiber values at $V_f = 1$. However, the curves decrease in value since the CTE of the matrix is greater than that of the wires. Furthermore, for thermal coefficients the transverse direction has rule of mixtures linearity and the longitudinal direction displays modified behavior favoring the wires.

The off-axis behavior of the thermal coefficients was examined next. Figure 5.10 shows the variation in α_x with varying orientation angle and Figure 5.11 shows the variation in α_y while orientation angle varies. Figure 5.12 is an illustration of how increasing angle offset affects coefficient of thermal deformation α_{xy}. α_x and α_y both follow a similar pattern to the Young's modulus values shown in Figures 5.4 and 5.5 as the trend looks very similar and both are mirror images of each other. The only real difference is that the curves do not flatten out at the end but rather have a uniform curvature. In these curves the lowest fiber volume fraction yielded the highest CTE while increasing fiber content led to a decrease in CTEs. This is to be expected since the wires did have a lower CTE than the matrix, so increasing their volume fraction should intuitively lead to lower properties. However, this is not quite the case for the off-axis properties. At 0° and 90° the composite did not experience any shear effects, but once it is off-axis, it immediately has a coupling CTE value. As expected, this is maximum at 45° and has a uniform inverse parabolic shape. Because the shear coefficient of thermal expansion is an order of magnitude lower than either of the other CTEs, its effect would be less of a factor than α_x and α_y. Interestingly, the coefficient α_{xy} is unique in that increasing the fiber volume fraction does not appear to uniformly affect its magnitude like all the other parameters considered so far. As expected, at $V_f = 0.5$ the shear

coefficient was the lowest, but α_{xy} at volume fraction 0.3 is actually lower than that at 0.4. The differences between $V_f = 0.3$ and $V_f = 0.5$ for α_x and α_y were found to be 17.05% and 20.56%, respectively, which is comparable to the trend found for the mechanical properties. However, for the CTE α_{xy} this value was found to be only 5.42%. Such a small variation in α_{xy} suggests that increasing the volume fraction is not a deciding factor in thermal shear. This result is surprising, but given that the thermal coefficient α_{xy} is so much lower than the other CTEs, this irregularity does not seem to have much effect on the overall material behavior.

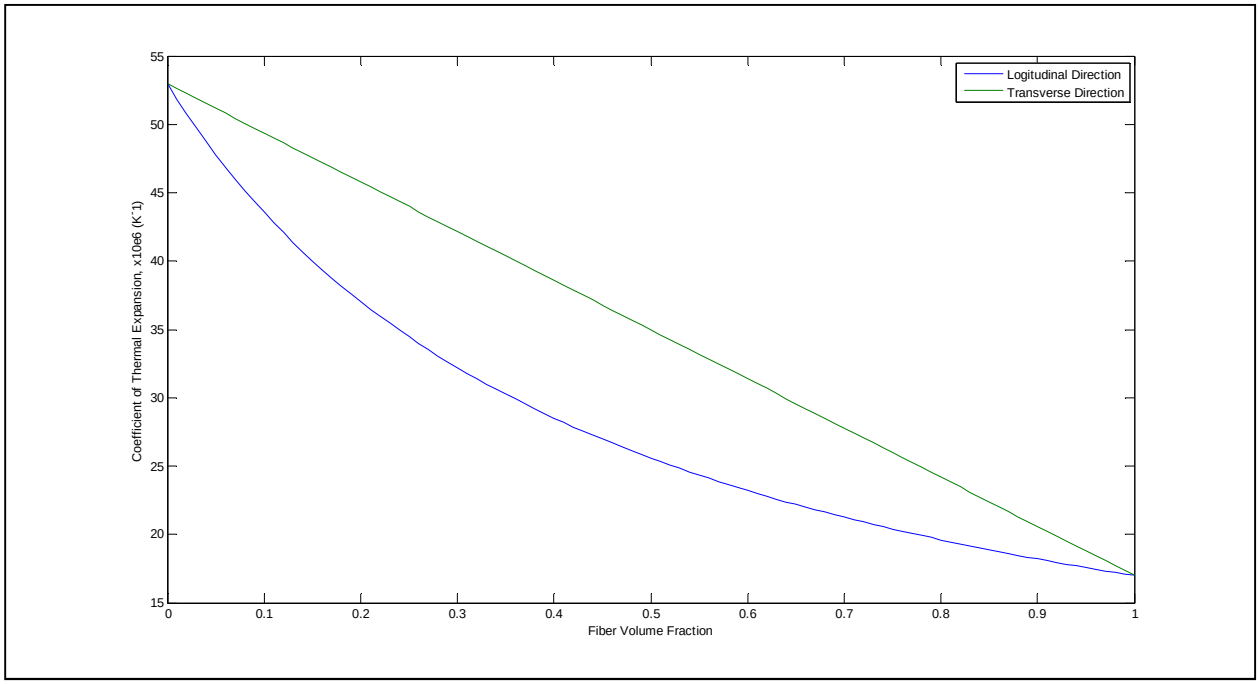


Figure 5.9 Longitudinal and Transverse CTE's α_1 and α_2 with Varying Fiber Volume Fraction. Thermal constants are opposite of mechanical properties, with linear transverse properties and parabolic longitudinal properties.

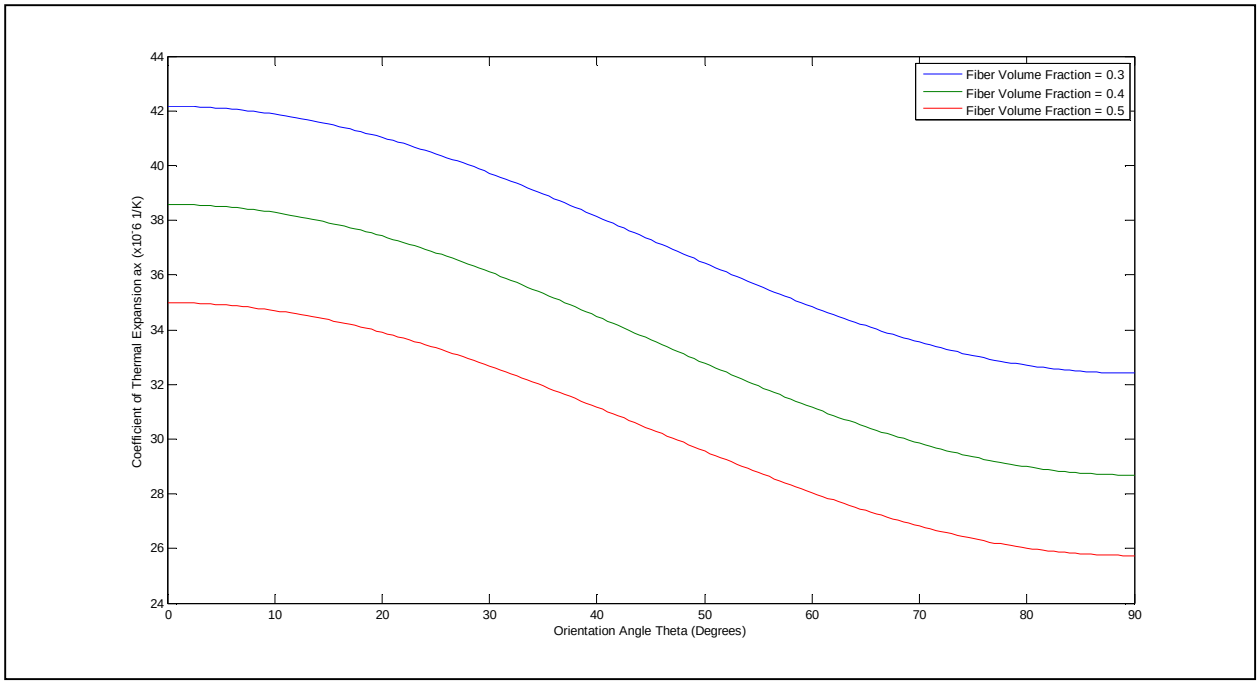


Figure 5.10 Variation of α_x as a Function of Orientation Angle ϑ. CTE decreases uniformly with volume fraction for all offset angles.

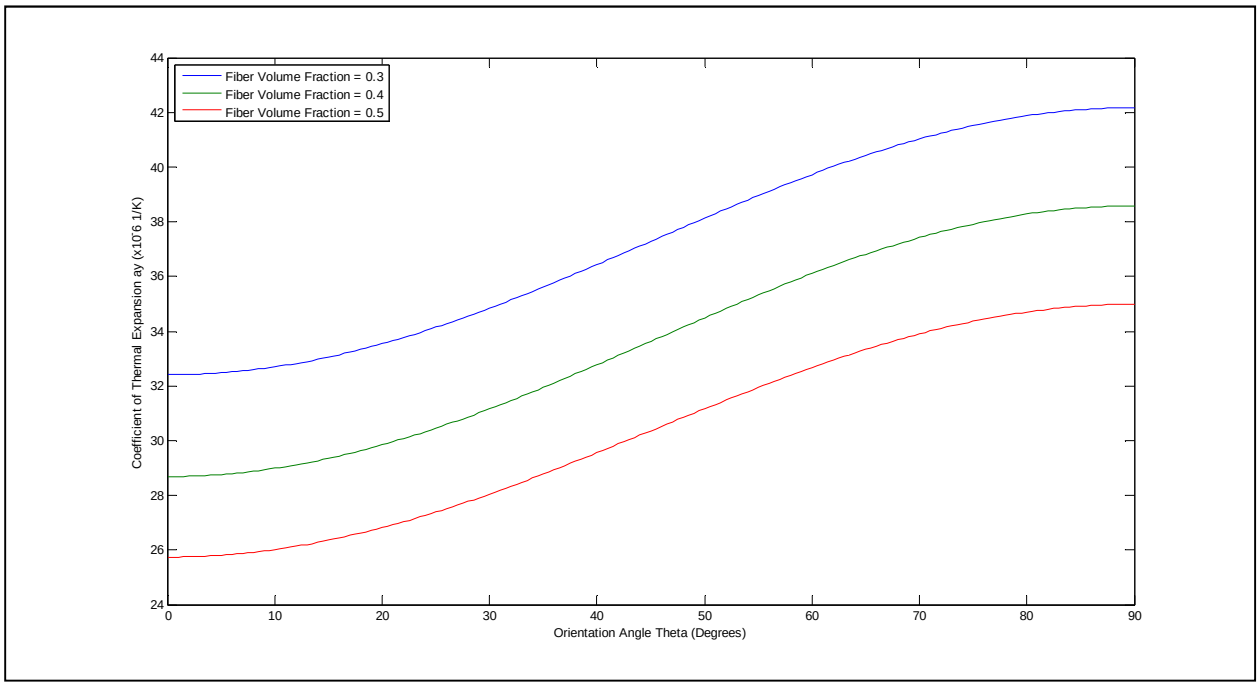


Figure 5.11 Variation of α_y as a Function of Orientation Angle ϑ. CTE decreases uniformly with volume fraction for all offset angles.

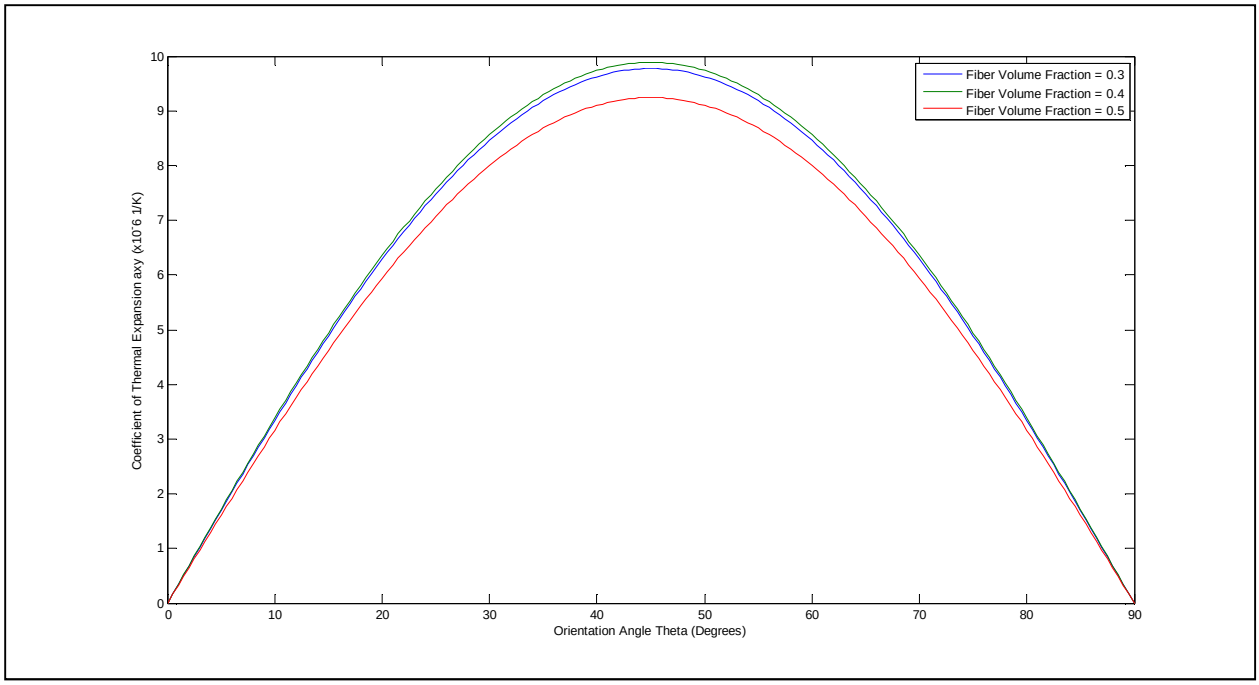


Figure 5.12 Variation of α_{xy} as a Function of Orientation Angle ϑ. CTE does not vary uniformly for α_{xy}.

5.1.2 Laminate Level Analysis Effects

The laminate level analysis is built upon the results of the lamina level analysis. The results will characterize the stresses in the laminate due to thermal loading, pressure loading, and a combination of both. Although there are no closed form equations that directly relate the stress and the fiber volume fraction, it has been shown previously how varying fiber volume fraction affects the composite material constants; thus, these constants can be used to observe how the stresses are affected by V_f. The material properties input into the model for the various fiber volume fractions are shown in Table 5.3. As previously discussed the mechanical properties are directly proportional to fiber volume fraction, while the thermal properties experience an inversely proportional trend. These mechanical values were used to find the compliance matrices for the composite and insulation using the equations in (3.30). The composite structure analyzed consists of two composite layers with an insulation layer in between.

Although the properties of the material are outlined in Table 5.3, this tells nothing about the specifications of the composite cylinder that uses these materials. Table 5.4 shows the various specifications of the composite cylinder. The pressure and temperature loadings shown are the values tested.

First, purely mechanical loading was tested for all three fiber volume fractions. This was the pressure load outlined in Table 5.4 (200 MPa) applied to the inside surface of the cylinder. A plot of the stress in the cylinder layers for the three fiber volume fractions in the *X* direction (fiber direction) is shown in Figure 5.13, while the same plots for the *Y* direction and shear in the *X*-*Y* plane are seen in Figures 5.14 and 5.15, respectively. While altering the fiber volume fraction for the pressure load did little to change the stress in the composite layers, the main effect was seen in the insulation. The composite stress did increase slightly with increasing fiber volume fraction, but the stress in the insulation layer actually decreased for the *X* and *Y* directions. The shear in the composite layers was relatively small, and shear in the insulation increased with increasing V_f.

Table 5.3 Material Properties for Laminate Level Analysis.

	Copper/Cyanate Ester Composite			**S2 Glass Insulation [32,33]**
Volume Fraction	$V_f = 0.3$	$V_f = 0.4$	$V_f = 0.5$	N/A
E_1 **(GPa)**	62.74	71.02	79.30	12.0
E_2 **(GPa)**	50.39	56.27	63.15	20.0
G_{12} **(GPa)**	20.54	22.71	25.20	6.0
ν_{12}	0.245	0.260	0.275	0.33
α_1 **(x 10^{-6} 1/K)**	42.17	38.58	34.98	16.5
α_2 **(x 10^{-6} 1/K)**	32.40	28.69	25.74	5.2

Table 5.4 Composite Cylinder Specifications [8, 33].

Property	Value
Cylinder Inner Diameter	45 cm
Composite Layer Dimensions	1 cm x 1 cm
Insulation Thickness	0.46 mm
Number of Turns	16
Number of Layers	2
Current in the Wires	100 kA
Angle offset of Insulation	18°
Pressure	200 MPa
Temperature Differential	150 K

The next test was performed for a uniform thermal load of 150 K differential through the cylinder. The results for this are shown in Figures 5.16 through 5.18. A much larger effect of fiber volume fraction was seen in the longitudinal and transverse stresses for thermal loading, with increasing fiber volume fraction resulting in an increase in stress in the composite layers and a corresponding decrease in insulation stress. The final test was simply a combination of pressure and thermal loading and was performed primarily for the sake of completeness. The results are illustrated in Figures 5.19 through 5.21. This follows the same trends as the pressure loading. A summary of the results is shown in Tables 5.5 and 5.6 below.

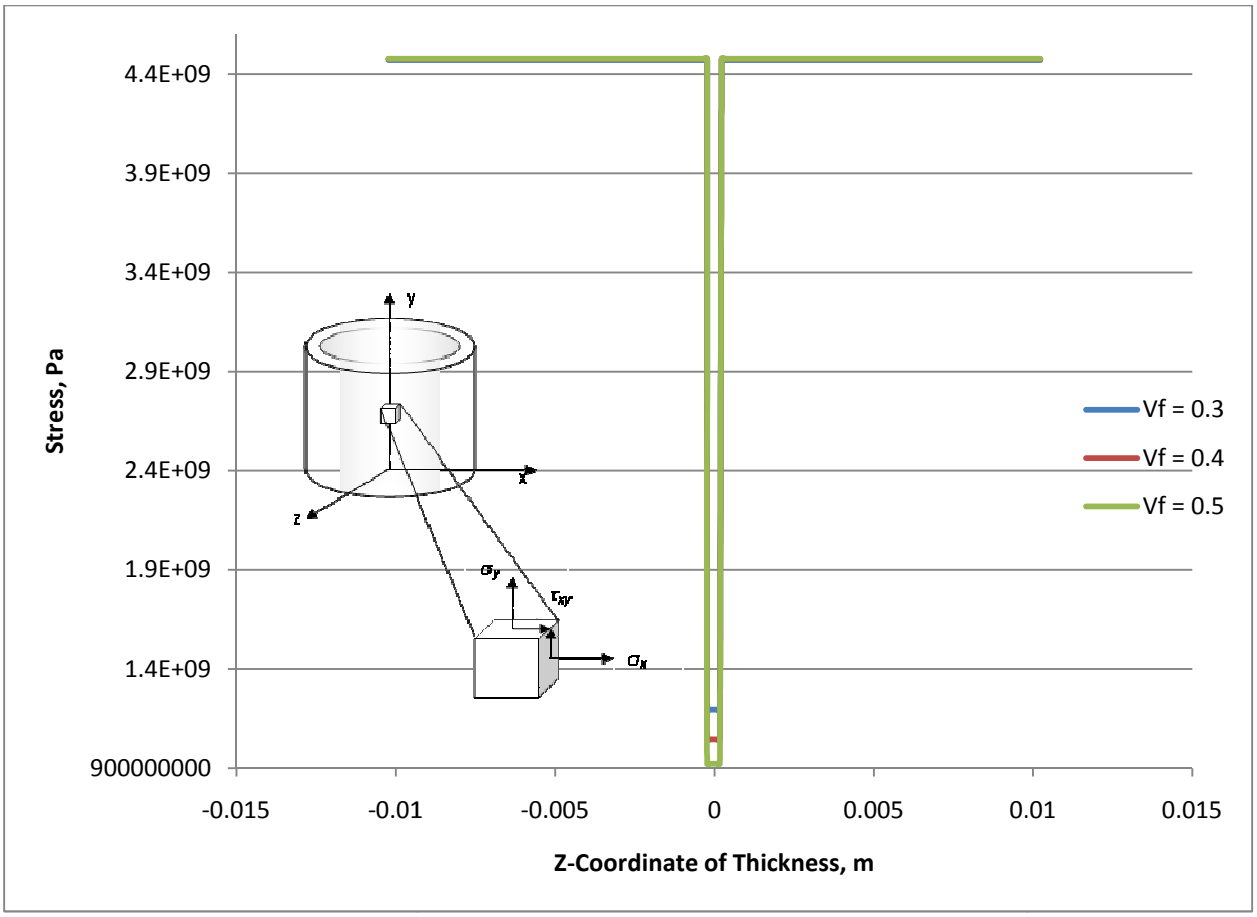


Figure 5.13 Stress in *X* Direction Due to Mechanical Loading. The curves show changes in stress for three fiber volume fractions for a uniform pressure load.

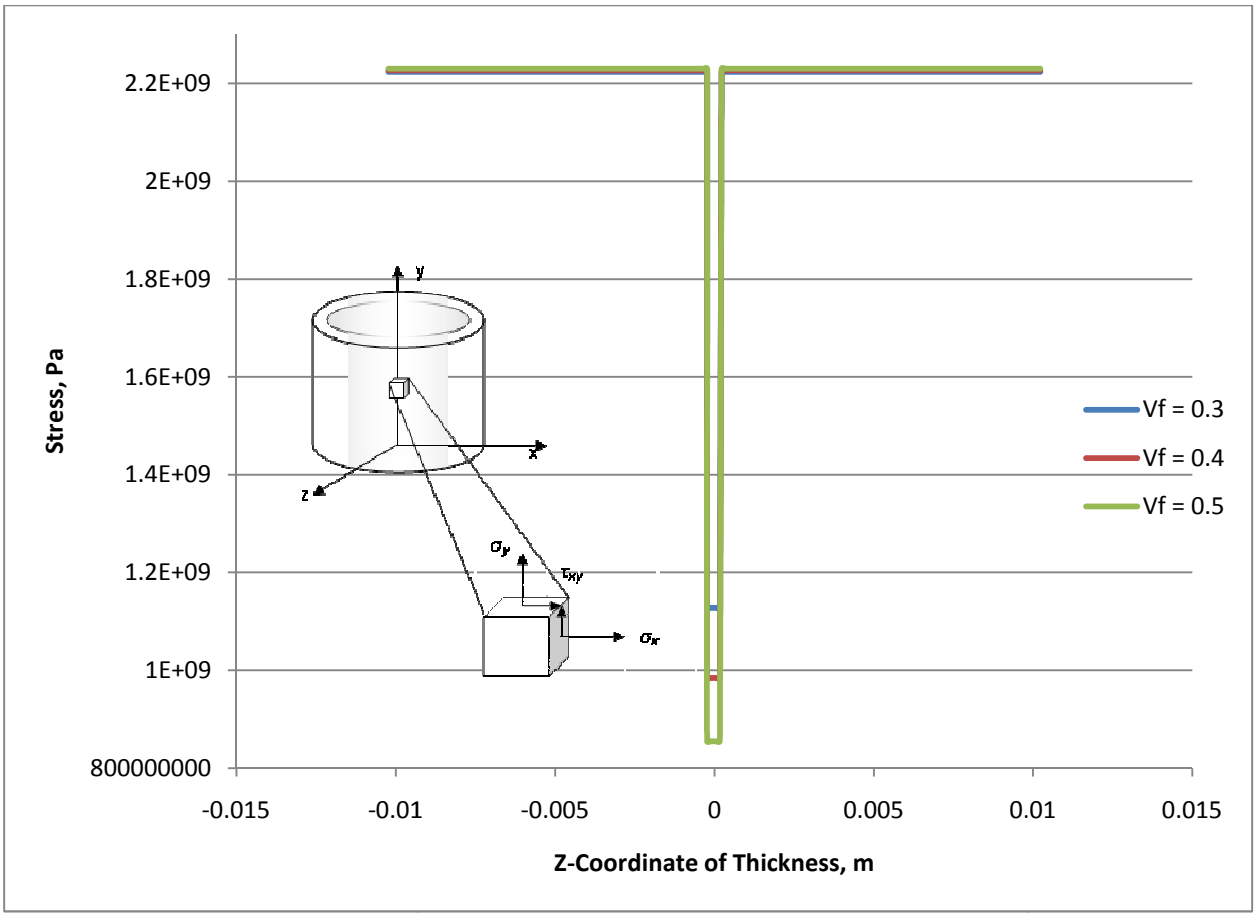


Figure 5.14 Stress in *Y* Direction Due to Mechanical Loading. The curves show changes in stress for three fiber volume fractions for a uniform pressure load.

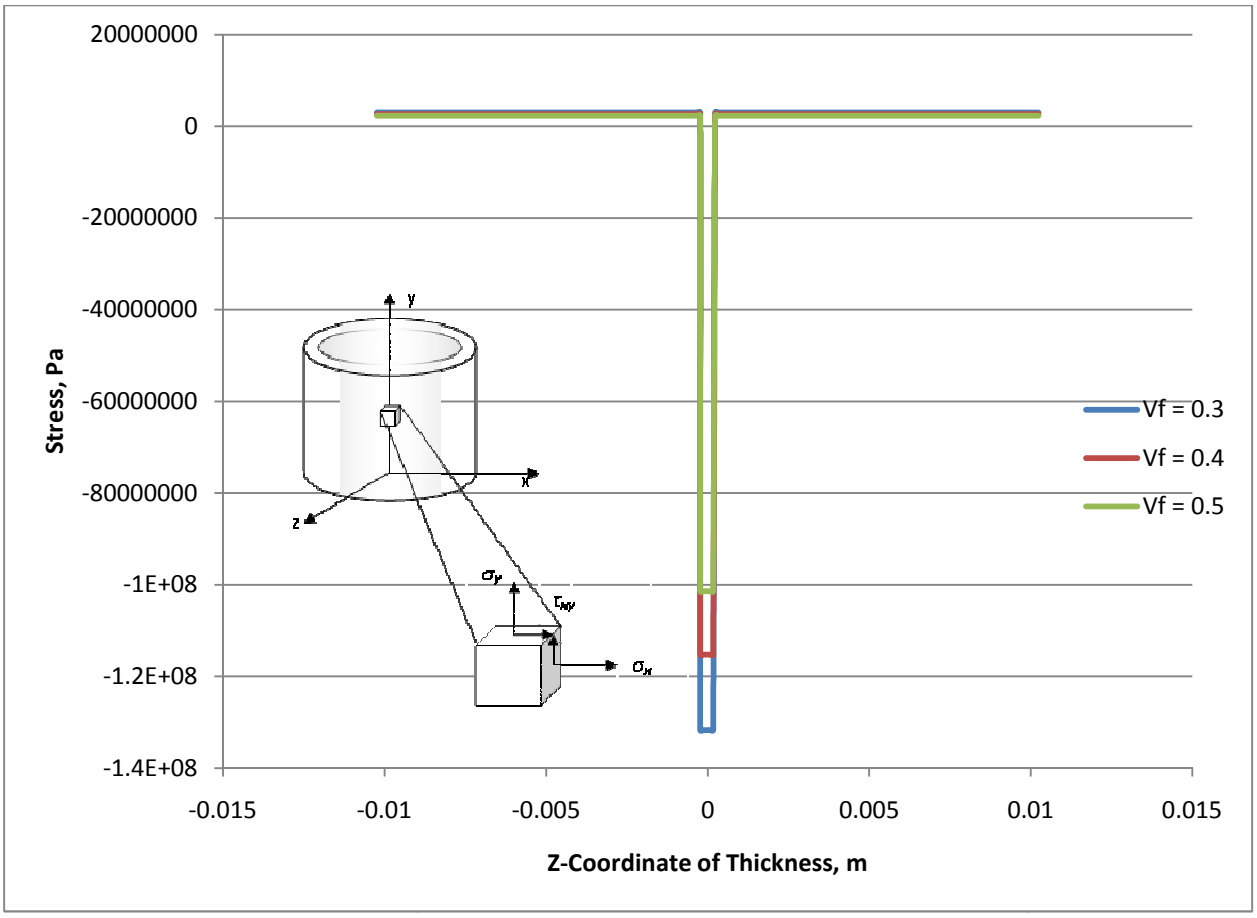


Figure 5.15 Stress in *X-Y* Plane Due to Mechanical Loading. The curves show changes in stress for three fiber volume fractions for a uniform pressure load.

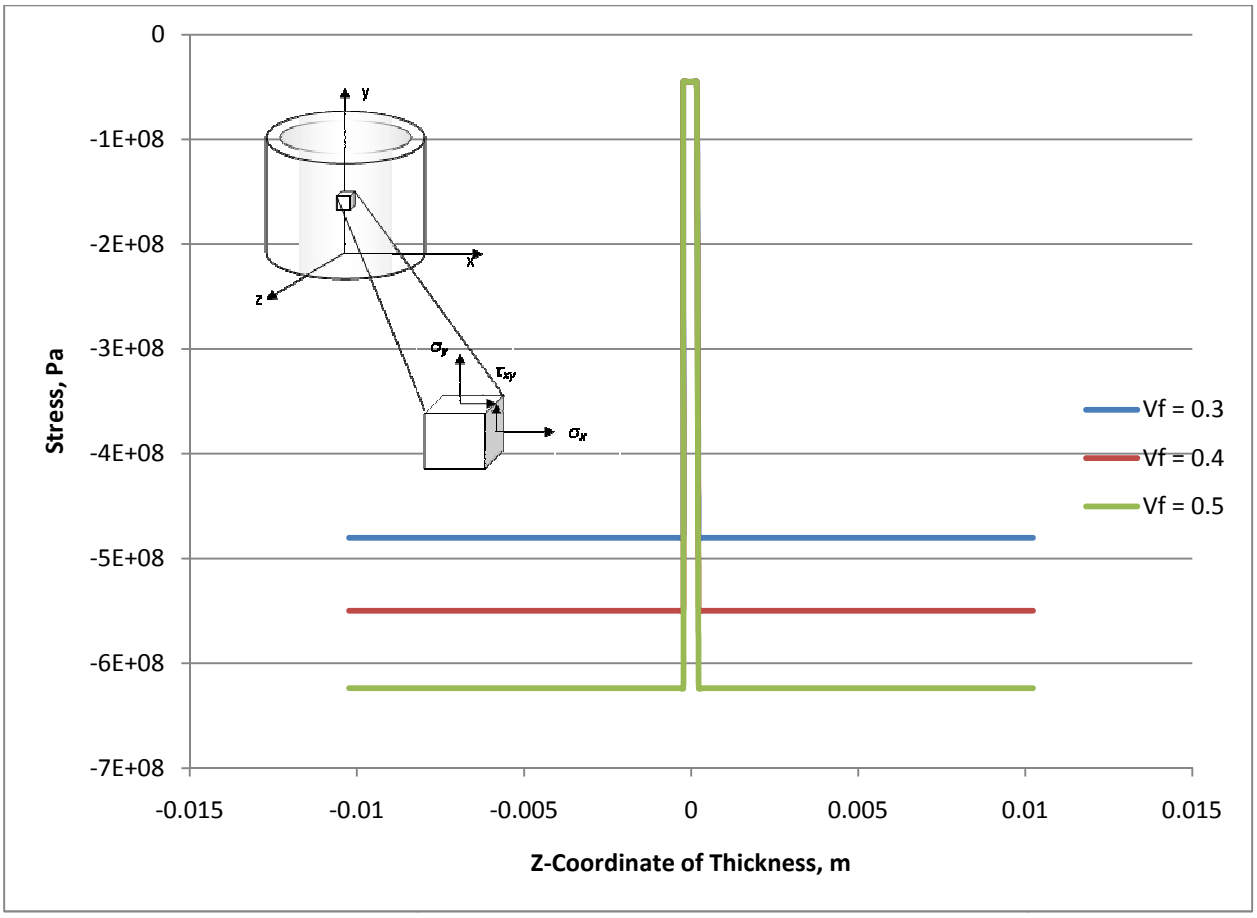


Figure 5.16 Stress in *X* Direction Due to Thermal Loading. The curves show changes in stress for three fiber volume fractions for a uniform temperature load.

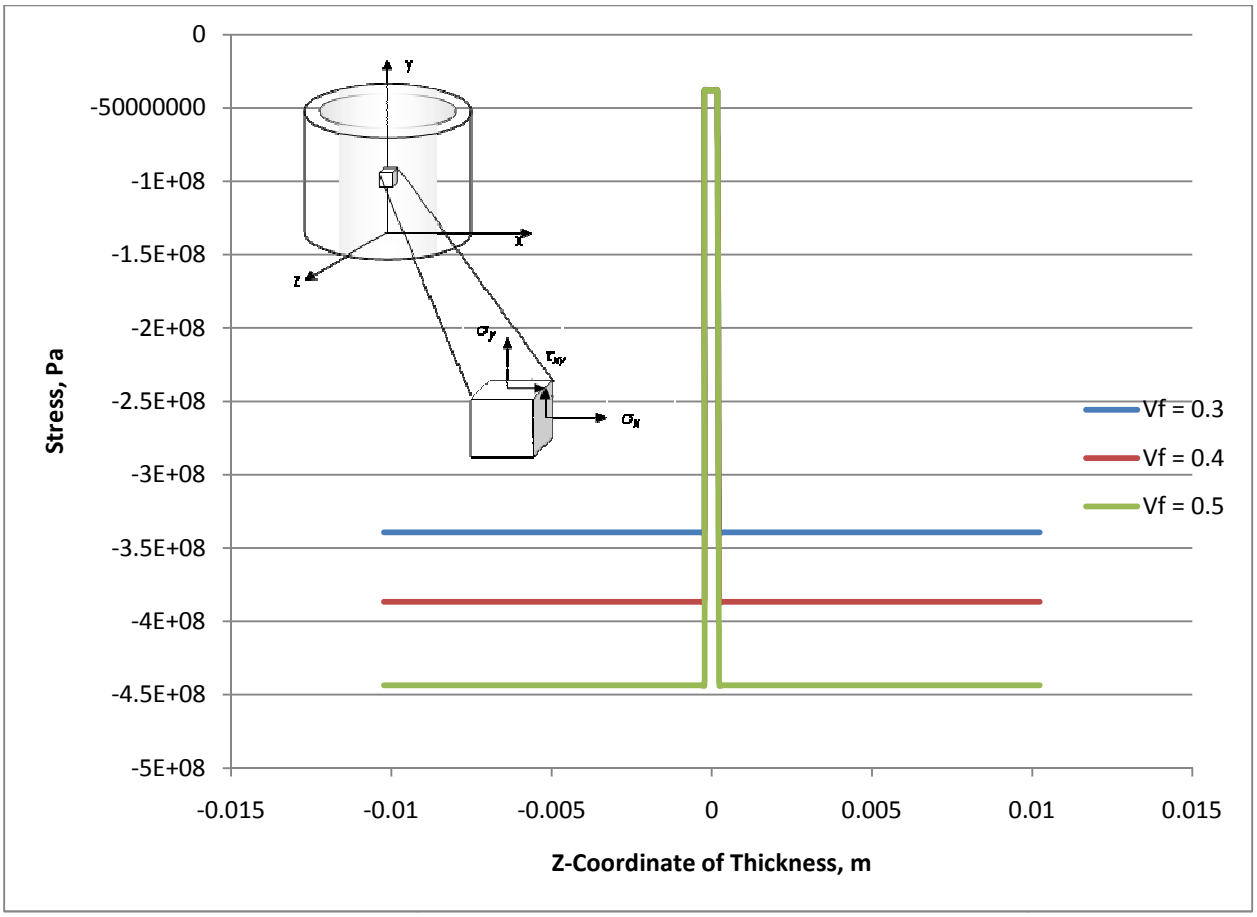


Figure 5.17 Stress in *Y* Direction Due to Thermal Loading. The curves show changes in stress for three fiber volume fractions for a uniform temperature load.

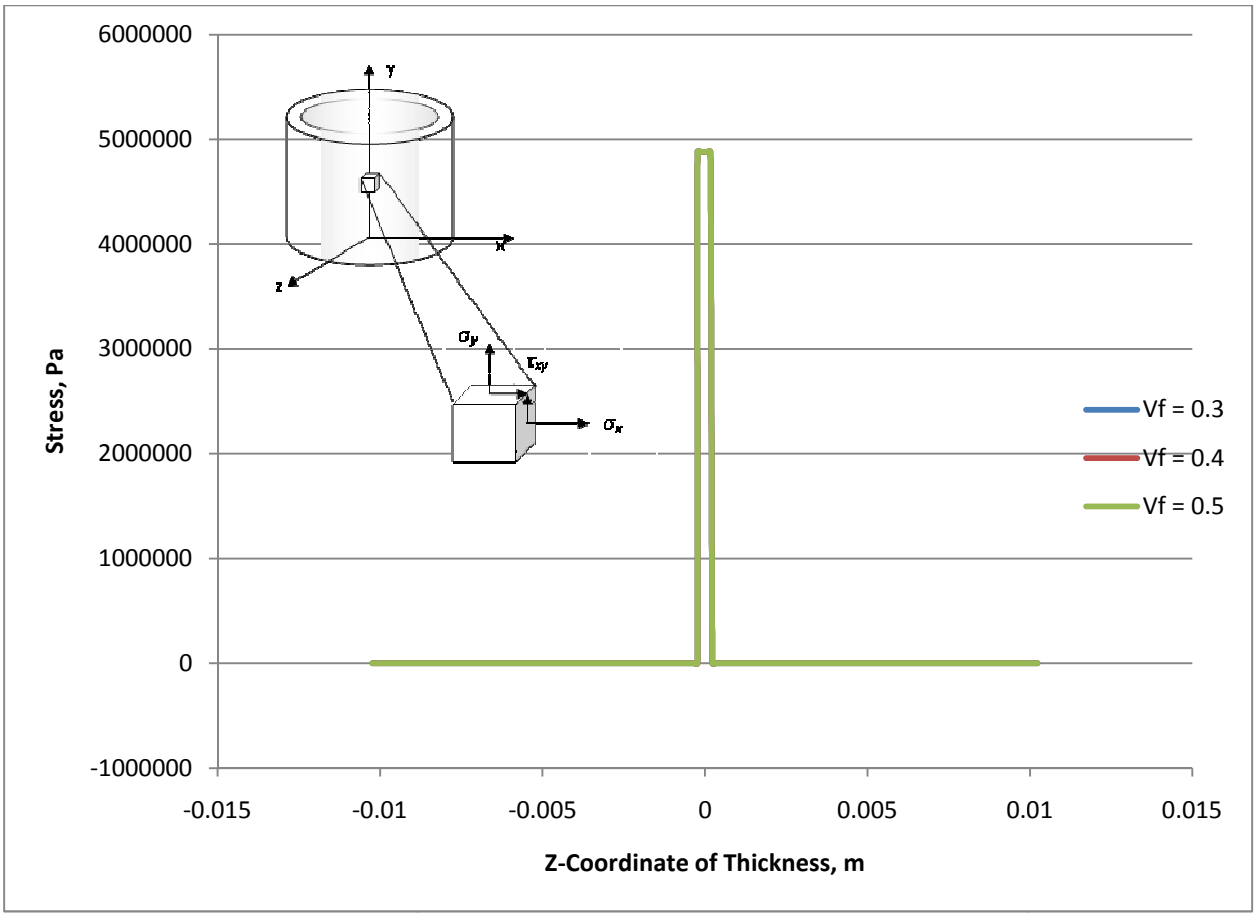


Figure 5.18 Stress in *X-Y* Plane Due to Thermal Loading. The curves show changes in stress for three fiber volume fractions for a uniform temperature load.

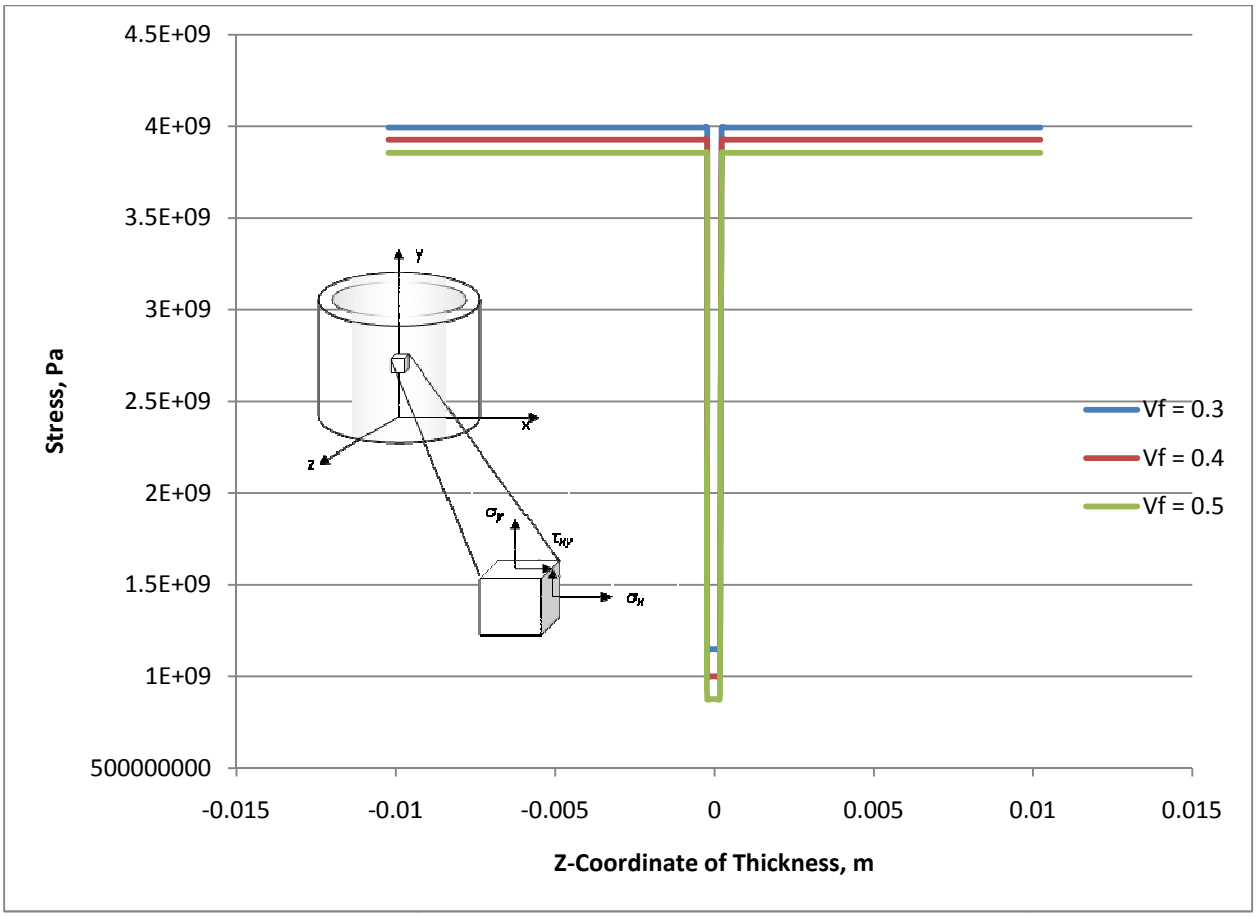


Figure 5.19 Stress in *X* Direction Due to Combined Loading. The curves show changes in stress for three fiber volume fractions for a combined load of temperature and pressure.

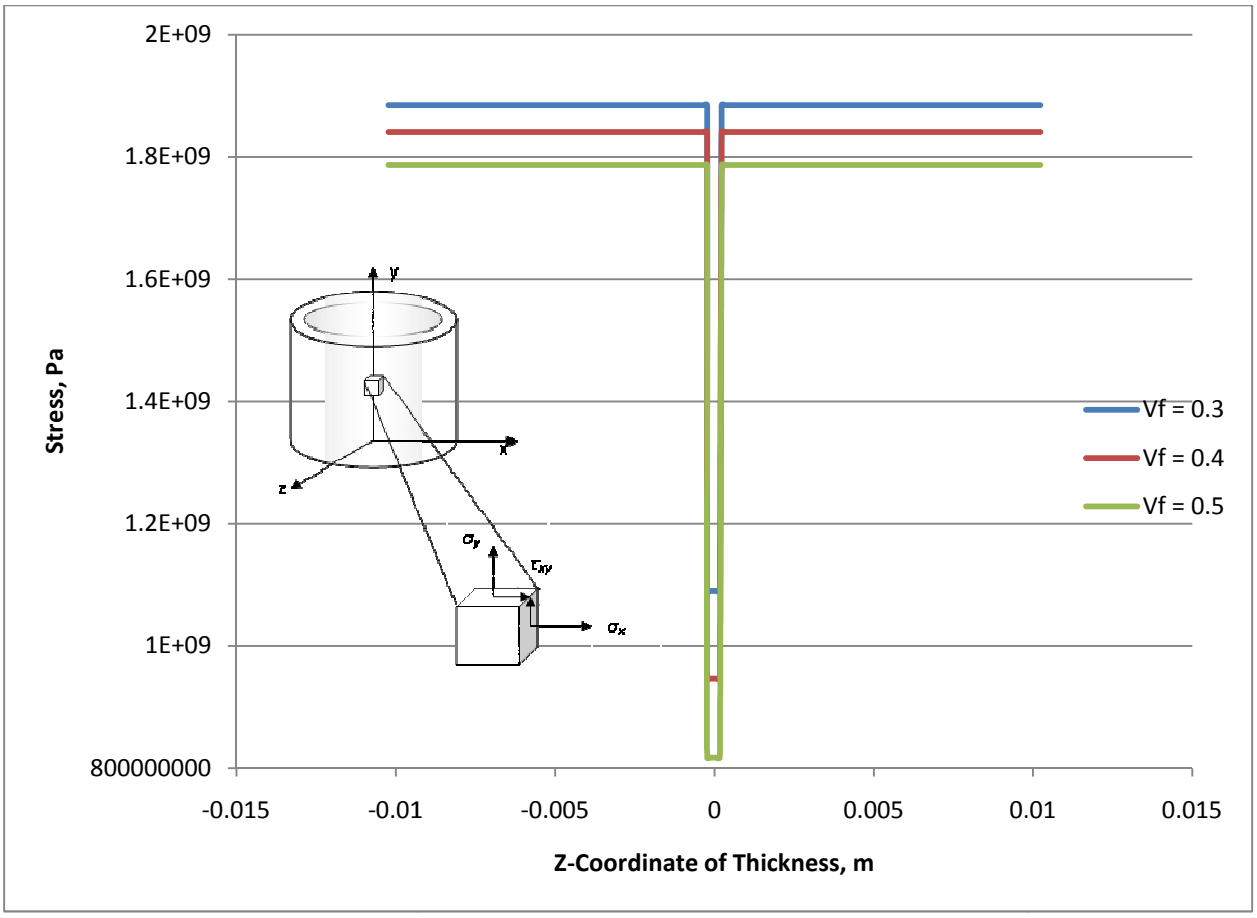


Figure 5.20 Stress in *Y* Direction Due to Combined Loading. The curves show changes in stress for three fiber volume fractions for a combined load of temperature and pressure.

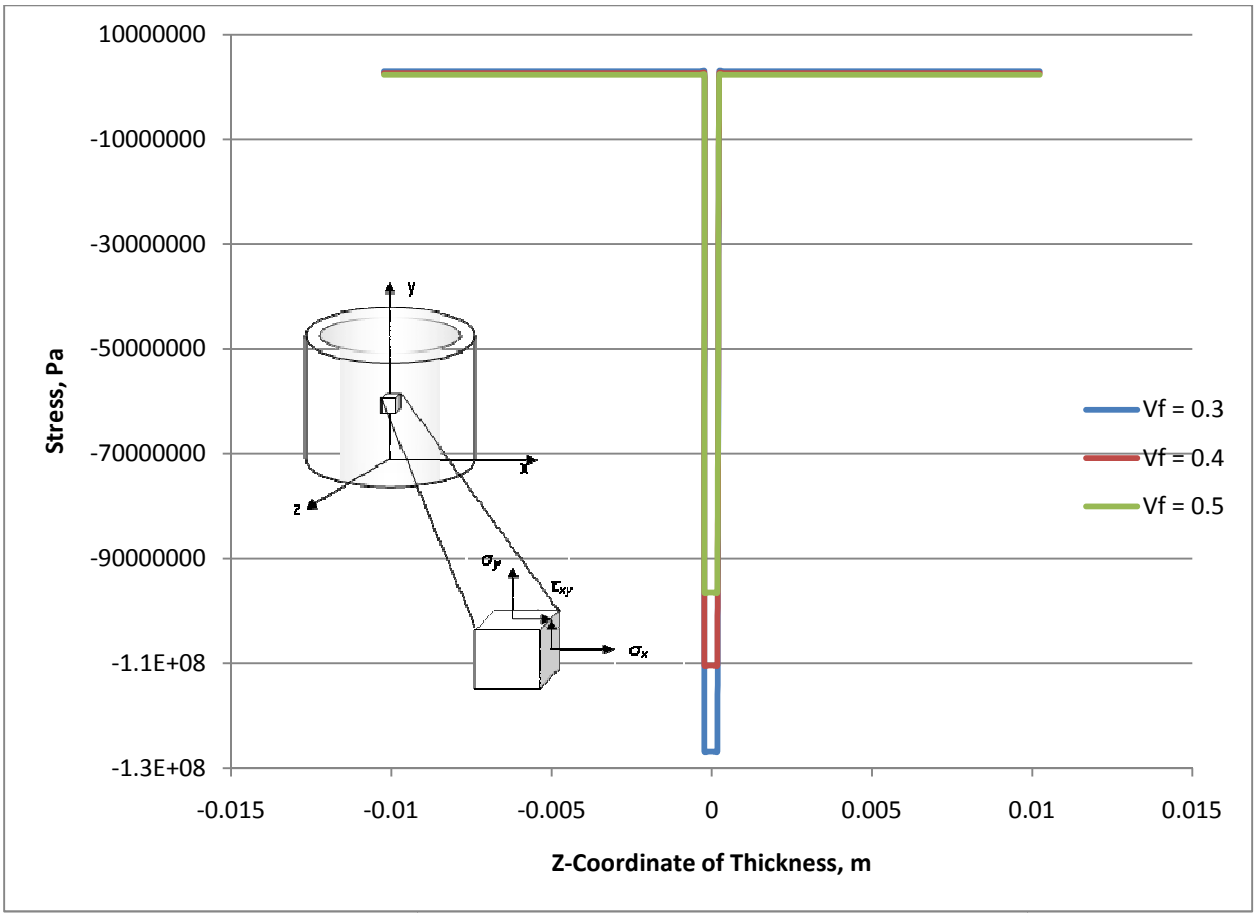


Figure 5.21 Stress in *X-Y* Plane Due to Combined Loading. The curves show changes in stress for three fiber volume fractions for a combined load of temperature and pressure.

Table 5.5 Summary of Laminate Level Analysis Results for Composite Layers.

Volume Fraction	Pressure			Temperature			Combined		
	Stress σ_x	Stress σ_y	Stress τ_{xy}	Stress σ_x	Stress σ_y	Stress τ_{xy}	Stress σ_x	Stress σ_y	Stress τ_{xy}
V_f = 0.3	4.47E+09	2.22E+09	3.03E+06	-4.80E+08	-3.39E+08	0.00E+00	3.99E+09	1.88E+09	3.03E+06
V_f = 0.4	4.48E+09	2.23E+09	2.65E+06	-5.50E+08	-3.87E+08	0.00E+00	3.93E+09	1.84E+09	2.65E+06
V_f = 0.5	4.48E+09	2.23E+09	2.33E+06	-6.24E+08	-4.43E+08	0.00E+00	3.86E+09	1.79E+09	2.33E+06
% Change	**0.14%**	**0.28%**	**-23.01%**	**29.90%**	**30.69%**	**0.00%**	**-3.44%**	**-5.19%**	**-23.01%**

Note: Units of Stress are Pa.

Table 5.6 Summary of Laminate Level Analysis Results for Insulation Layer.

Volume Fraction	Pressure			Temperature			Combined		
	Stress σ_x	Stress σ_y	Stress τ_{xy}	Stress σ_x	Stress σ_y	Stress τ_{xy}	Stress σ_x	Stress σ_y	Stress τ_{xy}
V_f = 0.3	1.19E+09	1.13E+09	-1.32E+08	-4.50E+07	-3.81E+07	4.88E+06	1.15E+09	1.09E+09	-1.27E+08
V_f = 0.4	1.05E+09	9.84E+08	-1.15E+08	-4.50E+07	-3.81E+07	4.88E+06	1.00E+09	9.46E+08	-1.10E+08
V_f = 0.5	9.22E+08	8.55E+08	-1.01E+08	-4.50E+07	-3.81E+07	4.88E+06	8.77E+08	8.17E+08	-9.65E+07
% Change	**22.79%**	**24.19%**	**23.01%**	**0.00%**	**0.00%**	**0.00%**	**23.68%**	**25.04%**	**23.90%**

Note: Units of Stress are Pa.

As is illustrated by these tables, the variation in stress as volume fraction was increased from 0.3 to 0.5 is not negligible. Also, one sees that the variation had an effect on the stress in the insulation layers even though they had the same properties in all three cases. The reason for this is that since the loads were constant, increasing the fiber volume fraction caused an increase in the load in the composite layer; the insulation must therefore experience a decrease in load so that the total stress is the same in the whole laminate. As can be seen in Table 5.5, increasing fiber volume fraction did lead to increases in stress in the composite; however, the thermal loading produced more than an order of magnitude more variation than the pressure load. Also, it is observed that in the composite layers the shear stresses were more than two orders of magnitude smaller than σ_x and σ_y shown in Table 5.5. This is attributed to the fact that the copper wires in the composite layer are oriented in the hoop direction; hence, lower shear stress is expected. In the insulation layers, the differences in the three stress components (σ_x, σ_y, and τ_{xy}) are much more uniform to within 20% of each other. As mentioned earlier, the glass fiber orientation in the wrapped insulation tape is about 18° from the hoop direction.

5.2 Finite Element Analysis

5.2.1 Magnetic Stress for Square Conductor

The stress experienced by the composite is caused by the magnetic field that is created when current runs through the continuous copper wires embedded in the cyanate ester resin. Since the load due to a magnetic field is quite complicated to analyze, COMSOL finite element analysis was used. Standard inputs typical of fusion reactors were used for this portion of the analysis, and these are the same numbers shown in Table 5.4. When the material properties are varied, the values in Table 5.3 are used. First, the magnetic field itself had to be created with the software, and then the forces resultant from this field were found using a structural mechanics package as outlined in previous sections. The magnetic field plot is shown in Figure 5.22 below. When analyzing the magnetic stresses in a solenoid,

one very important parameter to look at is the *magnetic flux density* [33]. The magnetic flux density is the measure of the "flow" of magnetic field through a unit surface area and carries the unit Tesla (T), where $1\,T = 1\,\frac{N}{A \cdot m}$ [23]. A plot of this magnetic flux density is shown in Figure 5.23. As can be seen in the figure, the maximum flux density experienced by the system is 0.442 T. Another interesting plot to include is the magnetic field lines generated by the current in the coil. The overall field is again shown in Figure 5.24. This field is composed of an *r*-component and a *z*-component that together make up the total field. These components are shown in Figures 5.25 and 5.26, respectively. When both of these fields are combined using superposition, the field in Figure 5.24 is produced. It is also of note that Figures 5.22 and 5.24 are of the same quantity, except that 5.22 is a surface plot of the magnetic field, while Figures 5.24 through 5.26 are contour plots of the field lines.

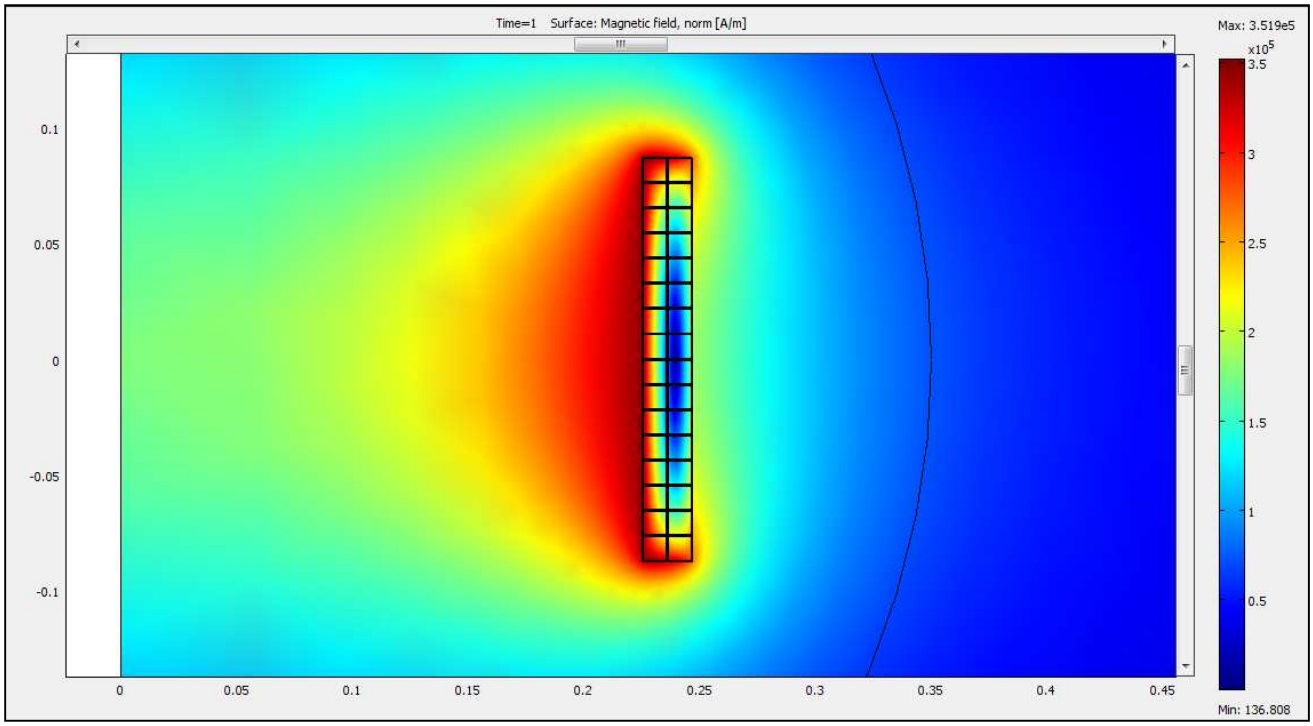


Figure 5.22 Surface Magnetic Field. The magnetic field is strongest at the inside edges of the coil with a magnitude of $3.519 \times 10^5\ \frac{A}{m}$.

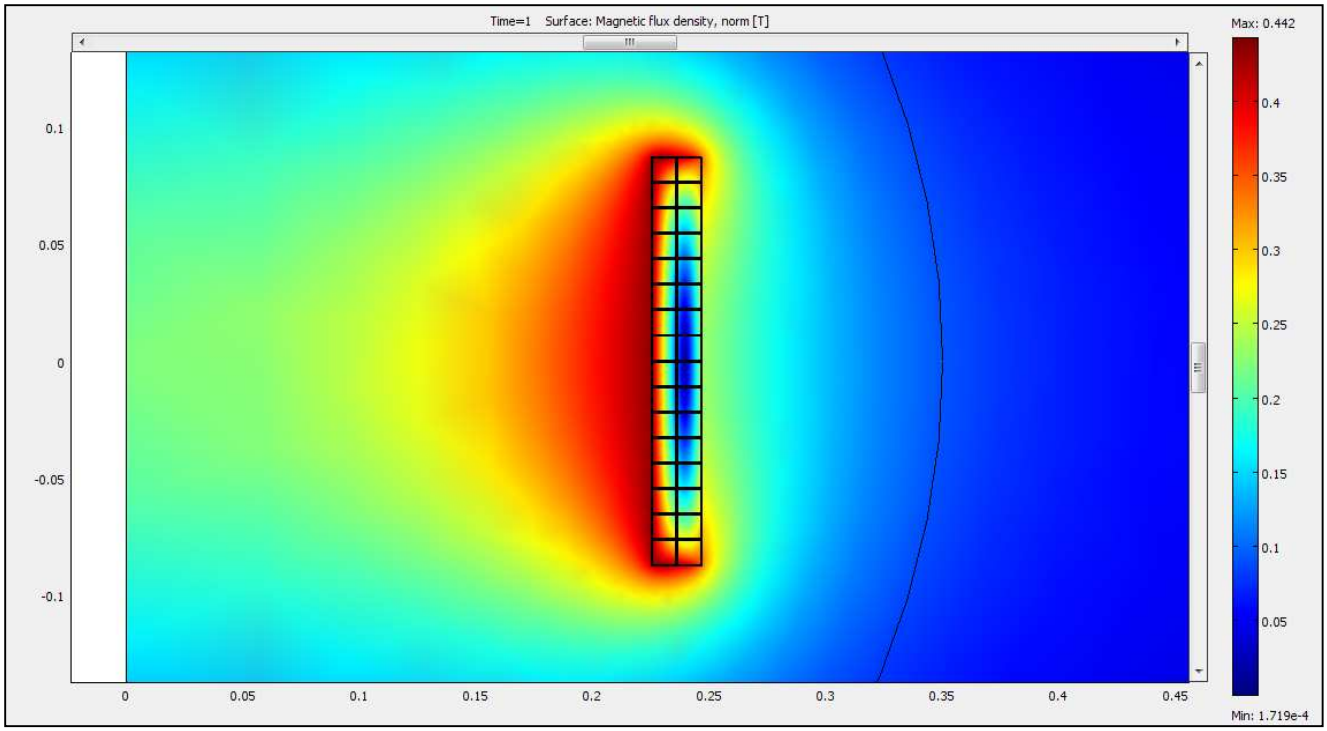


Figure 5.23 Surface Magnetic Flux Density. Magnetic flux density and magnetic field are the same except magnetic flux density is in Tesla. Maximum magnetic flux density is 0.442 T.

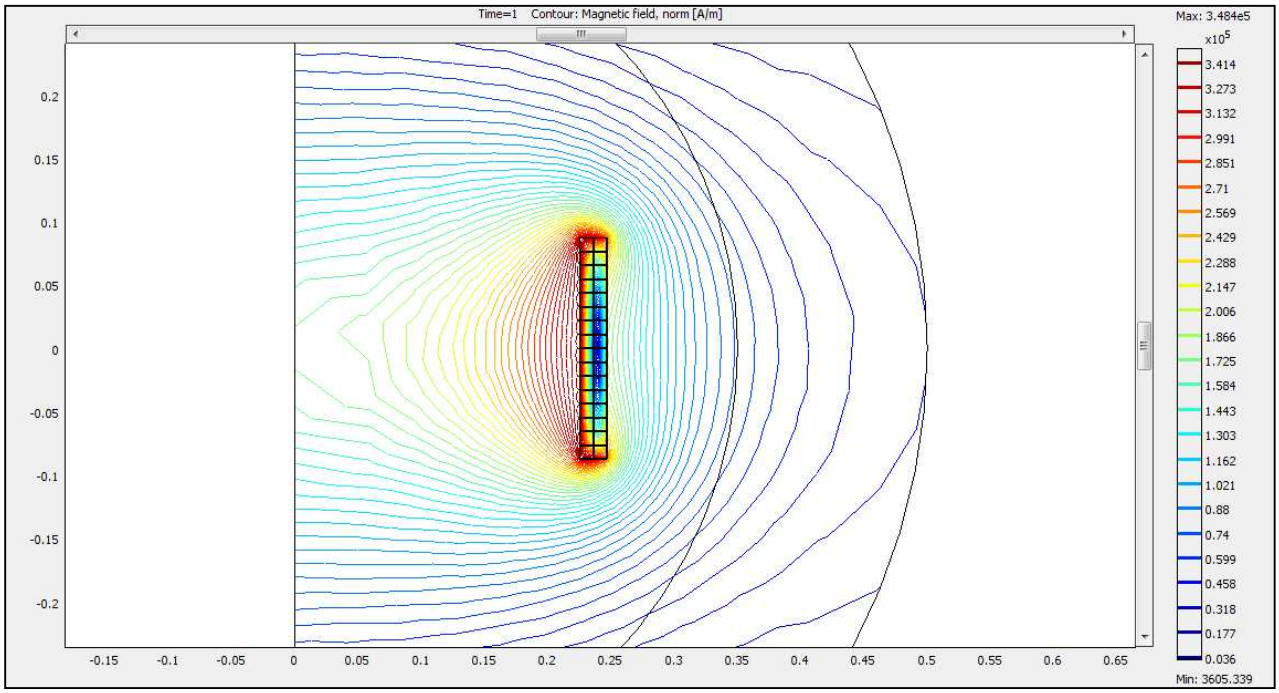


Figure 5.24 Magnetic Field Lines. Though the strength is weak for from the coil, the field lines extend beyond the boundaries of the model.

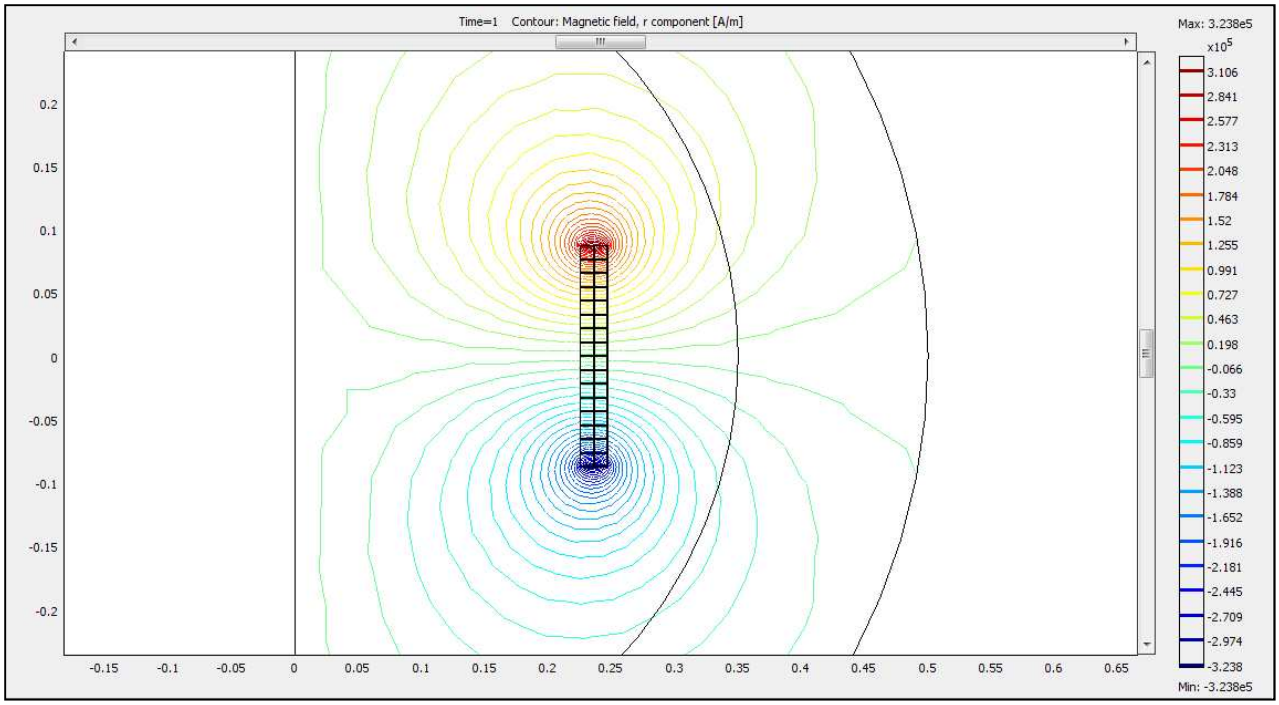


Figure 5.25 Magnetic Field Lines, *r* Component. This is one component of the normalized magnetic field.

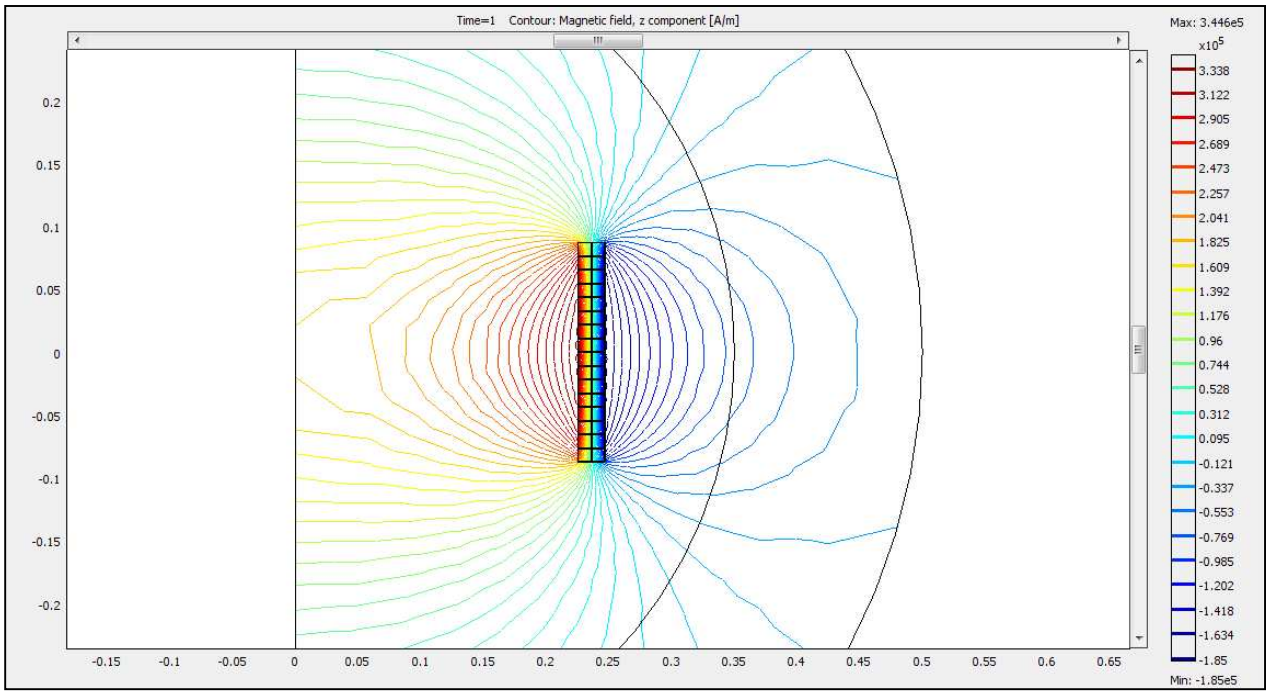


Figure 5.26 Magnetic Field Lines, *z* Component. This is one component of the normalized magnetic field.

Now that the magnetic field has been established, its effects on the material such as strain, stress, and displacement are next explored. The previous magnetic field and flux plots will be the same for all of the fiber volume fractions because the magnetic properties are independent of V_f. However, the following table, Table 5.7, is a summary of how the fiber volume fraction affected the stress. The numbers in the table are derived from the finite element analysis. Stress in the *r*-direction, denoted as σ_r, is illustrated in Figures 5.27 through 5.29. Stress is higher at the ends and the highest stresses are localized to the corners of the composite and the insulations layers experience a compressive stress. Stress in the *z*-direction (σ_z) is shown below in Figures 5.30 through 5.32. The trend here is similar to the *r*-direction, as the stress is tensile at the ends and compressive in the center. However, the *z*-direction stresses are much more compressive and the max tensile load is at the inner bottom corner of the fixed end of the coil. The hoop direction stresses, σ_φ, are shown in Figures 5.33 and 5.34. These stresses are much more uniform through the coil and are all tensile, with the composite having a larger stress than the insulation layers. It would be expected for all these stresses to be tensile as opposite sides of the coil will all have a repulsive force on them as discussed previously in Section 3.4. Shear stresses τ_{rz} are illustrated in Figures 5.35 through 5.37. This is also a complicated loading where the composite layers have higher stresses than the insulation does. This also is a very good example of how the corners and edges of contact between the insulation and composite have stress concentrators where high stresses are formed at these boundaries, as seen especially in Figure 5.37. Finally, the displacement that the coil experiences as a result of the magnetic loading is shown in Figures 5.38 through 5.40. Figures 5.38 and 5.39 show the *r*- and *z*-direction displacements (respectively) experienced by the geometry, while Figure 5.40 is the superposition of these into the total displacement. The displacement experienced is very small, and although it is uniform in the *z*-direction, the *r*-direction displacement is not uniform and displaces more in the center. The displacement in the *r*-direction is all positive, while as expected the *z*-displacement is negative due to the compressive forces. The deformed shape of the coil would no

longer be uniform but rather twisted which is what gives rise to the shear stresses seen by the coil. From looking at Figure 5.38 it can be seen that the center of the coil will expand outward causing it to take on a “bulging” shape. As mentioned before, a summary of the stresses is shown in Table 5.7 as well as a comparison for several fiber volume fractions.

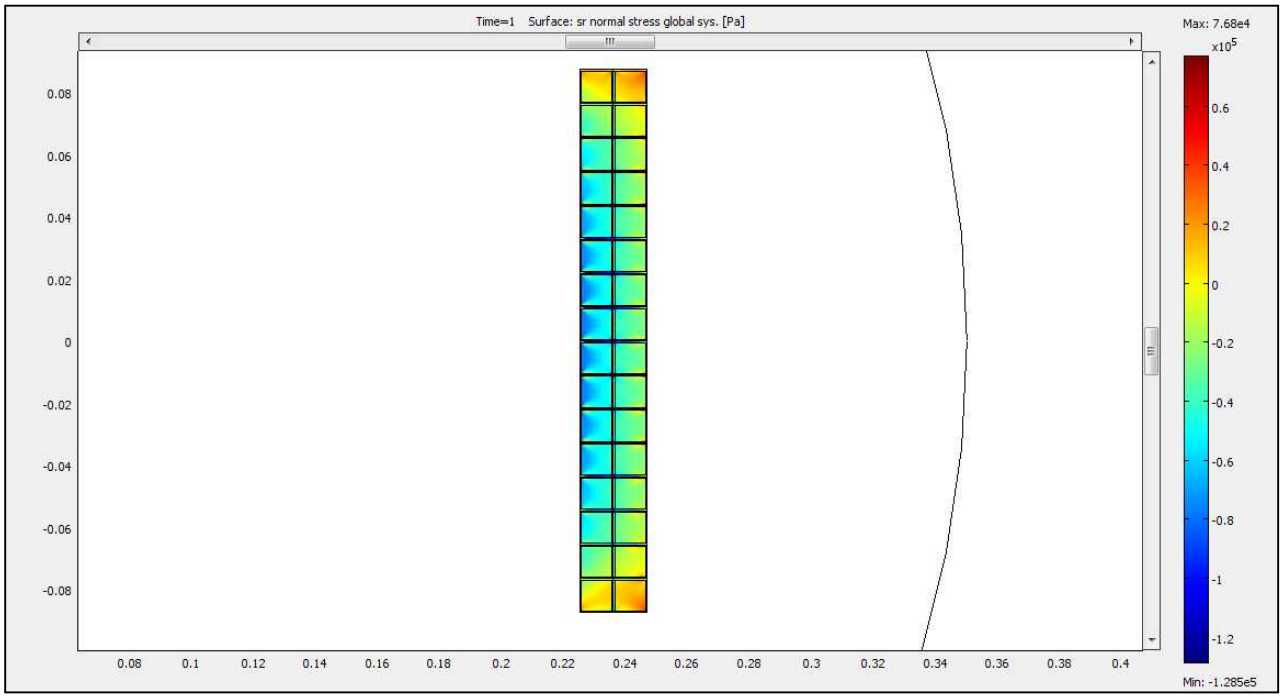


Figure 5.27 Stress in the *r* direction σ_r. Stress is maximum at interior insulation and at corners and edges.

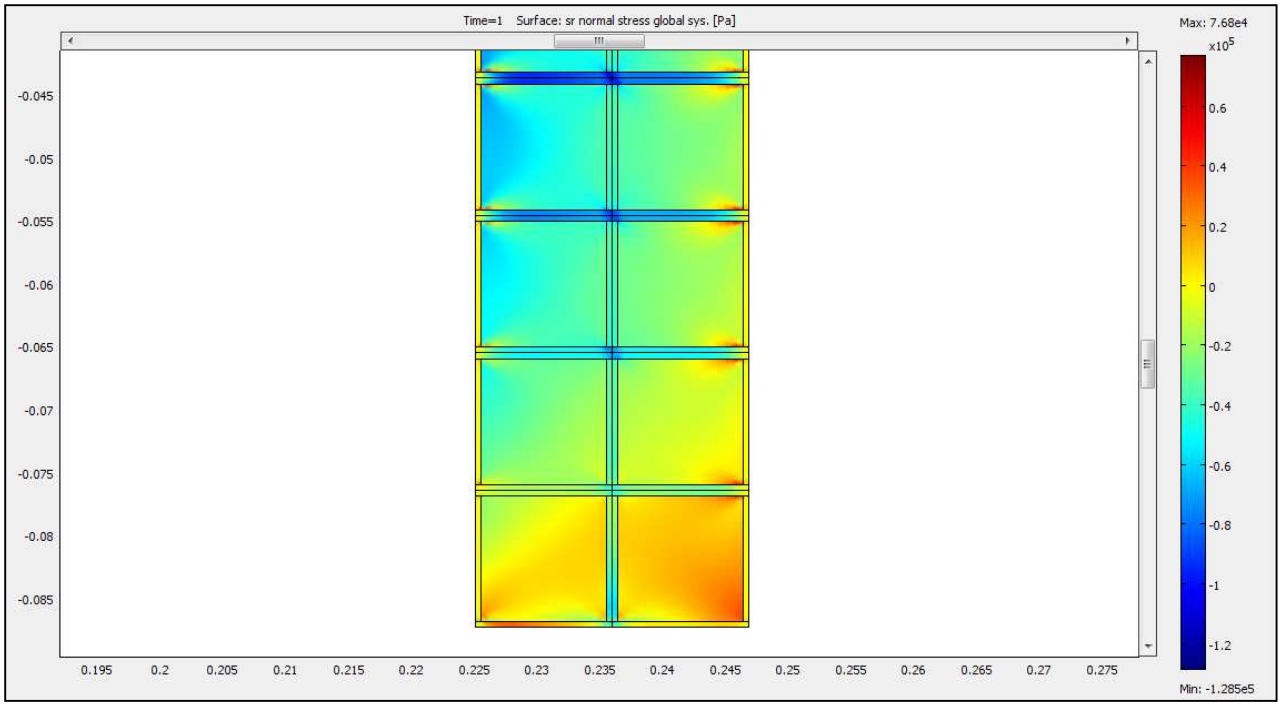


Figure 5.28 Close-up of the End of the Coil for Stress σ_r. Stress is maximum at interior insulation and at corners and edges.

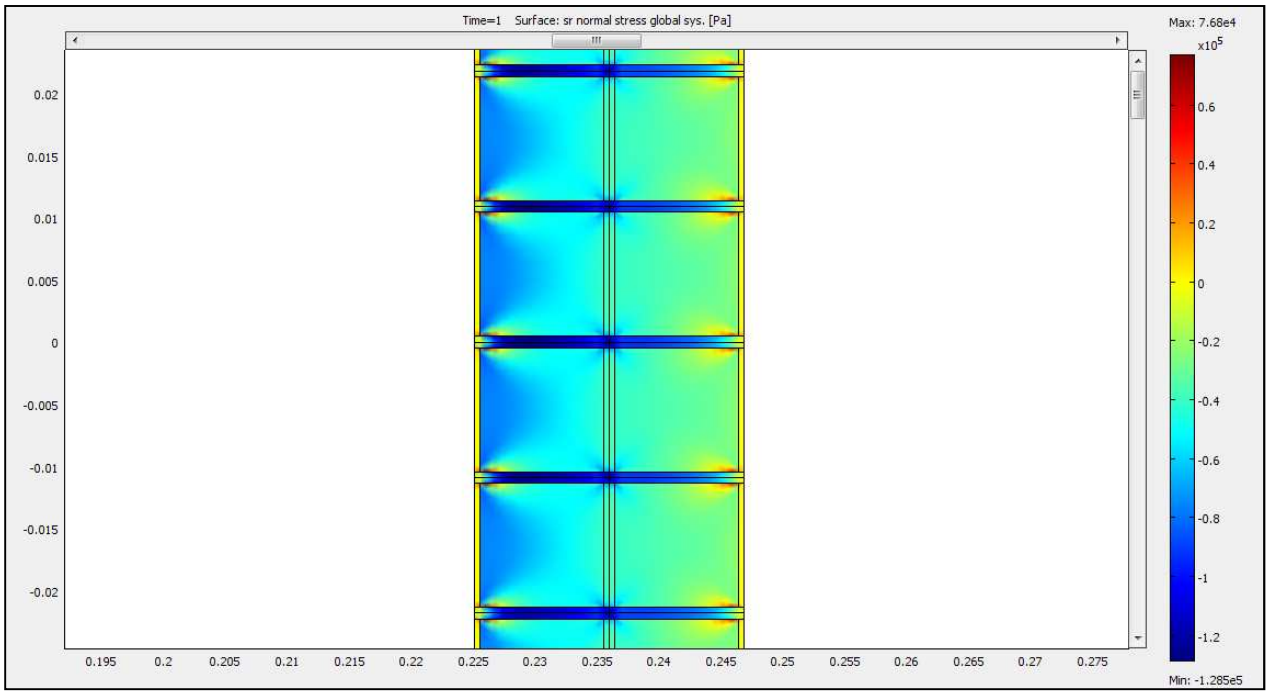


Figure 5.29 Close-up of the Center of the Coil for Stress σ_r. Stress is maximum at interior insulation and at corners and edges.

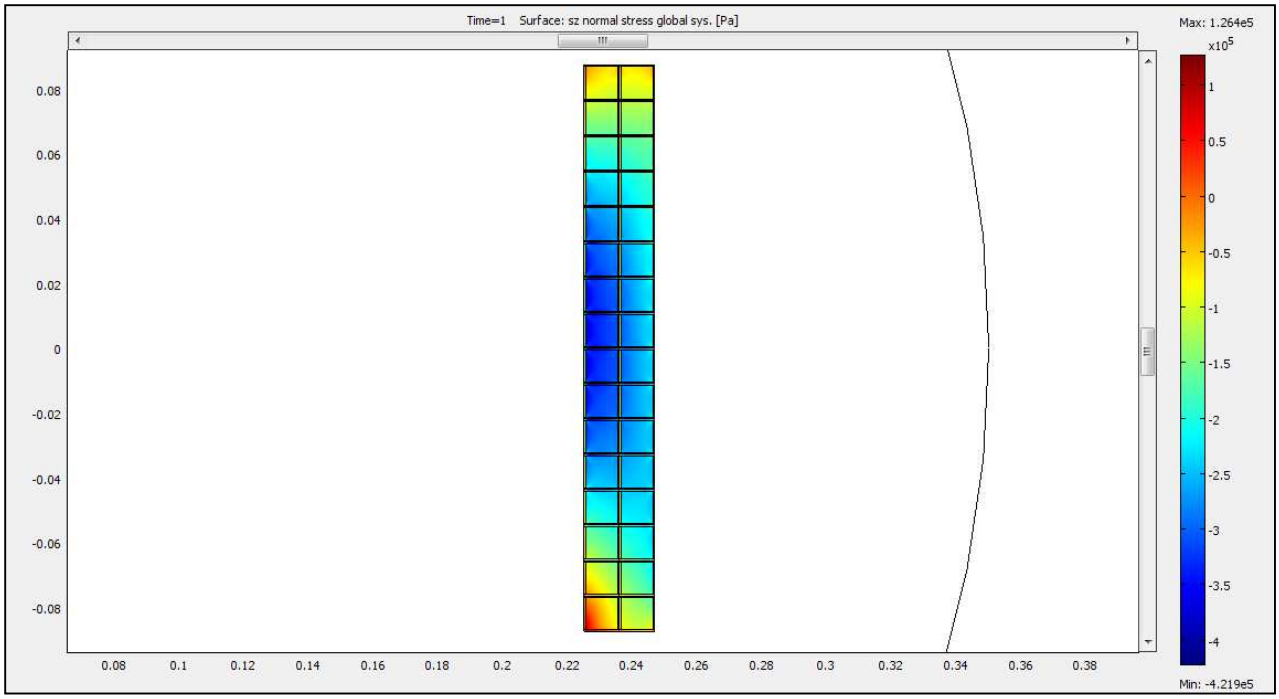


Figure 5.30 Stress in the *z* direction σ_z. Stress is maximum at the bottom inner corner and the inner center of the coil.

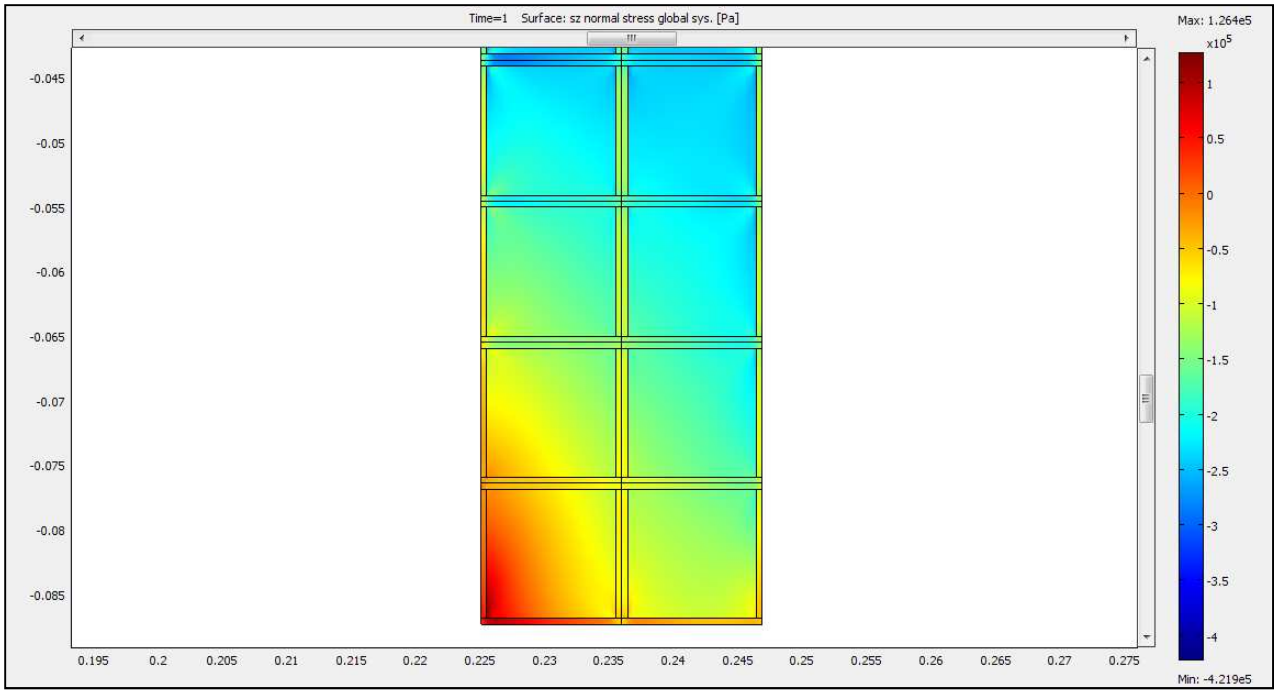


Figure 5.31 Close-up of the End of the Coil for Stress σ_z. Stress is maximum at the bottom inner corner and the inner center of the coil.

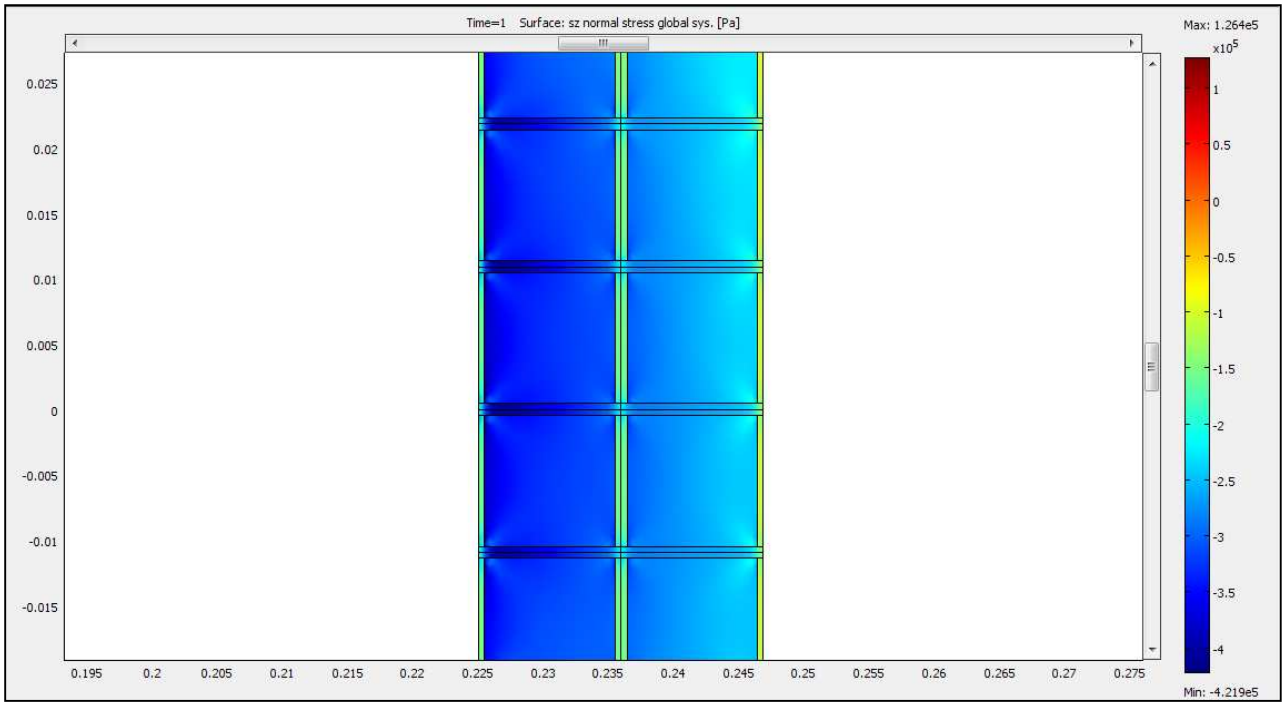


Figure 5.32 Close-up of the Center of the Coil for Stress σ_z. Stress is maximum at the bottom inner corner and the inner center of the coil.

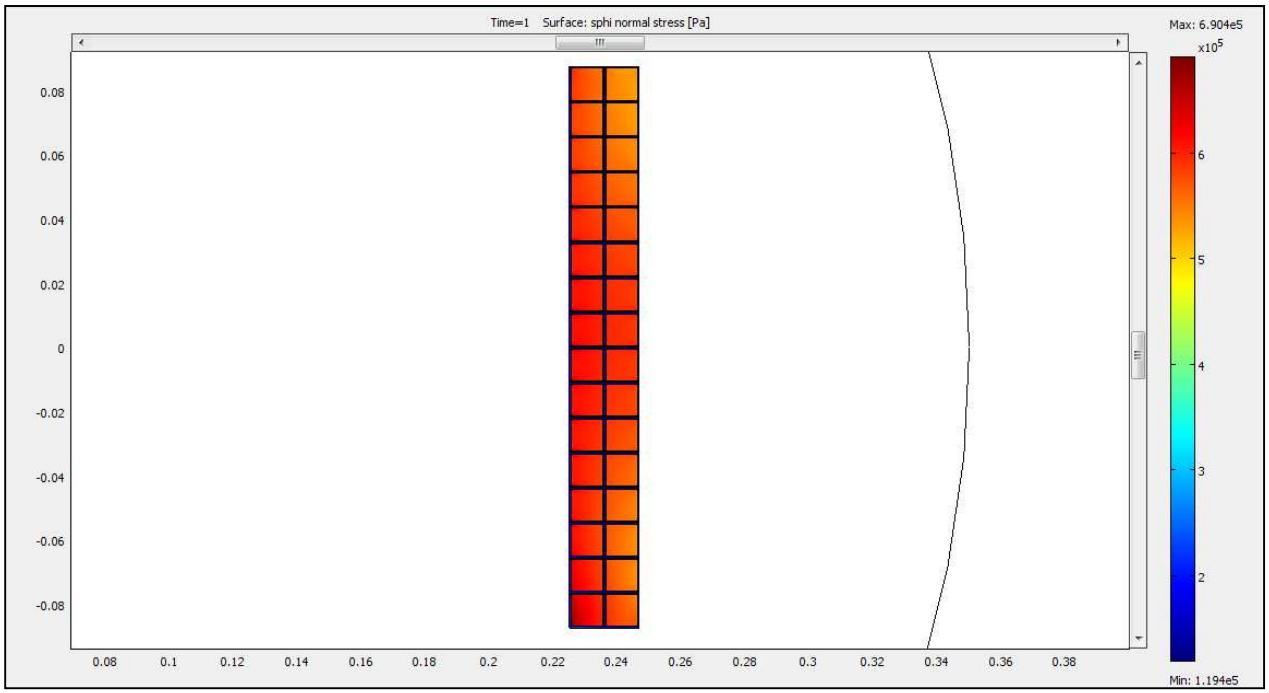


Figure 5.33 Stress in the φ direction σ_φ. Stress is uniform in the composite turns, and in the insulation layers.

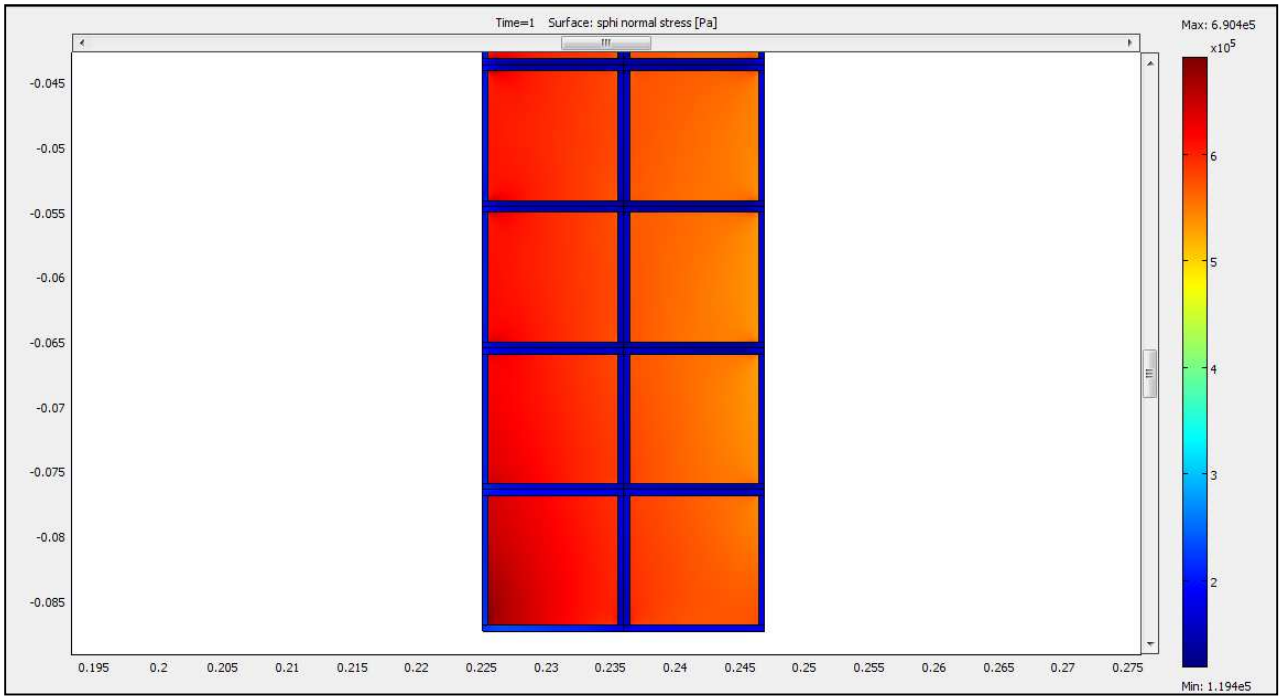


Figure 5.34 Close-up of the Coil for Stress σ_{φ}. Stress is uniform in the composite turns, and in the insulation layers.

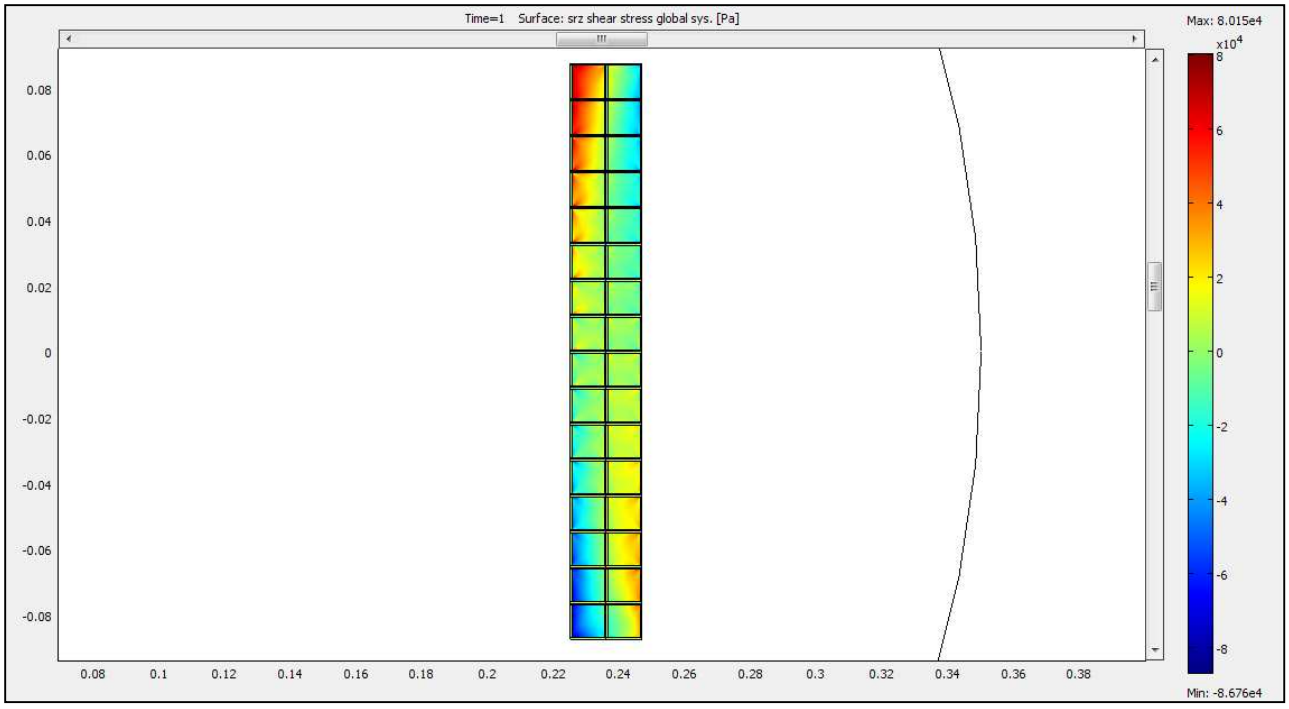


Figure 5.35 Shear Stress τ_{rz}. Shear stress has large stress concentrations in corners and at boundaries of composite and insulation layers.

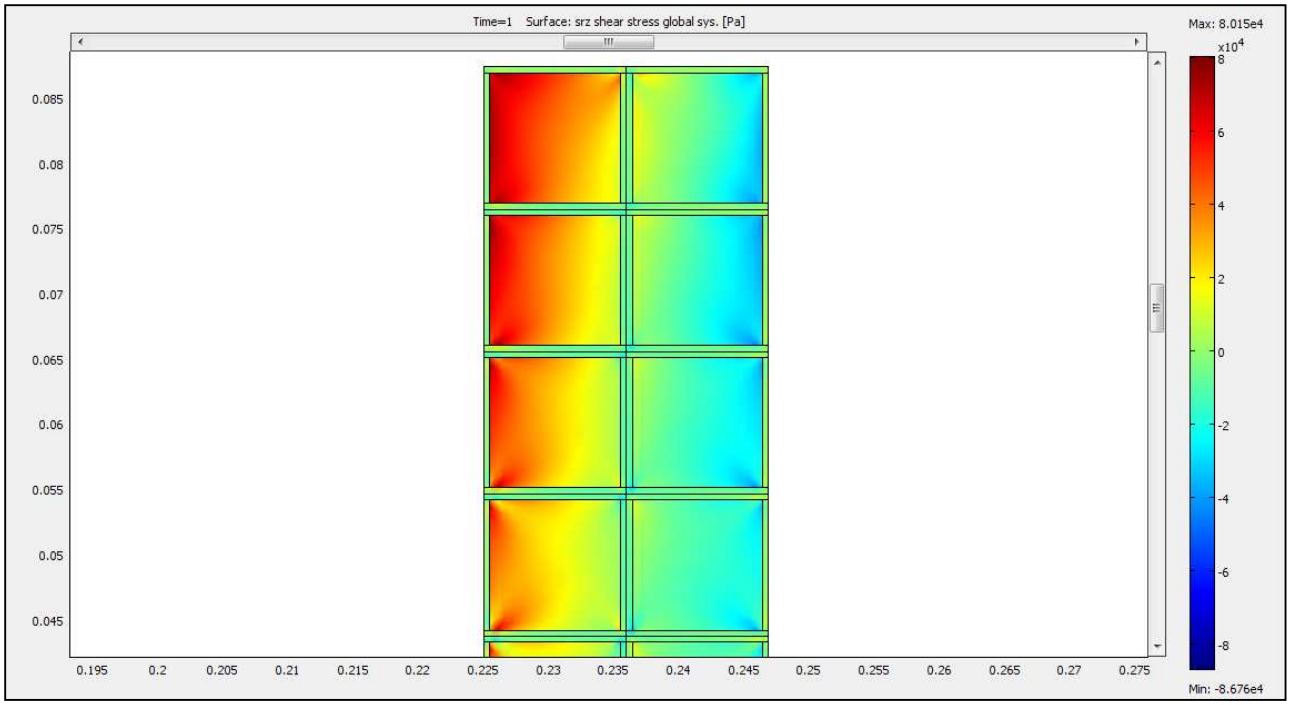


Figure 5.36 Close-up of the End of the Coil for Stress τ_{rz}. Shear stress has large stress concentrations in corners and at boundaries of composite and insulation layers.

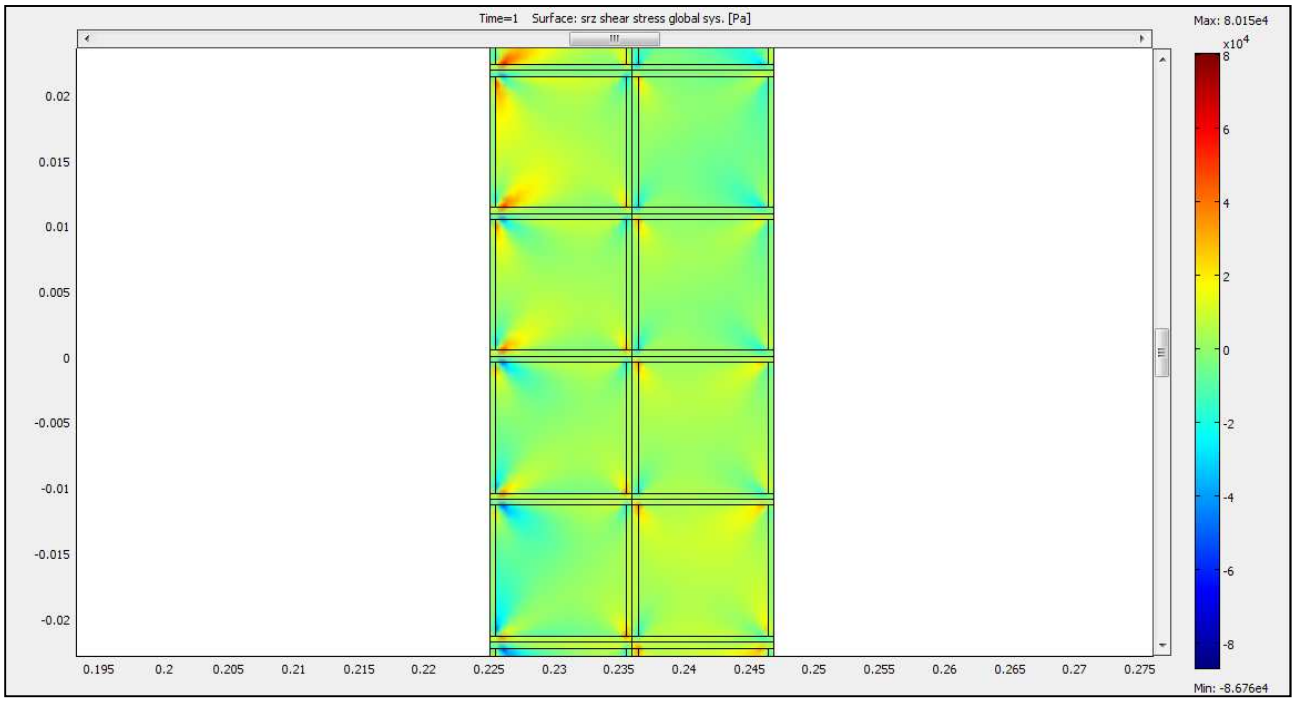


Figure 5.37 Close-up of the Center of the Coil for Stress τ_{rz}. Shear stress has large stress concentrations in corners and at boundaries of composite and insulation layers.

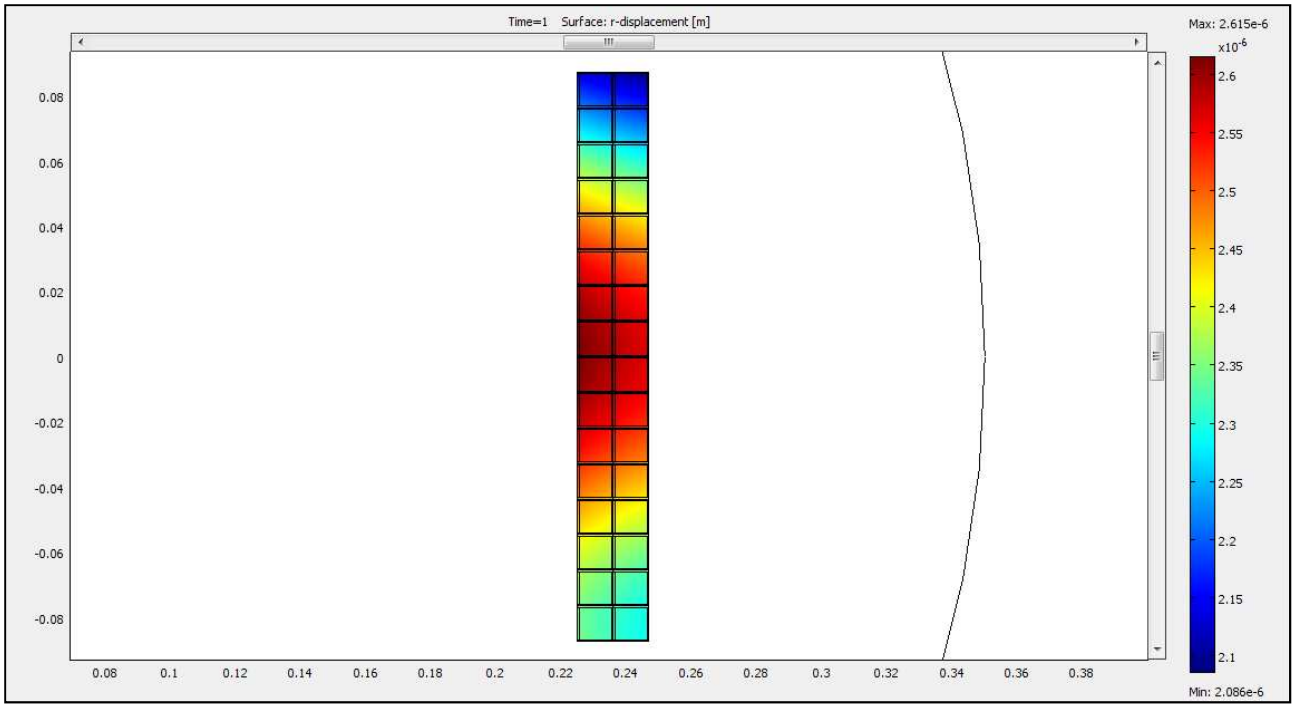


Figure 5.38 *r* direction Displacement d_r. Displacement is maximum at the center, causing a "bulging" to occur in the center of the coil.

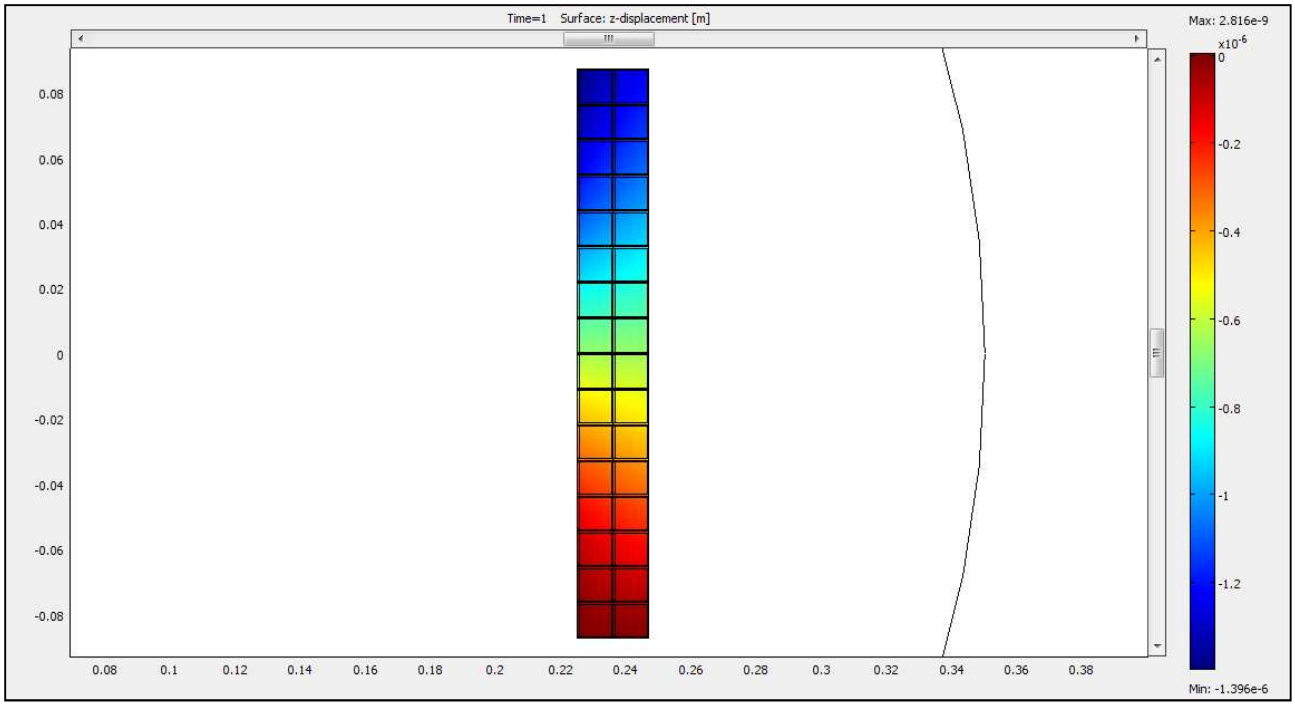


Figure 5.39 *z* direction Displacement d_z. Displacement is maximum at the free end and zero at the fixed end.

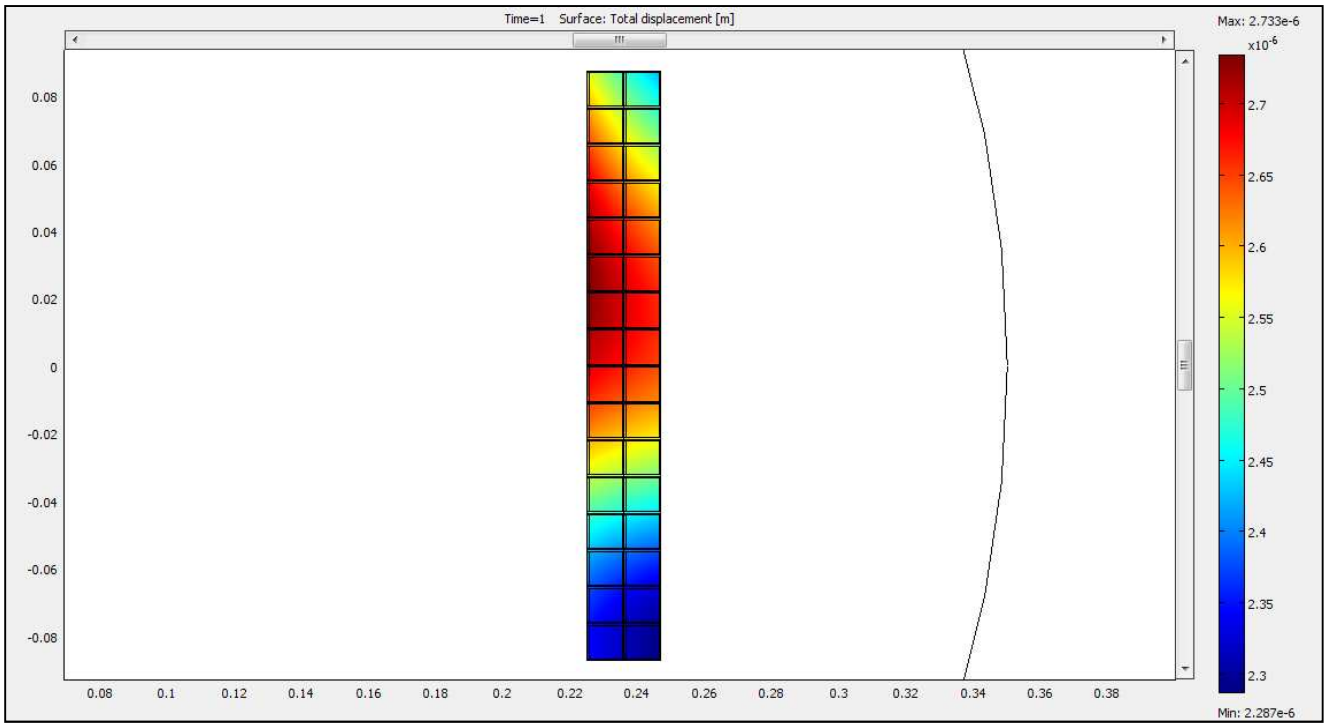


Figure 5.40 Total Displacement d_{tot}. This is a superposition of displacement in both directions.

Table 5.7 Maximum Stresses and Displacement for Several Volume Fractions.

Volume Fraction	Stress σ_r	Stress σ_z	Stress σ_φ	Stress τ_{rz}	Displ. d_r	Displ. d_z	Total Displ. d_t
V_f = 0.3	-1.28E+05	-4.22E+05	6.90E+05	-8.68E+04	2.62E-06	-1.40E-06	2.73E-06
V_f = 0.4	-1.34E+05	-4.35E+05	7.01E+05	-8.68E+04	2.35E-06	-1.30E+06	2.46E+06
V_f = 0.5	-1.38E+05	-4.49E+05	7.12E+05	-8.68E+04	2.13E-06	-1.21E-06	2.24E-06
% Change	**7.42%**	**6.45%**	**3.09%**	**0.03%**	**-18.62%**	**-13.54%**	**-18.04%**

Note: Units of Stress are Pa.

The summary of the magnetic stress analysis is shown above in Table 5.7. In general the Results are that increasing volume fraction has less of an effect on magnetic stresses than it does on thermal and mechanical stresses. Displacement is by far the most strongly affected quantity, with radial displacement decreased over 18% and axial displacement decreased over 13%. This is expected because as the composite stiffens with the addition of more wires, its displacement will be more constrained. This change in displacement translates into a smaller change in stress seen by the coil. Stress in the *r*-direction is most affected at over 7%, and axial stress is similar at almost 6.5%. Hoop stress in the fiber direction has less than half as much of an effect, and most surprisingly shear stress varies negligibly as the fiber volume fraction is increased. Again, shear stress is smaller than the other stress components so it is not as important a factor in the failure of the coil, but it is still surprising that it basically doesn't vary with fiber volume fraction.

5.2.2. Magnetic Stress for Rounded Conductor

This section of the analysis was performed solely to test out how much of an effect rounding off the edges of the magnetic model would have on the stresses experienced by the coil. This was done because the actual coil will, in practice, have rounded edges, and to investigate just how much of an effect that the corners have on stress in the cylinder. The magnetic field generated was not exactly the same because the geometry was altered, but it was very similar. The peak magnetic flux experienced was found to be 0.439 T for the rounded edged model, and when compared to 0.442 T for the square model, it is basically the same. The stresses were found to be a bit different, however. Figure 5.41 shows stress in the *r*-direction of the rounded coil. Stress distribution is very similar to Figure 5.29 in the conductor and insulation; however, in the insulation transition from rounded to square, a stress concentration can still be seen. Surprisingly, the magnitude of stress actually went up at the transition point so the rounded edged model has higher stresses at the critical points than the previous model did.

The plot of stress in the *z*-direction is shown in Figure 5.42 below. Although the original model didn't have very much stress concentration effect for σ_z, Figure 5.42 shows that the new rounded model does have a significant stress concentration at the same points as in Figure 5.41. Even hoop stress now experiences a stress concentration that wasn't previously there as illustrated in Figure 5.43. The final stress is shear stress in the coil, and it is shown below in Figure 5.44. It can be seen that this stress was also magnified by rounding the conductors and insulation. These results are surprising and show that stress concentration actually increased when the edges were removed. The most likely explanation for this is that the stress is a result of the meeting of the two materials at a point and not because of the corners. A final test was performed where the insulation layers surrounding the composite were completely joined to eliminate any corners in the model. This is shown in Figure 5.45. The results are very convincing, as the stress was not altered at all by this modification.

Of note is the fact that when the insulation is modified to have rounded corners, the material properties are no longer completely correct. Since the insulation is an orthotropic material, the fiber direction will slowly change as the insulation travels around the radius. It is possible to make this more accurate in the FEA software, but this is very difficult and was believed to be beyond the scope of this exercise. In any case the effect of having incorrect material properties around the radius is probably not significant and the goal of finding if stress concentration was a factor was still obtained.

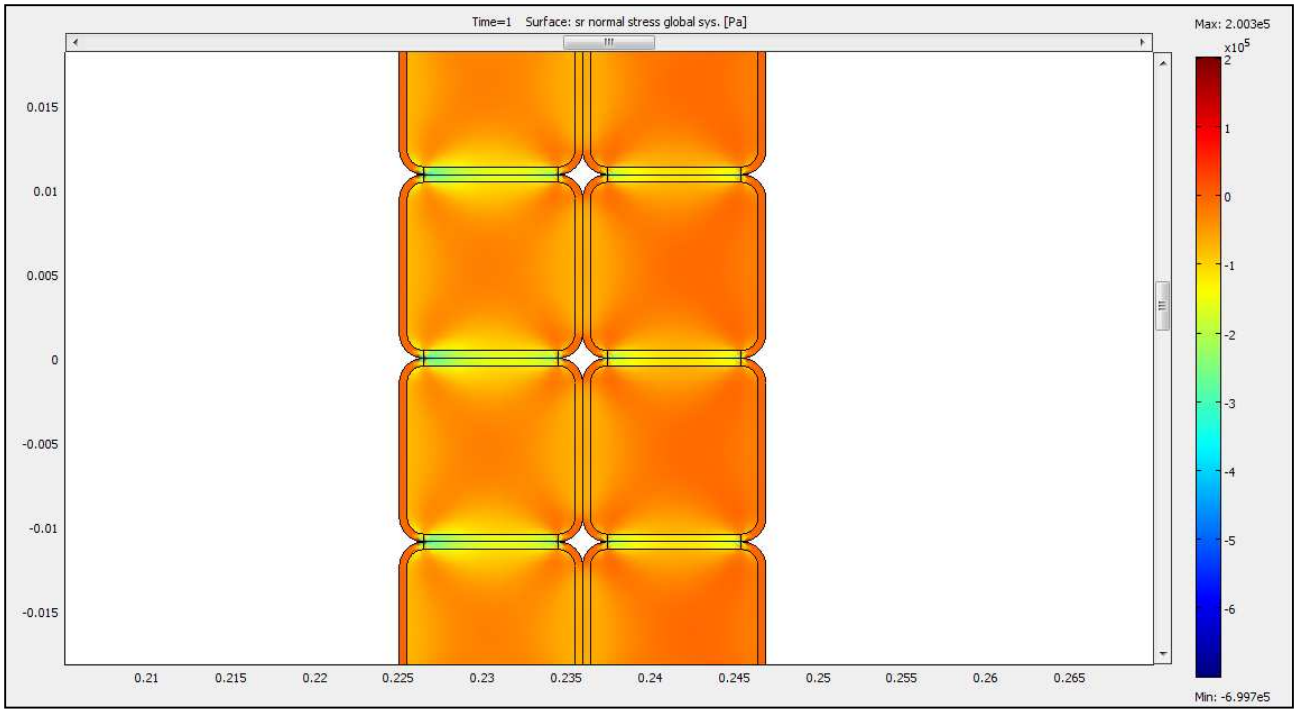


Figure 5.41 Stress in the *r* direction σ_r for Rounded Edges. Stress concentration still occurs at the intersection of adjacent insulation layers.

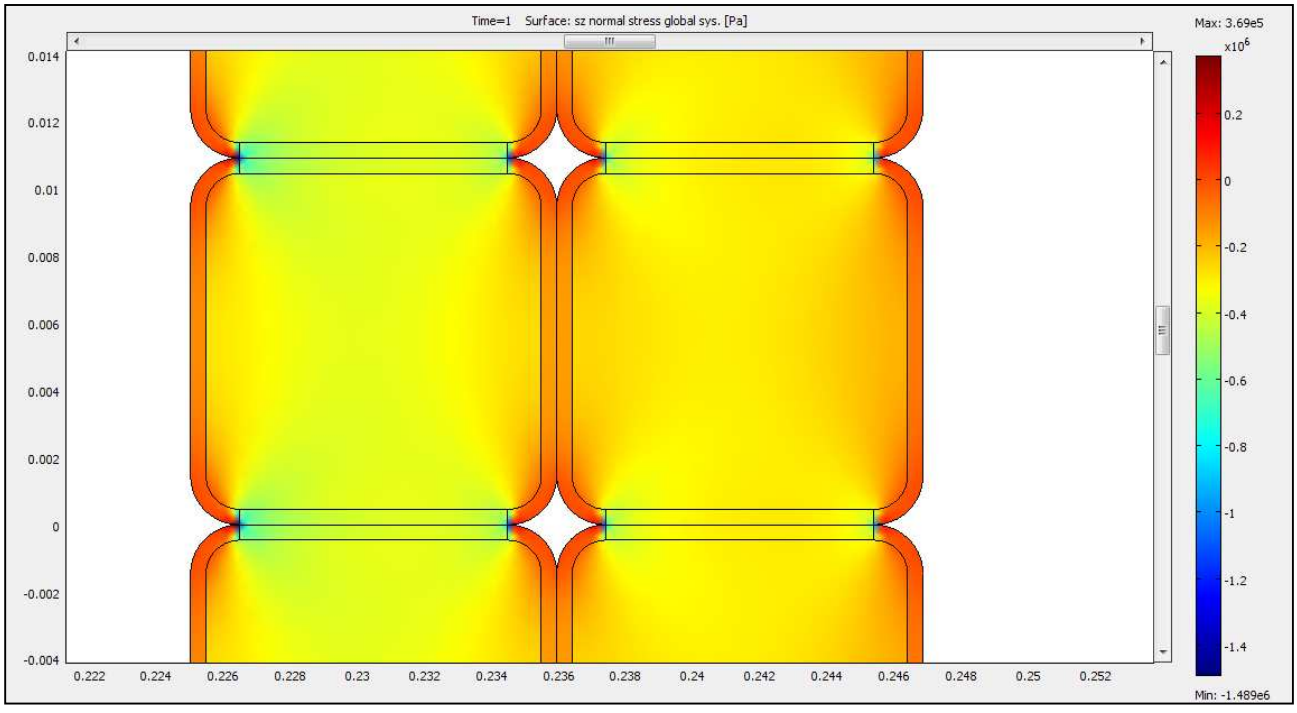


Figure 5.42 Stress in the *z* direction σ_z for Rounded Edges. Stress concentration still occurs at the intersection of adjacent insulation layers.

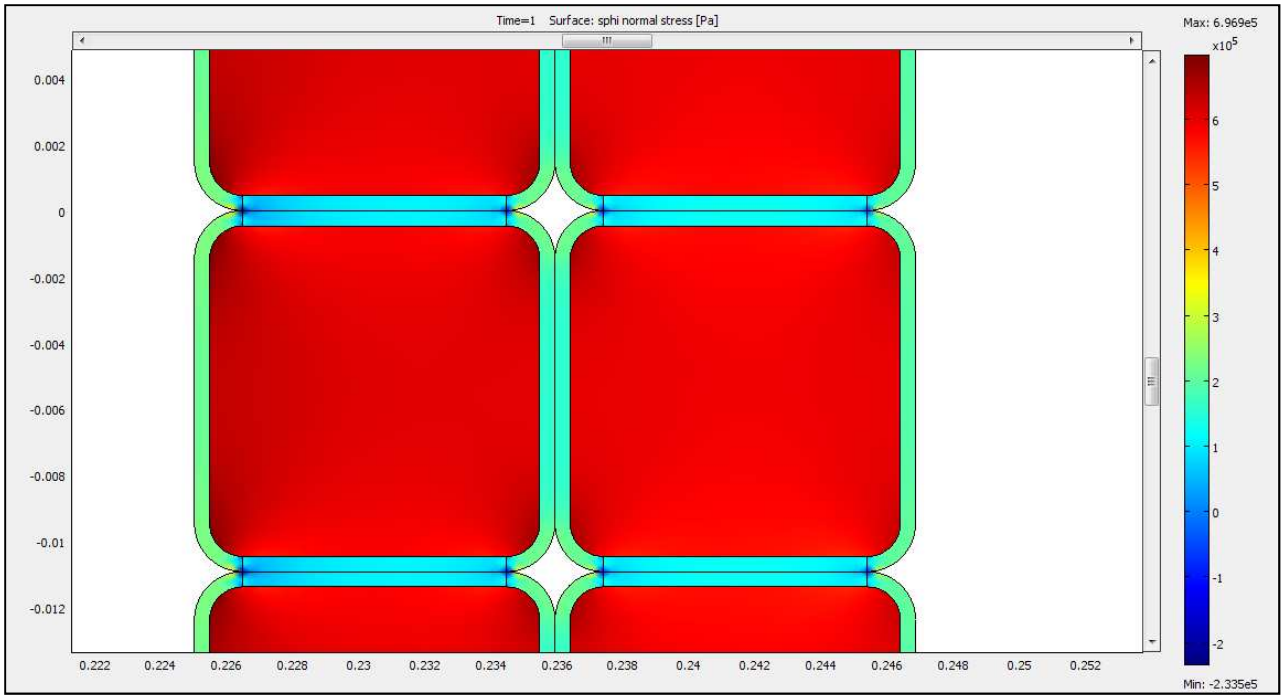


Figure 5.43 Stress in the φ direction σ_{φ} for Rounded Edges. Stress concentration still occurs at the intersection of adjacent insulation layers.

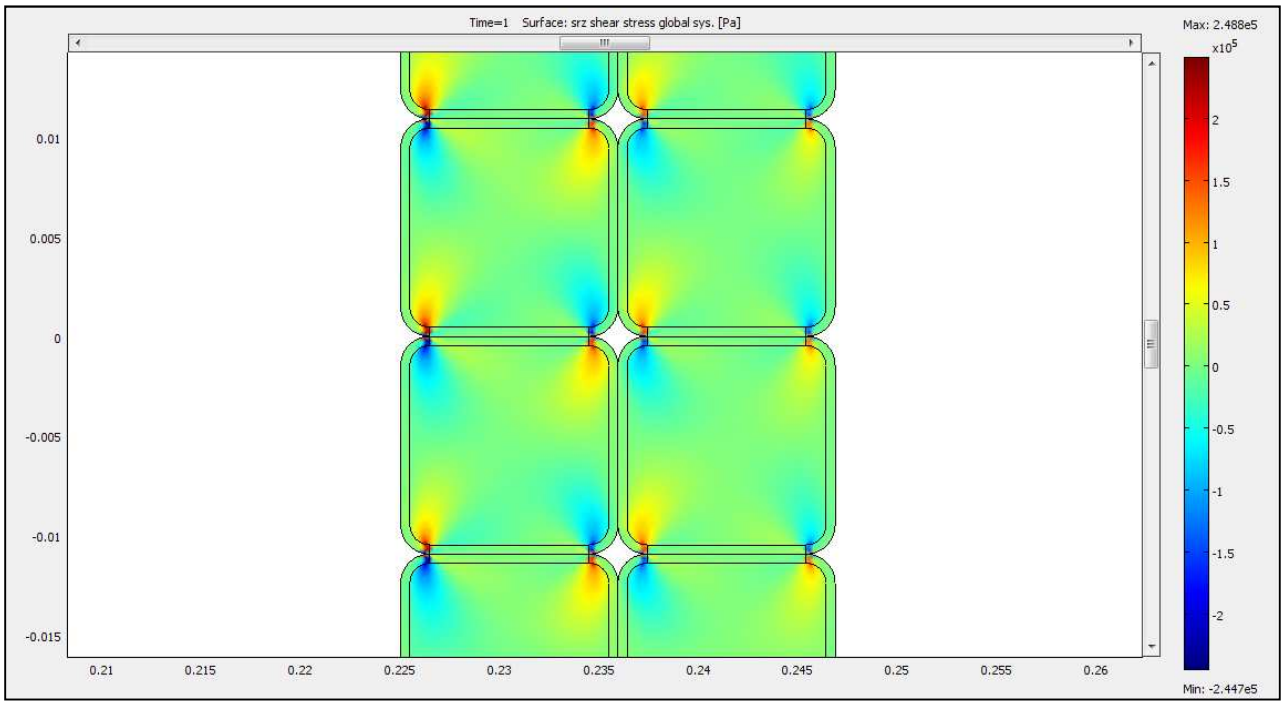


Figure 5.44 Shear Stress τ_{rz} for Rounded Edges. Stress concentration still occurs at the intersection of adjacent insulation layers.

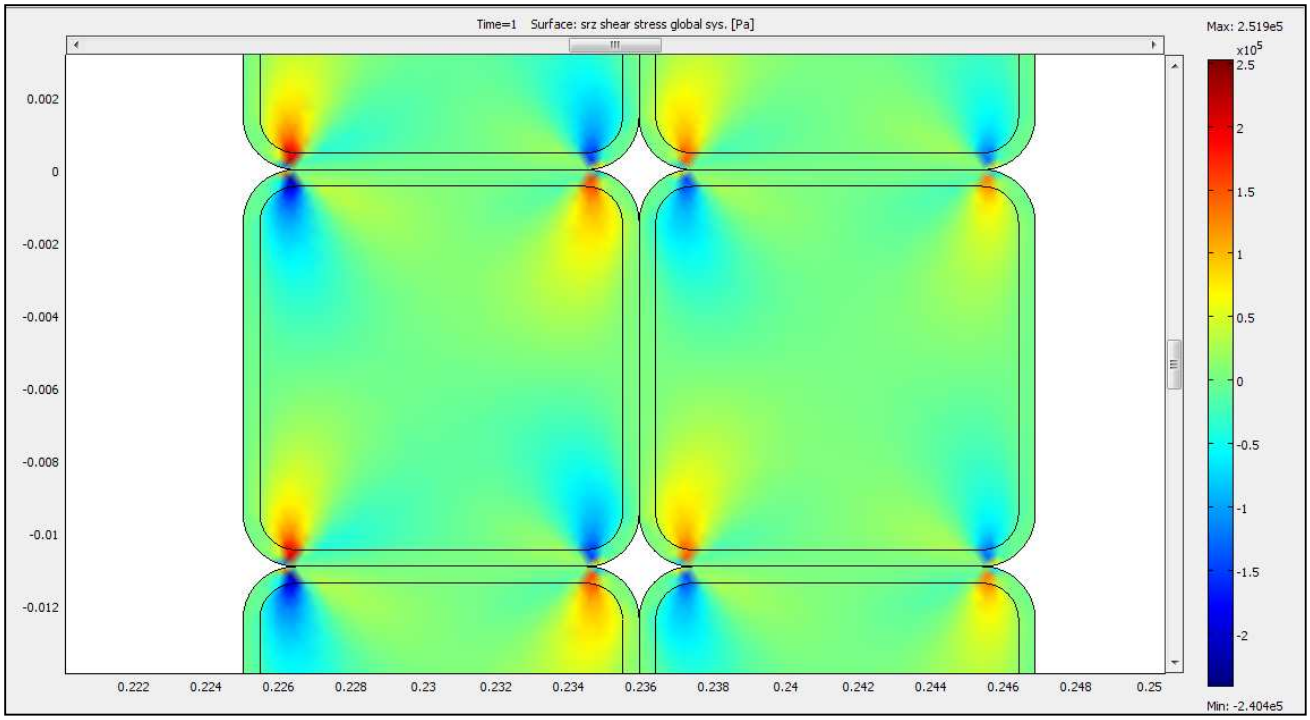


Figure 5.45 Stress with Insulation Boundary Removed. Stress concentration still occurs at the intersection of adjacent insulation layers.

5.2.3 Thermal Stress and Mechanical Stress

The final portion of the finite element analysis was to develop a test coil that would model the thermal and mechanical stresses that were previously found using MATLAB. This model was actually a 3D representation, but it wasn't a complete coil but rather just a portion of it. As in the mathematical model, three types of loads were tested: thermal, mechanical, and a combined load. The same magnitudes of loadings as the MATLAB portion were used. Figure 5.46 shows the stress in the *X*-direction while Figure 5.47 is of stress in the Y-direction, both for a thermal load of ΔT = 150K. Similarly to the previous findings, the stress is constant in the composite layers and in the insulation layers, lending some credibility to the assumptions made in the mathematical model. A summary of the results is shown in Table 5.8 below.

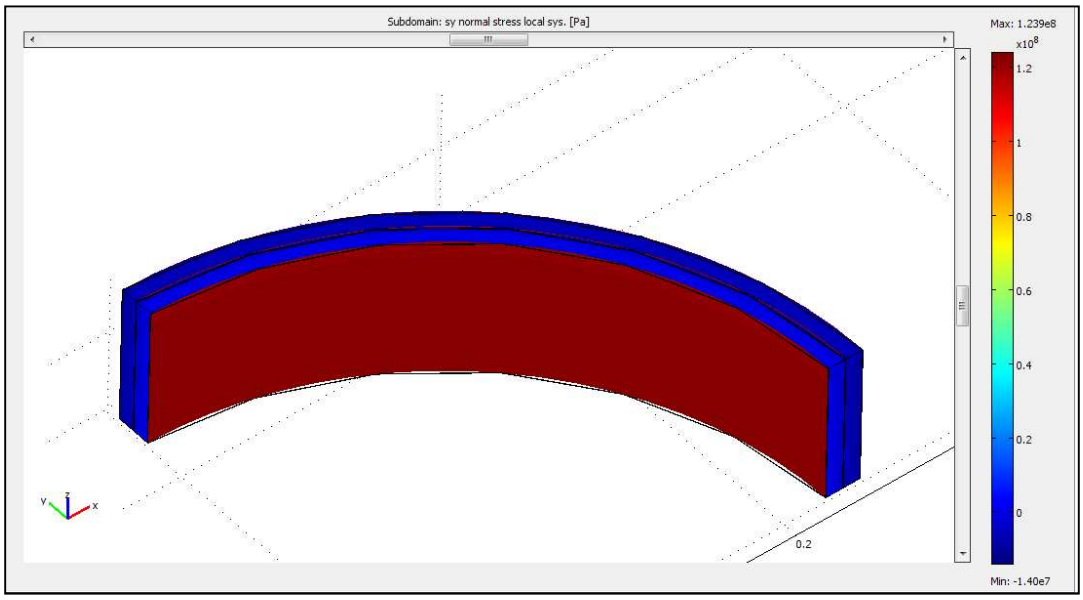


Figure 5.46 Thermal Stress in the *X* Direction. Stress is uniform in composite layers and in the insulation layers.

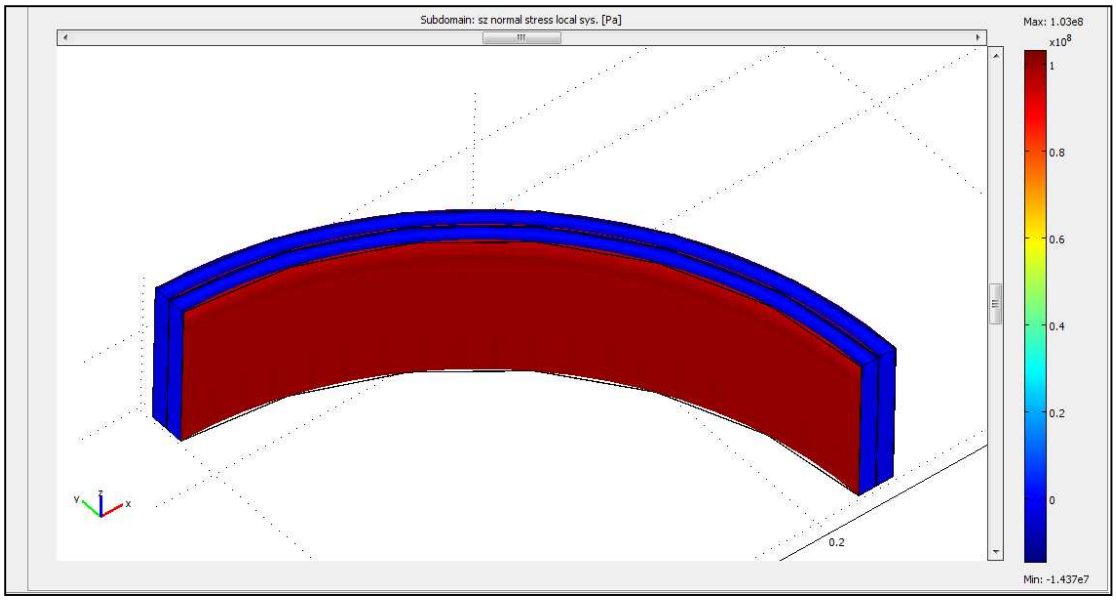


Figure 5.47 Thermal Stress in the *Y* Direction. Stress is uniform in composite layers and in the insulation layers.

Table 5.8 Summary of Thermal and Pressure Finite Element Analysis.

Volume Fraction	Pressure		Temperature		Combined	
	Stress σ_x	Stress σ_y	Stress σ_x	Stress σ_y	Stress σ_x	Stress σ_y
$V_f = 0.3$	2.34E+09	6.56E+07	-1.47E+07	-1.82E+07	2.34E+09	2.59E+07
$V_f = 0.4$	2.34E+09	4.84E+07	-1.45E+07	-1.61E+07	2.35E+09	2.69E+07
$V_f = 0.5$	2.35E+09	3.47E+07	-1.40E+07	-1.44E+07	2.35E+09	2.78E+07
% Change	**0.43%**	**-47.16%**	**-4.44%**	**-21.13%**	**0.34%**	**7.46%**

Note: Units of Stress are Pa.

When comparing the results in Table 5.8 to the previous results shown in Tables 5.5 and 5.6, the results do not look too promising. However, the finite element analysis does give some encouragement that the results of the mathematical modeling are correct. The FEA model had constant stress in its layers. Also, the composite layer thermal stress was negative and the pressure stress was positive, just like in the MATLAB model. The insulation layer was also similar, with a positive stress that was less than the pressure stress and almost opposite of the thermal stress. The magnitudes of stress are very similar for both models, and the pressure stress manifested as being higher than the thermal stress and dominated in the combined loading, just like for the mathematical model. Though another method of verification, such as experimental results, is desired, these results do tend to confirm that the assumptions in the mathematical model are acceptable and that the results, especially the trends hold true.

Chapter VI

CONCLUSIONS AND RECOMMENDATIONS

6.1 Conclusions

Cyanate ester resin was specifically designed to replace epoxy as the bonding or matrix material for copper wires in fusion reactors. Although other areas of application could be used, this was specifically the focus of the material production and testing of this research. In particular, an investigation into the effect that varying the volume fraction of wires in the composite had on the performance of the material was undertaken. This report summarizes and characterizes how one of the most important parameters of fiber reinforced composite materials, the fiber volume fraction, when altered, will cause variation in material properties and in stress and strain in the composite cylinder.

Based on laminate plate theory models and finite element analysis, it was found that varying fiber volume fraction affected both material properties and stresses due to mechanical, thermal, and magnetic loads. This variation was found not just in the composite itself, but also in the stress seen by the insulation material.

The major findings of this thesis are concluded as follows:

(1) Increasing fiber volume fraction for a cyanate ester/copper composite results in increased Young's moduli, shear modulus, and Poisson's ratios. In the target range of V_f = 0.3 to 0.5, the moduli increase almost twice as much as the Poisson's ratios. The moduli increase in magnitude by an average of 24.8% whereas the Poisson's ratios increase by much less, only about 11.7%. The properties were affected in the sequence E_x, E_y, G_{xy}, v_{xy}, and v_{yx} where longitudinal modulus experiences the greatest increase and Poisson's ratio the least. Thermal expansion coefficients

decreased in value as the fiber volume fraction was increased. Both longitudinal and transverse CTE's decreased by an average of 18.8% while shear CTE was only decreased by 5.4%.

(2) Varying the properties of the composite affected the load in all the other components as well. In a multi-layered laminate composed of cyanate ester/copper fiber composite layers with S2 glass cloth insulation in between, the stress in the glass layers as well as the stress in composite layers is altered by changing the fiber volume fraction of the composite.

(3) For a laminate composed of two cyanate ester impregnated copper composite layers with S2 glass insulation between, under pressure, temperature, and combined loading, the effect of varying fiber volume fraction was not uniform. Pressure effect is miniscule, but temperature is altered about 6%.

(4) Insulation experienced an opposite effect from that seen by the composite. It was affected more than the composite layers by the changes in properties, seeing an almost uniform decrease of around 20% in stress from volume fraction 0.3 to 0.5.

(5) Corners do not serve as stress concentrators for the magnetic loading in the solenoid; the stress concentration is rather due to contact between adjacent turns and the contact stress present when two materials meet. Rounding the corners of the composite and insulation increase the stresses at these critical points. While rounding the corners did move and possibly spread out the stress, it did not eliminate the concentration.

(6) The stress that occurs in the insulation, especially due to the compression of the insulation by adjacent turns, is very important to monitor since the insulation will probably fail before the composite itself does.

(7) Highest stress for all loading types occurred in the fiber direction. This is fortunate because the fiber direction has the superior properties due to the increased stiffness inherited by the composite material from the wires.

(8) For the magnetic model, stress in the *r*-direction was affected more by volume fraction than stress in the *z*-direction. Stress in the hoop direction was affected half as much as these, most likely due to the wires being wound in the hoop direction. Shear stress increase was negligible with increasing fiber volume fraction.

(9) In general, magnetic stresses are less sensitive to V_f effects than thermal stresses. Stresses induced by the pressure loading were affected least of all three types of loadings.

6.2 Recommendations

As outlined above, there are methods available to develop mathematical models that describe the behavior of fiber-reinforced composite materials with a good degree of accuracy. However, in the course of literature reviews it was observed that relatively little material is available in the area of metal wires for fiber-reinforced composite materials. Whenever metal is used as the reinforcement, it is usually in the form of whiskers as discussed previously. However, fusion applications are relatively unique in that they must have very long, continuous reinforcements because the copper wires carry a current in them by virtue of their purpose of creating magnetic fields.

Recommendations for future work follow:

(1) Very little literature is available in the use of metals as fiber reinforcement. Therefore, more research must be performed to characterize material properties when metals such as the copper used in this research are used for reinforcement purposes. It is believed that the strength in the fiber (longitudinal) direction would in practice be stronger than the models predict it to be. Existing models were used in this analysis but the confidence in their predictions would be stronger if a more complete analysis on this type of composite were performed.

(2) Mathematical models and finite element analysis are only as accurate as the physics they are based on and the material properties that are input into the model. Therefore it is suggested that experiments using the composite material with several different fiber volume fractions be performed to discover and develop material properties used in this analysis. These could be used to verify the results of the mathematical model as well as to instill more accuracy in the FEA simulation.

(3) Development and testing of a sample composite cylinder or preferably of several cylinders of different fiber volume fractions to verify material reaction to loads would be useful. Furthermore, these cylinders could be loaded to failure under several loads so that a failure criterion could be used in the models developed in this report.

(4) More extensive finite element analysis is suggested. This could be done to develop a combined model that incorporates magnetic loads, thermal loads, and pressure loads all together. Furthermore, a model that incorporates the moisture effects developed in Phase 1 of the research would be useful.

REFERENCES

1. IT Power Climate Change Consulting. (2004). [Energy Sources Worldwide Bar Chart 2004.] Retrieved from http://www.itpi.co.in/Resources/Renewable_energy/Renewable_energy.htm
2. United Kingdom Atomic Energy Authority. (2008). Retrieved from http://fusion.org.uk/mast/index.html
3. Wesson, J., & Campbell, D.J. (2004). *Tokamaks*. (3rd ed.). New York: Oxford University Press.
4. Davis, S.R. and Voss, G.M. (2009). *Manufacture and test of a prototype cyanate ester coil*. Manuscript funded by United Kingdom Engineering and Physical Sciences Research Council and by EURATOM.
5. Voss, G., Fabian, P., Feucht, S., Harte, M., & Terry, C. *Performance evaluation of cyanate ester resin.* Manuscript funded by the United Kingdom Engineering and Physical Sciences Research Council and by EURATOM.
6. Morgan, B., Madhukar, M., Walsh, J., Hooker, M., & Grandlienard, S. (2010). Moisture degradation of cyanate ester/S2 glass composite insulation systems. *Journal of Composite Materials*, 44, 821-837.
7. Fabian, P.E., Munshi, N.A., & Denis, R.J. (2001, July). *Highly radiation-resistant vacuum impregnation resin systems for fusion magnet insulation*. Paper presented at the meeting of ICMC, Madison, WI.
8. Hooker, M. Ph.D. Mechanical Engineer. (personal communication, January 2009 – May 2010).
9. National Compact Stellarator Experiment. (2008). [NCSX Machine 2008.] Retrieved from http://ncsx.pppl.gov/
10. Berthelot, J.M. (1999). *Composite materials: Mechanical behavior and structural analysis.* New York: Springer – Verlag New York.
11. Jones, R.M. (1975). *Mechanics of composite materials.* Washington, D.C.: McGraw – Hill.

12. Hillermeier, R.W., & Seferis, J.C. (2000). Environmental effects on thermoplastic and elastomer toughened cyanate ester composite systems. *Journal of Applied Polymer Science*, *77*, 556-557.
13. Goertzen, W.K., & Kessler, M.R. (2006). Thermal and mechanical evaluation of cyanate ester composites with low-temperature processability. *ScienceDirect*. Sponsored by Iowa State University.
14. Tsai, S.W., & Hahn, H.T. (1980). *Introduction to composite materials.* Lancaster, PA: Technomic Publishing.
15. Ventsel, E., & Krauthammer, T. (2001). *Thin plates and shells: Theory, analysis, and applications.* New York: Marcel Dekker.
16. McMillan Jr., J.P. (1994). *Effects of fiber volume fraction on the elastic stability of specially orthotropic plates* (Master's thesis). University of Tennessee, Knoxville.
17. Sayre, J. R. (1997). *The effects of bias angle and fiber volume fraction on the mechanical properties of filament-wound, polypropylene-glass tubes* (Master's thesis). University of Tennessee, Knoxville.
18. Kavuri, H. (2004). *Cure behavior study and elastic modulus characterization of resin system of a quasi poloidal stellarator modular coil* (Master's thesis). University of Tennessee, Knoxville.
19. Hyer, M.W. (1998). *Stress analysis of fiber-reinforced composite materials*. New York: WCB McGraw Hill.
20. Chawla, K.K. (1998). *Composite materials: Science and engineering*. (2nd ed.). New York: Springer – Verlag New York.
21. Gibson, R.F. (2007) *Principles of composite material mechanics*. (2nd ed.). CRC Press.
22. Reddy, J.N. (2007) *Theory and analysis of elastic plates and shells*. (2nd ed.). Boca Raton, FL: Taylor and Francis Group.

23. Young, H.D., & Freedman, R.A. (2004). *University physics: With modern physics*. (11th ed.). San Francisco: Pearson Education.
24. San Jose State Department of Physics and Astronomy. (2007). [Physics 51 – Electricity & Magnetism.] Retrieved from http://www.physics.sjsu.edu/becker/physics51/mag_field.htm
25. Tipler, P.A. (1999). *Physics for scientists and engineers*. (4th ed.). New York: W.H. Freeman and Company.
26. Connexions, Rice University. (2010). [Magnetic field due to current in straight wire.] Retrieved from http://cnx.org/content/m31103/latest/
27. AP Physics, Waterville High School, Waterville, ME. (2006). [The Magnetic Field.] Retrieved from http://www.apphysics.net/elecmag/magfield.html
28. COMSOL AC/DC Module Documentation. Retrieved from C:\COMSOL35a\doc\acdc\acdcug.pdf
29. Becker, R. (1964). *Electromagnetic fields and interactions.* New York: Blaisdell Publishing.
30. Norton, R.L. (2006). *Machine design: An integrated approach.* (3rd ed.). Upper Saddle River, NJ: Pearson Prentice Hall.
31. Hibbeler, R.C. (2005). *Mechanics of materials*. (6th ed.). Upper Saddle River, NJ: Pearson Prentice Hall.
32. Annex to Design Requirements and Guidelines Level 1. Structural Material Database Article 3: Non-Metalllic Materials Database and Specifications – Electrical Insulation Materials. Provided by ITER.
33. Freudenberg, K. Mechanical Engineer. (personal communication, July 2009 – April 2010).

APPENDIX

Principle Code Used in Analysis

```
% Modeling of the Lamina Level Analysis of a Copper/Cyanate Ester Composite

clear all;
clc;

% First, material properties
% Fiber Volume Fractions
vf1 = 0.3;
vf2 = 0.4;
vf3 = 0.5;

% Fiber and matrix material properties
Ef = 120.7;       %(GPa)
Em = 37.9;        %(GPa)
Gf = 44.7;        %(GPa)
Gm = 15.8;        %(GPa)
nuf = 0.35;
num = 0.20;
ctef = 17;       %x10e-6 1/K
ctem = 52.96;     %x10e-6 1/K

% Micromechanics %
% Loop through both equations to see the trends
n = 1;
for ii = 0:0.01:1
   fibervf(n) = ii;

   e1(n) = Ef*ii+Em*(1-ii);
   e2(n) = Em*((1-sqrt(ii))+(sqrt(ii))/(1-sqrt(ii)*(1-Em/Ef)));
   v1(n) = nuf*ii+num*(1-ii);
   v2(n) = (v1(n)*e2(n))/e1(n);
   g(n) = Gm*((1-sqrt(ii))+(sqrt(ii))/(1-sqrt(ii)*(1-Gm/Gf)));
   c1(n) = ((ctef*Ef-ctem*Em)*ii+ctem*Em)/((Ef-Em)*ii+Em);
   c2(n) = ctem+(ctef-ctem)*ii;

   n = n+1;
end


% Off-axis behavior of Lamina
E1_1 = Ef*vf1+Em*(1-vf1);
E1_2 = Ef*vf2+Em*(1-vf2);
E1_3 = Ef*vf3+Em*(1-vf3);

E2_1 = Em*((1-sqrt(vf1))+(sqrt(vf1))/(1-sqrt(vf1)*(1-Em/Ef)));
E2_2 = Em*((1-sqrt(vf2))+(sqrt(vf2))/(1-sqrt(vf2)*(1-Em/Ef)));
E2_3 = Em*((1-sqrt(vf3))+(sqrt(vf3))/(1-sqrt(vf3)*(1-Em/Ef)));
```

```
nu12_1 = vf1*nuf+(1-vf1)*num;
nu12_2 = vf2*nuf+(1-vf2)*num;
nu12_3 = vf3*nuf+(1-vf3)*num;

nu21_1 = (nu12_1*E2_1)/E1_1;
nu21_2 = (nu12_2*E2_2)/E1_2;
nu21_3 = (nu12_3*E2_3)/E1_3;

G12_1 = Gm*((1-sqrt(vf1))+(sqrt(vf1))/(1-sqrt(vf1)*(1-Gm/Gf)));
G12_2 = Gm*((1-sqrt(vf2))+(sqrt(vf2))/(1-sqrt(vf2)*(1-Gm/Gf)));
G12_3 = Gm*((1-sqrt(vf3))+(sqrt(vf3))/(1-sqrt(vf3)*(1-Gm/Gf)));

% Thermal Analysis %

% Nonlinear equation for thermal expansion in longitudinal direction
cte1_1 = ctef*vf1+ctem*(1-vf1);
cte1_2 = ctef*vf2+ctem*(1-vf2);
cte1_3 = ctef*vf3+ctem*(1-vf3);

% Rule of mixture for transverse thermal expansion coefficient
cte2_1 = (ctef*ctem)/(vf1*ctem+(1-vf1)*ctef);
cte2_2 = (ctef*ctem)/(vf2*ctem+(1-vf2)*ctef);
cte2_3 = (ctef*ctem)/(vf3*ctem+(1-vf3)*ctef);

% Lamina Level Analysis as a function of theta %
n = 1;
for i = 0:0.5:90
   theta(n) = i;

   Ex_1(n) = E1_1/((cosd(i))^4+((E1_1/G12_1)-
2*nu12_1)*(cosd(i))^2*(sind(i))^2+(E1_1/E2_1)*(sind(i))^4);
   Ex_2(n) = E1_2/((cosd(i))^4+((E1_2/G12_2)-
2*nu12_2)*(cosd(i))^2*(sind(i))^2+(E1_2/E2_2)*(sind(i))^4);
   Ex_3(n) = E1_3/((cosd(i))^4+((E1_3/G12_3)-
2*nu12_3)*(cosd(i))^2*(sind(i))^2+(E1_3/E2_3)*(sind(i))^4);

   Ey_1(n) = E2_1/((cosd(i))^4+((E2_1/G12_1)-
2*nu21_1)*(cosd(i))^2*(sind(i))^2+(E2_1/E1_1)*(sind(i))^4);
   Ey_2(n) = E2_2/((cosd(i))^4+((E2_2/G12_2)-
2*nu21_2)*(cosd(i))^2*(sind(i))^2+(E2_2/E1_2)*(sind(i))^4);
   Ey_3(n) = E2_3/((cosd(i))^4+((E2_3/G12_3)-
2*nu21_3)*(cosd(i))^2*(sind(i))^2+(E2_3/E1_3)*(sind(i))^4);

   Gxy_1(n) = G12_1/((cosd(i))^4+(sind(i))^4+2*(2*(G12_1/E1_1)*(1+2*nu12_1)+2*(G12_1/E2_1)-
1)*(cosd(i))^2*(sind(i))^2);
   Gxy_2(n) = G12_2/((cosd(i))^4+(sind(i))^4+2*(2*(G12_2/E1_2)*(1+2*nu12_2)+2*(G12_2/E2_2)-
1)*(cosd(i))^2*(sind(i))^2);
```

```
   Gxy_3(n) = G12_3/((cosd(i))^4+(sind(i))^4+2*(2*(G12_3/E1_3)*(1+2*nu12_3)+2*(G12_3/E2_3)-
1)*(cosd(i))^2*(sind(i))^2);


   nuxy_1(n) = (nu12_1*((cosd(i))^4+(sind(i))^4)-(1+(E1_1/E2_1)-
(E1_1/G12_1))*(cosd(i))^2*(sind(i))^2)/...
      ((cosd(i))^4+((E1_1/G12_1)-2*nu12_1)*(cosd(i))^2*(sind(i))^2+(E1_1/E2_1)*(sind(i))^4);
   nuxy_2(n) = (nu12_2*((cosd(i))^4+(sind(i))^4)-(1+(E1_2/E2_2)-
(E1_2/G12_2))*(cosd(i))^2*(sind(i))^2)/...
      ((cosd(i))^4+((E1_2/G12_2)-2*nu12_2)*(cosd(i))^2*(sind(i))^2+(E1_2/E2_2)*(sind(i))^4);
   nuxy_3(n) = (nu12_3*((cosd(i))^4+(sind(i))^4)-(1+(E1_3/E2_3)-
(E1_3/G12_3))*(cosd(i))^2*(sind(i))^2)/...
      ((cosd(i))^4+((E1_3/G12_3)-2*nu12_3)*(cosd(i))^2*(sind(i))^2+(E1_3/E2_3)*(sind(i))^4);

   nuyx_1(n) = (nu21_1*((cosd(i))^4+(sind(i))^4)-(1+(E2_1/E1_1)-
(E2_1/G12_1))*(cosd(i))^2*(sind(i))^2)/...
      ((cosd(i))^4+((E2_1/G12_1)-2*nu21_1)*(cosd(i))^2*(sind(i))^2+(E2_1/E1_1)*(sind(i))^4);
   nuyx_2(n) = (nu21_2*((cosd(i))^4+(sind(i))^4)-(1+(E2_2/E1_2)-
(E2_2/G12_2))*(cosd(i))^2*(sind(i))^2)/...
      ((cosd(i))^4+((E2_2/G12_2)-2*nu21_2)*(cosd(i))^2*(sind(i))^2+(E2_2/E1_2)*(sind(i))^4);
   nuyx_3(n) = (nu21_3*((cosd(i))^4+(sind(i))^4)-(1+(E2_3/E1_3)-
(E2_3/G12_3))*(cosd(i))^2*(sind(i))^2)/...
      ((cosd(i))^4+((E2_3/G12_3)-2*nu21_3)*(cosd(i))^2*(sind(i))^2+(E2_3/E1_3)*(sind(i))^4);

   ctex_1(n) = cte1_1*(cosd(i))^2+cte2_1*(sind(i))^2;
   ctex_2(n) = cte1_2*(cosd(i))^2+cte2_2*(sind(i))^2;
   ctex_3(n) = cte1_3*(cosd(i))^2+cte2_3*(sind(i))^2;

   ctey_1(n) = cte1_1*(sind(i))^2+cte2_1*(cosd(i))^2;
   ctey_2(n) = cte1_2*(sind(i))^2+cte2_2*(cosd(i))^2;
   ctey_3(n) = cte1_3*(sind(i))^2+cte2_3*(cosd(i))^2;

   ctexy_1(n) = 2*(cte1_1-cte2_1)*cosd(i)*sind(i);
   ctexy_2(n) = 2*(cte1_2-cte2_2)*cosd(i)*sind(i);
   ctexy_3(n) = 2*(cte1_3-cte2_3)*cosd(i)*sind(i);

   n = n+1;

end

% Plot the results
figure(1);
plot(fibervf,e1,fibervf,e2);
xlabel('Fiber Volume Fraction');
ylabel('Young''s Modulus, GPa');
legend('E1','E2','Location','East');
```

```
figure(2);
plot(fibervf,g);
xlabel('Fiber Volume Fraction');
ylabel('Shear Modulus, GPa');

figure(3);
plot(fibervf,v1);
xlabel('Fiber Volume Fraction');
ylabel('Poisson''s Ratio');


figure(4);
plot(theta,Ex_1,theta,Ex_2,theta,Ex_3);
xlabel('Orientation Angle Theta (Degrees)');
ylabel('Longitudinal Stiffness Modulus Ex (GPa)');
legend('Fiber Volume Fraction = 0.3','Fiber Volume Fraction = 0.4','Fiber Volume Fraction = 0.5');

figure(5);
plot(theta,Ey_1,theta,Ey_2,theta,Ey_3);
xlabel('Orientation Angle Theta (Degrees)');
ylabel('Transverse Stiffness Modulus Ey (GPa)');
legend('Fiber Volume Fraction = 0.3','Fiber Volume Fraction = 0.4','Fiber Volume Fraction =
0.5','Location','Northwest');

figure(6);
plot(theta,Gxy_1,theta,Gxy_2,theta,Gxy_3);
xlabel('Orientation Angle Theta (Degrees)');
ylabel('Shear Stiffness Modulus Gxy (GPa)');
legend('Fiber Volume Fraction = 0.3','Fiber Volume Fraction = 0.4','Fiber Volume Fraction = 0.5');

figure(7);
plot(theta,nuxy_1,theta,nuxy_2,theta,nuxy_3);
xlabel('Orientation Angle Theta (Degrees)');
ylabel('Poisson''s Ratio vxy');
legend('Fiber Volume Fraction = 0.3','Fiber Volume Fraction = 0.4','Fiber Volume Fraction = 0.5');

figure(8);
plot(theta,nuyx_1,theta,nuyx_2,theta,nuyx_3);
xlabel('Orientation Angle Theta (Degrees)');
ylabel('Poisson''s Ratio vyx');
legend('Fiber Volume Fraction = 0.3','Fiber Volume Fraction = 0.4','Fiber Volume Fraction = 0.5');


figure(9);
plot(fibervf,c1,fibervf,c2);
xlabel('Fiber Volume Fraction');
ylabel('Coefficient of Thermal Expansion, x10e6 (K^-1)');
legend('Logitudinal Direction','Transverse Direction');
```

```
figure(10);
plot(theta,ctex_1,theta,ctex_2,theta,ctex_3);
xlabel('Orientation Angle Theta (Degrees)');
ylabel('Coefficient of Thermal Expansion ax (x10^-6 1/K)');
legend('Fiber Volume Fraction = 0.3','Fiber Volume Fraction = 0.4','Fiber Volume Fraction = 0.5');

figure(11);
plot(theta,ctey_1,theta,ctey_2,theta,ctey_3);
xlabel('Orientation Angle Theta (Degrees)');
ylabel('Coefficient of Thermal Expansion ay (x10^-6 1/K)');
legend('Fiber Volume Fraction = 0.3','Fiber Volume Fraction = 0.4','Fiber Volume Fraction = 0.5',...
   'Location','Northwest');

figure(12);
plot(theta,ctexy_1,theta,ctexy_2,theta,ctexy_3);
xlabel('Orientation Angle Theta (Degrees)');
ylabel('Coefficient of Thermal Expansion axy (x10^-6 1/K)');
legend('Fiber Volume Fraction = 0.3','Fiber Volume Fraction = 0.4','Fiber Volume Fraction = 0.5');


% Modeling of Laminate Level Analysis of a Copper/Cyanate Ester Composite %

lay = xlsread('C:\Users\Chance\Documents\Thesis and Research\Matlab Modeling\Input
Data','sheet1','B2'); % Number of layers

% Loop to calculate thickness of each layer (mm)
x = xlsread('C:\Users\Chance\Documents\Thesis and Research\Matlab Modeling\Input
Data','sheet1','G3:G22');
tt = 0;
for i = 1:lay
   t(i) = x(i);
   tt = tt+t(i);
end

% Loop to calculate z coordinates for each layer (midline = 0)
z(1) = -tt/2;
z(lay+1) = tt/2;
for i = 2:lay
   z(i) = z(i-1)+t(i-1);
end

% Stiffness matrix Qij (Qc) and Glass Cloth matrix Qg
qc = xlsread('C:\Users\Chance\Documents\Thesis and Research\Matlab Modeling\Input
Data','sheet1','B17:D19');
qg = xlsread('C:\Users\Chance\Documents\Thesis and Research\Matlab Modeling\Input
Data','sheet1','B20:D22');
```

```
% Read in the thermal coefficients alpha1 and alpha2
alpha1 = xlsread('C:\Users\Chance\Documents\Thesis and Research\Matlab Modeling\Input
Data','sheet1','C6');
alpha2 = xlsread('C:\Users\Chance\Documents\Thesis and Research\Matlab Modeling\Input
Data','sheet1','C7');
alphag1 = xlsread('C:\Users\Chance\Documents\Thesis and Research\Matlab Modeling\Input
Data','sheet1','C8');
alphag2 = xlsread('C:\Users\Chance\Documents\Thesis and Research\Matlab Modeling\Input
Data','sheet1','C9');

% Calculate the matrices A, B, D and thermal coefficients and loop for each layer
y = xlsread('C:\Users\Chance\Documents\Thesis and Research\Matlab Modeling\Input
Data','sheet1','H3:H22');
A = 0;
B = 0;
D = 0;
n = 1;
for i = 1:lay
   if mod(i,2) == 1;
      angle(i) = y(i);
      q(:,n:n+2) = qtrans(qc,angle(i));
      A = A+q(:,n:n+2)*t(i);
      B = B+(1/2)*((z(i+1))^2-(z(i)^2))*q(:,n:n+2);
      D = D+(1/3)*((z(i+1))^3-(z(i)^3))*q(:,n:n+2);
      cte(:,n) = alpha1*(cos(angle(i)*pi/180))^2+alpha2*(sin(angle(i)*pi/180))^2;
      cte(:,n+1) = alpha1*(sin(angle(i)*pi/180))^2+alpha2*(cos(angle(i)*pi/180))^2;
      cte(:,n+2) = 2*(alpha1-alpha2)*cos(angle(i)*pi/180)*sin(angle(i)*pi/180);
      n = n+3;
   else
      angle(i) = y(i);
      q(:,n:n+2) = qtrans(qg,angle(i));
      A = A+q(:,n:n+2)*t(i);
      B = B+(1/2)*((z(i+1))^2-(z(i)^2))*q(:,n:n+2);
      D = D+(1/3)*((z(i+1))^3-(z(i)^3))*q(:,n:n+2);
      cte(:,n) = alphag1;
      cte(:,n+1) = alphag2;
      cte(:,n+2) = 0;
      n = n+3;
   end
end

% Get the internal pressure P
pressure = xlsread('C:\Users\Chance\Documents\Thesis and Research\Matlab Modeling\Input
Data','sheet1','B3');
pvradius = xlsread('C:\Users\Chance\Documents\Thesis and Research\Matlab Modeling\Input
Data','sheet1','C4');
```

```
% N-M matrix
n_m(1,1) = pressure*pvradius;
n_m(2,1) = 0.5*pressure*pvradius;
n_m(3:6,1) = 0;

% A-B-B-D matrix
abbd = A;
abbd(4:6,1:3) = B;
abbd(1:3,4:6) = B;
abbd(4:6,4:6) = D;

% Find e-k matrix
e_k = (inv(abbd))*n_m;
% e_k = [1000e-3 0 0 0 0 0];

% Extract the temperature distribution delta T
dt = xlsread('C:\Users\Chance\Documents\Thesis and Research\Matlab Modeling\Input
Data','sheet1','B5');


% Calculate stresses in each layer and add in thermal stress
f = 1;
g = 1;
cte = cte';
for i = 1:lay
   for j = z(i):0.0001:z(i+1)
      % stress(:,f) = q(:,g:g+2)*e_k(1:3)+q(:,g:g+2)*j*e_k(4:6)-q(:,g:g+2)*cte(:,g:g+2)*dt;
      stress(:,f) = q(:,g:g+2)*(e_k(1:3)+j*e_k(4:6)-dt*cte(g:g+2,:));
            thick(f) = j;
      f = f+1;
   end

   g = g+3;
end


% Plot the results
figure(13)
plot(thick,stress(1,:),'r')
xlabel('Z-Coordinate of Thickness, mm')
ylabel('Stress, kPa')
title('Normal Stress in the X-Direction')

figure(14)
plot(thick,stress(2,:),'b')
xlabel('Z-Coordinate of Thickness, mm')
ylabel('Stress, kPa')
title('Normal Stress in the Y-Direction')
```

```
figure(15)
plot(thick,stress(3,:),'m')
xlabel('Z-Coordinate of Thickness, mm')
ylabel('Stress, kPa')
title('Shear Stress in the XY-Direction')


% check thin-walled vs. thick-walled stress
ro = pvradius+tt/2;
ri = pvradius -tt/2;
pthh = (((ri^2)*pressure)/(ro^2-ri^2))*(1+(ro^2)/(ri^2))*tt;
ptha = (((ri^2)*pressure)/(ro^2-ri^2))*tt;

% End of Program
```

Function for Transposing Stiffness Matrices

```
function [q] = qtrans(a,b)
% QTRANS(Q,A) will transpose a 3x3 symmetric orthotropic composite
% stifness matrix Q into another stiffness matrix that corresponds
% to the angle shift A.


b=b*(pi/180)

c(1,1) = a(1,1)*(cos(b))^4+a(2,2)*(sin(b))^4+2*(a(1,2)+2*a(3,3))*((sin(b))^2)*((cos(b))^2)
c(2,2) = a(1,1)*(sin(b))^4+a(2,2)*(cos(b))^4+2*(a(1,2)+2*a(3,3))*((sin(b))^2)*((cos(b))^2)
c(1,2) = (a(1,1)+a(2,2)-4*a(3,3))*((sin(b))^2)*((cos(b))^2)+a(1,2)*(((sin(b))^4)+((cos(b))^4))
c(3,3) = (a(1,1)+a(2,2)-2*a(1,2)-2*a(3,3))*((sin(b))^2)*((cos(b))^2)+a(3,3)*(((sin(b))^4)+((cos(b))^4))
c(1,3) = (a(1,1)-a(1,2)-2*a(3,3))*((sin(b)))*((cos(b))^3)-(a(2,2)-a(1,2)-2*a(3,3))*((sin(b))^3)*(cos(b))
c(2,3) = (a(1,1)-a(1,2)-2*a(3,3))*((sin(b))^3)*((cos(b)))-(a(2,2)-a(1,2)-2*a(3,3))*((sin(b)))*((cos(b))^3)
c(2,1) = c(1,2)
c(3,1) = c(1,3)
c(3,2) = c(2,3)

q = c
```

Code for Finding Reduced Compliance Matrices

```
clear all;
clc;

% Find the Compliance Matrices for the Materials
% Reduced Stiffness Matrix for Orthotropic Composite
E1 = 130;
E2 = 5;
nu12 = 0.25;
G12 = 10;

nu21 = (nu12*E2)/E1
aaa(1,1) = E1/(1-nu12*nu21)
aaa(1,2) = (nu12*E2)/(1-nu12*nu21)
aaa(2,2) = E2/(1-nu12*nu21)
aaa(3,3) = G12
aaa(2,1) = aaa(1,2)


% Reduced Stiffness Matrix for Insulation
Ec1 = 12;
Ec2 = 20;
nuc12 = 0.33;
Gc12 = 6;

nuc21 = (nuc12*Ec2)/Ec1
bbb(1,1) = Ec1/(1-nuc12*nuc21)
bbb(1,2) = (nuc12*Ec2)/(1-nuc12*nuc21)
bbb(2,2) = Ec2/(1-nuc12*nuc21)
bbb(3,3) = Gc12
bbb(2,1) = bbb(1,2)

% Reduced stiffness isotropic insulation
E = 210;
nu = 0.3;

bbb(1,1) = E/(1-nu^2)
bbb(1,2) = (nu*E)/(1-nu^2)
bbb(2,2) = bbb(1,1)
bbb(3,3) = E/(2*(1+nu))
bbb(2,1) = bbb(1,2)
```

VITA

Chance Thomas Donahue was born on November 12, 1985 in Knoxville, Tennessee. He was raised in LaFollette, Tennessee where he attended East LaFollette Elementary for grades K – 5th, LaFollette Middle School for grades 6th – 8th, and went to high school at Campbell County Comprehensive High School. He graduated Salutatorian in 2004 and began college that fall at the University of Tennessee in Knoxville. After starting in Aerospace Engineering, he changed curriculum to Mechanical Engineering and graduated Summa Cum Laude in December of 2008 with his Bachelor of Science in Mechanical Engineering. During his undergraduate studies, Chance had summer internships at National Coal Corporation, CEMEX Inc. and Alcoa Inc. He began his graduate studies in January 2009 in Mechanical Engineering with a concentration of machine design and product development. He worked as a research assistant to Dr. Madhu S. Madhukar at the Magnet Development Laboratory in collaboration with UT, Oak Ridge National Laboratory, and Composite Technology Development. He will be graduating Cum Laude in August 2010 with his Masters of Science in Mechanical Engineering and begin working in July 2010 for Savannah River Nuclear Solutions, LLC as a maintenance and operations engineer in Aiken, South Carolina.